High voltage electrical discharges in the laboratory

Master thesis in space physics

by

Øystein Grøndahl

December 2014

Department of Physics and Technology

University of Bergen

Norway

Abstract

A new phenomenon called terrestrial gamma-ray flashes (TGFs) was discovered early in the 1990s by the NASA satellite Compton Gamma-Ray Observatory. The short-duration bursts of highly energetic gamma-rays are caused by bremsstrahlung from energetic electrons, but the production mechanism of these electrons is not known. TGFs were linked to lightning, and different theories of production mechanisms have been studied since.

Highly energetic radiation has been detected from long laboratory sparks, and implies production of highly energetic electrons even in laboratory sparks. Even though the potential differences are much less than those found in thunderclouds, this enabled the study of laboratory sparks to learn more about natural lightning and the production mechanism of TGFs.

In this thesis we present an experiment of high voltage electrical discharges in the laboratory. We have planned and conducted a laboratory experiment at the Eindhoven University of Technology. This experiment has collected data from a large number of sparks. Here, we present a brief review of literature relevant to terrestrial gamma-ray flashes (TGFs) and laboratory sparks. We present theories governing laboratory sparks and some theories of TGFs. We develop and discuss different tools and methods for data processing to prepare the data for future analysis.

We also discuss whether the signals from the detectors are caused by electrons and photons, and argue that they are most likely caused by electrons. A model for estimating the source locations for the electrons is suggested, but is not fully developed.

Acknowledgments

I am grateful for discussions with and guidance from my supervisor, Nikolai Østgaard. I experienced a great boost in motivation after each interaction. I wish to thank Marit Irene Sandanger, Linn-Kristine Glesnes Ødegaard and Thomas Gjesteland for their great support in finishing my thesis.

Participation from the group at the Technical University of Eindhoven was essential, as all the experiments were carried out in their laboratory. I would like to thank Brant Carlson, Pavlo Kochkin and Ragnhild Nisi for two fun and interesting weeks of experimenting in Eindhoven.

This entire experience has been been shaped by the positive influences from my colleagues at Stord/Haugesund University College. They have gone beyond expectations to help me finish my thesis.

Finally, I would like to thank my friends and family for their support during these years.

Øystein Grøndahl

18.12.2014, Bergen

Contents

List of Figures

List of Tables

Chapter 1

Introduction

1.1 Introduction

Electric sparks have long been known to humanity, but they are still far from thoroughly understood. As recently as 1994 an until then unknown phenomenon of lightning was reported: Terrestrial gamma-ray flashes (TGFs). TGFs are short bursts of highly energetic photons, typically observed by spacecraft. The fraction of high-energy photons in a TGF is higher than those for solar flares, cosmic gamma-ray bursts and other cosmic sources, making it one of the most highly energetic natural photon phenomena.

TGFs belong in the field of high-energy atmospheric physics (HEAP) (Dwyer et al., 2012), which was in a way established by C.T.R. Wilson when he proposed that electrons may on average gain more energy from a strong electric field than they lose due to collisions, and that this process may lead to high-energy radiation (Wilson, 1925).

The production altitude of TGFs is typically between approximately 14 and 21 km (Dwyer and Smith, 2005; Østgaard et al., 2008; Gjesteland et al., 2010). On average, TGFs detected by the RHESSI spacecraft contain around 10^{17} photons if the production altitude is 15 km, and 10^{16} for 20 km (Hansen et al., 2013). To produce this number of photons by bremsstrahlung, around ten times as many electrons of relativistic energies are required (Carlson et al., 2009). Skeltved et al. (2014) found the number of energetic electrons to be 1-10 times as many as the number of photons. Photon energies extend to several tens of MeV (Marisaldi et al., 2010). The typical duration of TGFs is around 0.10-0.40 ms (Fishman et al., 2011; Gjesteland et al., 2010).

Many TGFs are associated with so-called positive lightning between clouds, intracloud lightning, when a negative leader is propagating upwards between charge regions (Stanley et al., 2006; Lu et al., 2010; Shao et al., 2010). Positive lightning means that negative charge is moved upwards.

There have been several different theories describing production mechanisms that might cause TGFs. Today, two theories remain as reasonable explanations (Dwyer et al., 2012). One relies on a mechanism called relativistic feedback, which describes electrons producing photons and positrons that can travel backwards along the electric field, before they create new energetic electrons that travel forwards against the electric field (Dwyer, 2003). The other theory was introduced by Moss et al. (2006) and further developed by Celestin and Pasko (2011) among others. The theory states that extremely strong electric fields in the tips of lightning leaders and streamers may produce the high-energy electrons required for a TGF.

In reality both mechanisms can be operating and contribute in producing TGFs. The two theories are not mutually exclusive, and there may be other explanations.

In the middle of the 18th century, Benjamin Franklin performed his famous kite experiment to investigate whether lightning was an electrical phenomenon. It turned out that lightning is electrical, and it has been studied as such since then. It is hard to study natural lightning. We can study triggered lightning (triggered by rockets, as with Franklin's kite). Another option is to study electrical sparks, or discharges, in laboratories, in an effort to extract some knowledge that can be applied to full-size lightning discharges.

My thesis will focus on meter-length megavolt laboratory sparks. These sparks may help us to better understand the streamer-leader theory for producing TGFs. We planned and conducted a series of experiments which produced a large data set. This data set can be used to examine some properties of energetic electrons related to streamer creation in electric sparks in an effort to learn more about the streamer-leader theory. We produced the scintillating fiber detectors ourselves, and thus had to calibrate them to be able to prepare the data set for analysis.

The next parts of this thesis are the motivation and objectives for the thesis. Next is a literature study, providing a summary of some earlier work on TGFs and the related long laboratory sparks. This is followed by a section describing the theory of streamers. Then, the experimental setup and the data gathered is described. The data processing and analysis methods follow this,

and the thesis finishes with discussion, conclusions and recommendations for further work.

1.2 Motivation

The production mechanism(s) of terrestrial gamma-ray flashes (TGFs) are not fully understood. There are two reasonable theories today: The runaway relativistic electron avalanche fed by the relativistic feedback mechanism, and the theory of thermal runaway from streamers. There does not seem to be any technology applications directly related to the phenomenon of TGFs. Since the production mechanism of TGFs seems to be related to the onset of electric sparks, it is possible that some application will arise in the future. For the time being, the motivation for studying laboratory sparks is purely scientific: It is a step towards a deeper understanding of nature in general and electrical discharges and TGFs in particular.

Examining laboratory sparks (or TGFs) is basic research. We are trying to describe and understand one small part of nature, not to develop any technology or products as applied science might aim to do. There are no economical incentives, this research is driven by the interest of understanding nature and natural phenomena.

1.3 Objectives

The main objectives of this M.Sc. project are

1. Plan, prepare and conduct the laboratory spark experiments

2. Develop methods for processing the data from the experiment to prepare the data for analysis, including performing a relative calibration of the detectors

The preparations included building our own scintillating fiber detectors. Since we built these ourselves, we had no manufacturer's data sheets explaining how to read the data. We had to calibrate the detectors, and we had to find effective ways of searching through the data. The detectors and the data are not well known previous experiments in the literature (unlike datasets from standard databases). We have encountered unexpected problems, and addressed these during the progress of this project.

1.4 Ethical considerations

All works in physics should include ethical considerations. For the work described in this thesis, only one issue comes to mind: the safety of the researchers performing the experiments. High-voltage equipment and the generated x-rays do pose a safety issue for researchers. The laboratory's routines for operating the equipment and the hardware safety barriers greatly reduces the risk of injury from the equipment. However, the possible radiation dose from the generated x-rays are unknown. The dose is believed to be minuscule. This could be worthwhile confirming in future similar experiments. The topics of TGF generation and lightning initiation are neutral topics related to understanding nature, and it's next to impossible to see any way the knowledge could be used with ill intent. All in all, there seems to be no ethical issues with performing the experiments or working on the related theory.

1.5 Literature study

This section is a brief literature study of terrestrial gamma-ray flashes (TGFs) and long laboratory sparks. The intent is to give the reader an introduction to the work that has been performed, and to show how studies of long laboratory sparks connect to studies of TGFs. It turns out that studying laboratory sparks may help us understand the source mechanism(s) of TGFs. For a comprehensive review that goes into greater detail of the history and development of theories and observations regarding TGFs, the reader is advised to look up the review by Dwyer et al. (2012). In the following, some of the theories of TGFs is introduced, to help the reader understand the later section on observations.

1.5.1 Some theory related to terrestrial gamma-ray flashes

Wilson (1925) put forth the idea that electrons in strong electric fields may on average have a greater rate of energy gain from the field than their rate of energy loss from collisions. This happens if the field is strong enough, and if the electron has an energy larger than a certain threshold.

By this mechanism, highly energetic electrons may be produced, and they can in turn pro-

duce highly energetic radiation due to bremsstrahlung. Wilson assumed source or seed particles were cosmic rays or came from other external sources. This theory allows for high-energy electrons, but not in large numbers. The energetic electrons are called runaway electrons or relativistic runaway electrons.

Gurevich et al. (1992) expanded on this idea by including the effects of Møller scattering (elastic scattering in electron-electron collisions). By scattering, more energetic electrons may be produced, and the seed particle can potentially start an avalanche of relativistic electrons, known as a relativistic runaway electron avalanche (RREA). With a larger amount of energetic electrons, the amount of bremsstrahlung might explain the bursts of gamma-rays in TGFs.

Later, Dwyer (2003) further expanded on the idea by introducing relativistic feedback. Relativistic electrons may produce photons that may propagate in a direction (partially) opposite to the field. If the photon later produces a new energetic electron, this electron may be accelerated through the field again and thus be the seed for a new avalanche of energetic electrons. The same may happen if a positron is created by pair-production by a photon, since the positron would be accelerated backwards in the direction of the field. With this modification of the theory of RREAs, much larger numbers of energetic electrons, and thus gamma-rays, may be produced.

Another theory for the production of high-energy electrons is that they are created by strong electric fields in lightning leader or streamer channels. Such electrons may be seed particles for relativistic runaway electron avalanches, or may themselves give off the radiation that is a TGF. This theory was set forth after Dwyer et al. (2005b) discovered x-ray bursts produced by laboratory sparks in air.

1.5.2 Observations and simulations of terrestrial gamma-ray flashes

The first paper to report on TGFs (Fishman et al., 1994) was based on observations by the Burst and Transient Source Experiment (BATSE) on the NASA satellite Compton Gamma Ray Observatory (CGRO). Ironically, BATSE discovered TGFs while on a mission to search for cosmic gamma-ray bursts, which were discovered by the Vela satellites, whose mission was to search for gamma-rays from the atmosphere due to nuclear testing (Klebesadel, 1973).

Based upon the first observation of TGFs by BATSE, TGFs were thought to last approximately 1 ms, originate at altitudes above at least 30 km and to fit a bremsstrahlung spectrum with a

characteristic energy of 1 MeV (Fishman et al., 1994). All these numbers were later refined and changed by other observations and other work.

Shortly after the discovery of TGFs, Inan et al. (1996) reported that TGFs were linked in time and space to individual radio atmospheric signals ('spherics'), which occur due to atmospheric lightning discharges, thus providing a direct association between lighting and TGFs.

The second spacecraft that observed TGFs was the Reuven Ramaty High Energy Solar Spectroscopic Imager (RHESSI) spacecraft (Lin et al., 2002). Using RHESSI data, Smith et al. (2005) found photon energies up to 10-20 MeV that were produced by bremsstrahlung from 20-40 MeV electrons. Smith et al. (2005) also stated that RHESSI's 10 to 20 monthly TGF observations corresponded to 50 TGFs per day globally, and to a larger number if TGFs turned out to be narrowly beamed. Dwyer and Smith (2005) showed by Monte Carlo simulations that the production altitude of RHESSI TGFs was likely to be around 15-21 km, see Figure 1.1. They also reported that the soft energy spectrum of some BATSE TGFs made it unlikely that they originated so deep in the atmosphere. This in turn indicated that there might be two different production mechanisms for TGFs. In the same simulations, Dwyer and Smith (2005) also estimated the necessary number of runaway electrons with energies over 1 MeV (energetic electrons) to produce the observed fluencies of gamma-rays at 600 km altitude: For a source altitude of 21 km, a total of 10^{16} energetic electrons are required. For a source altitude of 15 km, a total of $2 \cdot 10^{17}$ energetic electrons are required. The same simulations also indicated that a mechanism known as relativistic runaway electron avalanche (RREA) could be part of the production mechanism for TGFs. RREAs are explained in subsection 2.2.1.

BATSE data were revisited, and the best estimates for source altitudes were found to be around 15-20 km (Carlson et al., 2007; Østgaard et al., 2008; Gjesteland et al., 2010), while the >30 km sources for BATSE TGFs were shown to be incorrect, due to dead time losses in the BATSE detectors (Grefenstette et al., 2008; Gjesteland et al., 2010). Gjesteland et al. (2010) also found that the typical duration of BATSE TGFs was 0.25 ms.

Cummer (2005) analyzed atmospheric radio emissions ("sferics") from lightning discharges associated with some RHESSI TGFs to link TGFs to lightning. He also found that TGFs can not have a production altitude over 30 km due to the measured current moments.

Many TGFs are associated with positive intracloud lightning (+IC), which are negative light-

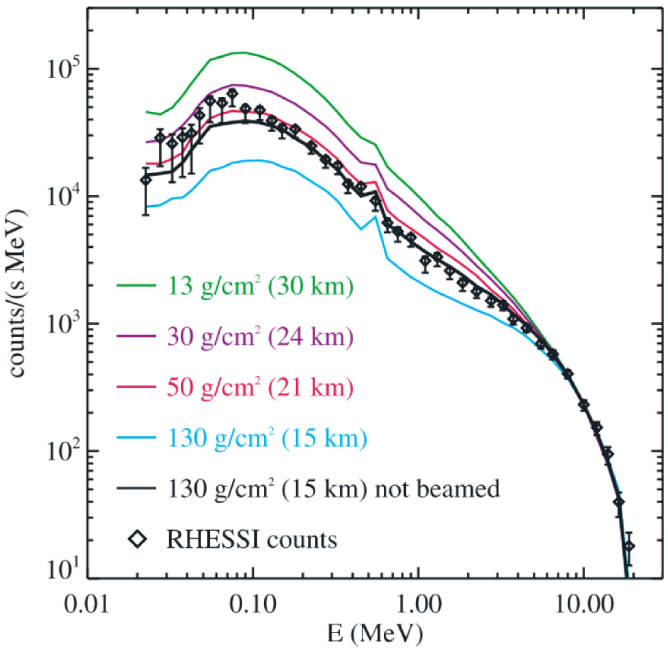

Figure 1.1: (Color) Dwyer and Smith (2005) compared measurements from the RHESSI spacecraft (shown by black points) with simulations of TGFs at different source altitudes shown by the colored lines. This figure is a copy of figure 2 of Dwyer and Smith (2005).

ning leaders proagating upwards between charge regions within clouds (Stanley et al., 2006; Lu et al., 2010; Shao et al., 2010), see Figure 1.2. Around 75 % of all lightning are intracloud lightning, and most of these are positive intracloud lightning. Therefore, TGFs may be quite common, as pointed out by Østgaard et al. (2012).

The Italian satellite Astrorivelatore Gamma a Immagini Leggero (AGILE) (Tavani et al., 2008, 2009) detected TGFs with photon energies ranging up to 40 MeV (Marisaldi et al., 2010). Tavani et al. (2011) even found single TGF photons with up to 100 MeV energies in the AGILE data. There is an ongoing debate on whether this may stem from cosmic rays.

The NASA satellite Fermi Gamma-Ray Space Telescope (Fermi) (Meegan et al., 2009) has also detected TGFs (Briggs et al., 2010). Fishman et al. (2011) found from Fermi data that TGFs usually have a duration between 0.10 ms and 0.40 ms, but can be as short as 0.05 ms.

The Airborne Detector for Energetic Lightning Emissions (ADELE) detected a TGF while being flown on an airplane close to two active thunderstorm cells (Smith et al., 2011b). After ADELE flew close to over 1000 discharges and detected only one TGF, Smith et al. (2011a) claimed that only approximately every hundredth or thousandth lightning discharge produces

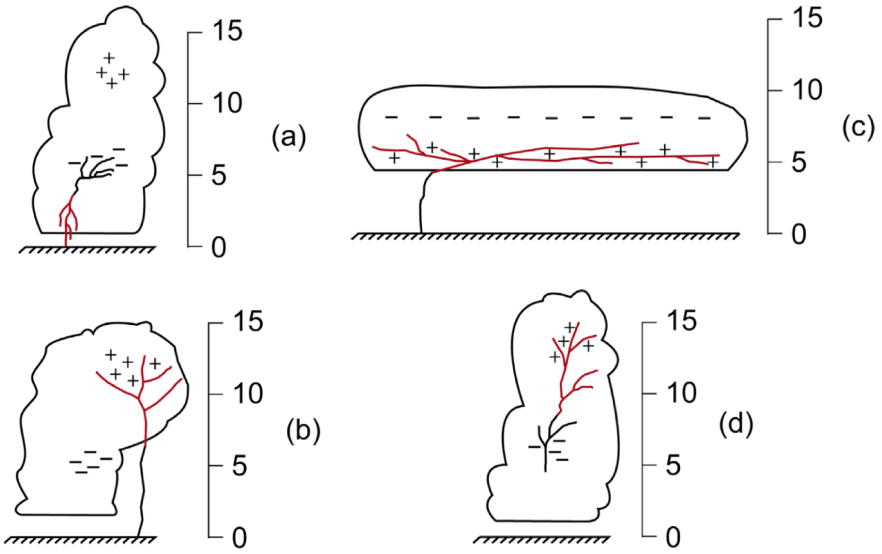

Figure 1.2: (Color) Sketches of different types of lightning. Image a) shows negative cloud-to-ground flash, image b) shows tilted positive ground flash, image c) shows positive ground flash with sheet lightning along the charge region in the cloud, and image d) shows intracloud flash. The height scale is in kilometers. All heights are in km. This figure is a copy of figure 2 of Williams et al. (2006).

a TGF.

After studying RHESSI and Fermi TGFs and the instruments' different sensitivities, Østgaard et al. (2012) argued that we can not rule out the possibility that all lightning might produce TGFs, even though ADELE detection rate was so low. If all lightning strikes can produce TGFs, the faintest TGFs would be caused by as few as 10^{12} electrons.

Gjesteland et al. (2012) developed a new method for searching for TGFs in RHESSI data, and showed that the data contained at least twice as many TGFs, especially fainter TGFs, see Figure 1.3. Briggs et al. (2013) used a new data mode and new analysis methods to examine Fermi data and found that Fermi detected TGFs 10 times more frequently than previously thought. This also supports the idea that TGFs may be common.

Splitt et al. (2010) studied lightning storms associated with TGFs, and found that certain meteorological conditions correlate well with TGF occurrences. In particular, they showed that thunderstorms producing TGFs are closely associated with tall tropical thunderstorm systems of 13.6 km to 17.3 km height.

Østgaard et al. (2013) examined the first simultaneous observations of a TGF and the optical signal from the associated lightning strike. They reported that a strong radio pulse was created

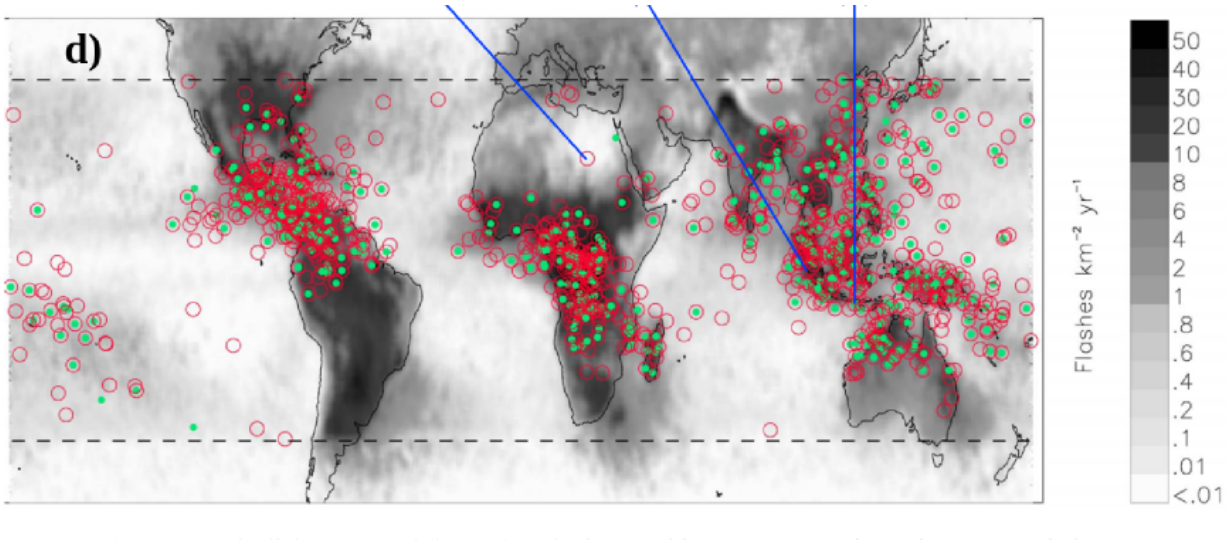

Figure 1.3: (Color) Gjesteland et al. (2012) published a map showing RHESSI TGFs observed in 2004, 2005, and 2006. The *green dots* are old TGFs, while the *red circles* are TGFs found by the new algorithm introduced in that paper. RHESSI does not collect data over South America due to the South Atlantic Anomaly which could damage the equipment. The black-to-white scale shows frequency of lightning strikes. This figure is a copy of part of figure 1 of Gjesteland et al. (2012).

by the TGF itself.

The spatial distribution of the photons of TGFs has been studied in several papers. Hazelton et al. (2009) found that narrow-beam sources were unlikely to produce the observed number of high-energy photons in some RHESSI TGFs for source altitudes over 21 km. Gjesteland et al. (2011) found that the likely half-angle of an emission cone would be $30° < \theta < 40°$.

Dwyer (2008) simulated runaway relativistic electron avalanches (RREAs, see subsection 2.2.1), and found that this mechanism by itself acting on seed particles from cosmic rays does not provide enough energetic electrons to explain TGF photons.

Dwyer (2012) presented a model for electric breakdown called the relativistic feedback discharge model, which simulates electrons in strong electric fields (as in thunderclouds). The simulations indicated that gamma ray flashes are to be expected from positive intracloud lightning in large-scale thundercloud fields when relativistic feedback is taken into account.

Skeltved (2013) simulated relativistic runaway electron avalanches (RREAs) in his M.Sc. thesis. His results indicate that for 100 MV potentials, 10^4 electrons can be expected, while previous results have indicated that the expected number is 10^6. His conclusion was that only the largest

thunderstorms can produce TGFs using the relativistic feedback mechanism alone.

Several groups of researchers have modelled runaway electron production from streamers. The simulations of Moss et al. (2006) indicated that electrons may be accelerated to 2-8 keV by strong electric fields in streamer tips in lightning leaders, and that such electrons may be the source of the TGF photons via bremsstrahlung. Celestin and Pasko (2011) expanded on this. They found that the strong electric fields in streamer tips may even produce runaway electrons with energies as high as 100 keV, while most will be around several tens of keV. Their simulations even indicated that TGFs may happen without relativistic runaway electron avalanches (RREAs), which may be difficult to sustain in the weaker electric fields observed in thunderclouds.

1.5.3 Laboratory sparks

Dwyer et al. (2012) states in the review of high-energy atmospheric physics that before 2001, it was generally believed that only low-energy electrons were involved in electrical discharges in air. These electrons could have energies of no more than a few tens of eV. When Moore and Eack (2001) and Dwyer et al. (2003) discovered emissions of x-rays that could be linked to natural and triggered lightning, it was clear that there must be some process that accelerates electrons to relativistic energies. Dwyer et al. (2005b) reported that they observed x-ray bursts from laboratory sparks (spark gaps of 1.5 m to 2 m and around 10 cm, voltage of 1.5 MV). The x-ray bursts generally occurred before the actual spark jumped the gap, while the electric field in the gap was at its highest. An example of what a meter-scale laboratory spark can look like is show in Figure 1.4.

Other groups of researchers set out to test the claims and to establish new knowledge of laboratory sparks. The findings of Rahman et al. (2008) confirmed that x-rays are produced by laboratory sparks, using a different laboratory and equipment. Dwyer et al. (2008) studied 231 sparks, and found that for about 70 % of negative voltage sparks and about 10 % of positive voltage sparks, emitted x-rays were detected. The voltage was 1 MV, and they measured single photon energies exceeding 300 keV, and total deposited energy in one detector exceeding 50 MeV for single sparks. Since the photons must be created by electron bremsstrahlung, this indicates some electrons get high energies, and that the number of electrons is high.

X-rays have been observed both before and during the collapse of the voltage over the spark

Figure 1.4: (Color) This photograph shows what a 1 meter long laboratory spark can look like. This photograph was taken by Lex van Deursen of the University of Eindhoven during our week of experimenting in January 2013.

gap (Dwyer et al., 2005b; Rahman et al., 2008; Dwyer et al., 2008; Nguyen et al., 2008).

March and Montanyà (2010) studied the effects of varying the rise time and peak voltage for laboratory sparks, and found that faster rise times and higher peak voltages in general produced more x-ray emissions with higher energies than slower rise times and lower peak voltages. They also claimed this was similar to what is detected in nature. In another paper, they showed that emissions of x-rays are affected by the geometric distribution of the electric field around the cathode (March and Montanyà, 2011).

Nijdam et al. (2008) studied stream structures using stereo photography. They found that streamers branched off at about 42° with a standard deviation of 12°, almost independent of the pressure of the gas. Nguyen (2012) studied meter-long laboratory sparks, and found that all x-ray bursts detected occurred during formation of primary streamers. Kochkin et al. (2012) reported that for positive high voltage, a corona of positive streamers emerged from the high-voltage electrode. When the streamers got closer to the grounded electrode, counter-streamers emerged from it. The connection of the sets of streamers coincided with the emission of hard x-rays. In another experiment, Kochkin et al. (2014) used nanosecond-fast photography to study the development of sparks from negative high-voltage, and to link spatial and temporal development, see Figure 1.5. They produced images that show how streamers spread and the main conducting channel (the leader) is formed. They even managed to photograph the stepping process of a leader being formed (Figure 1.6).

To summarize: Terrestrial gamma-ray flashes has been linked to radio emissions associated with lightning by Inan et al. (1996); Cummer (2005); Shao et al. (2010); Lu et al. (2010). Williams et al. (2006) suggested that TGFs are linked to high-altitude intracloud lightning in which negative leaders are moving upwards. March and Montanyà (2011) reported that the mechanism would be the same as the mechanism for negative leaders from clouds to ground, which were associated with the x-ray bursts observed at ground level by Dwyer et al. (2005a). Later the same year, Dwyer et al. (2005b) reported to have found that laboratory sparks produced x-ray bursts like those observed from lightning. Therefore, studies of high voltage laboratory sparks can provide insight in the sources of the high-energy radiation in TGFs.

Since x-rays of a few hundred keV have been observed from laboratory sparks, there must be electrons of at least those energies. Electrons of such energies can seed relativistic runaway

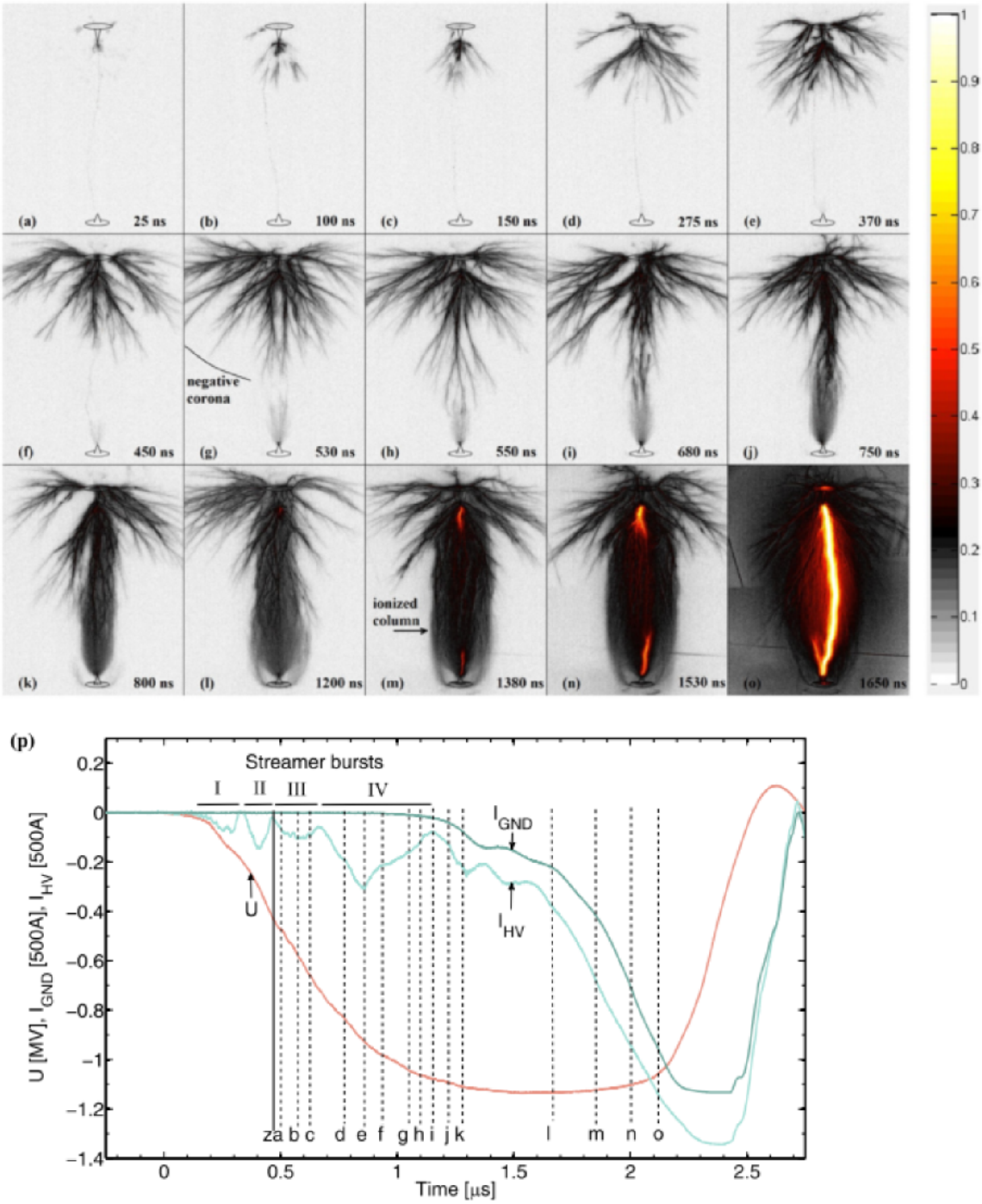

Figure 1.5: (Color) Kochkin et al. (2014) studied how 1-meter long laboratory sparks develop, using nanosecond-fast photography. The images (a) to (o) have the same shutter opening time, but different shutting time, and the measurements are averaged from 65 sparks. This figure is a copy of figure 2 of Kochkin et al. (2014).

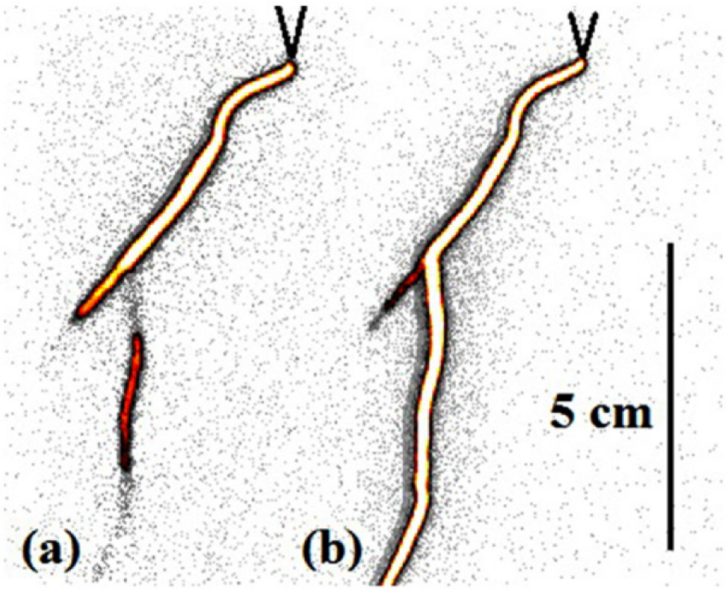

Figure 1.6: (Color) Kochkin et al. (2014) photographed the stepping process of a leader. This is similar to the stepping process seen in natural lightning of much larger spatial scales. The exposure time is 0.5 ns for each image, and the time delay between the images is 50 ns. This figure is a copy of one part of figure 15 of Kochkin et al. (2014).

electron avalanches in thundercloud electric fields. Therefore, this thesis examines electrons in laboratory sparks in an effort to learn about one possible production mechanism for terrestrial gamma-ray flashes.

Chapter 2

Theory

In this chapter we will introduce relevant theories for laboratory sparks and electron and x-ray generation, and mention some theory related to terrestrial gamma-ray flashes and lightning.

We will begin with theory of particle interactions, continue with the effects electric fields have on charged particles, and finish with a short section on thunderclouds and lightning. Since the topic of this thesis is experiments on laboratory sparks, we will not go into depth regarding actual lightning physics and all phenomena relevant for TGFs. We used 1 MV voltage in our experiments. This sets an absolute upper limit for electron and photon energies of 1 MeV, while more reasonable upper limits are around 500 keV for electrons and even less for photons.

For more depth of related topics, please read Cooray (2003), Rakov and Uman (2003), or Dwyer et al. (2012).

2.1 Laboratory spark physics

In this section we will examine some theories related to sparks, including how electrons may be produced and interact with air, and how photons may be produced by bremsstrahlung by energetic electrons. Finally, we will describe streamers and leaders, how they are formed, and how they may accelerate electrons to high energies.

This introduction to theory is based mainly on Rakov and Uman (2003), Cooray (2003), and Tipler and Llewellyn (2008).

Cross sections

Electrons and photons moving through a gas can interact with the gas and transfer energy. We will treat electrons and photons in a statistical manner. The parameter that is related to the likelihood that particles and photons interact with the gas molecules is called the cross section, σ. Tipler and Llewellyn (2008) defines the cross section σ as *the number scattered per nucleus per unit time divided by the incident intensity*. Thus, it varies with the density of the material. Cross sections depend on several variables, such as particle energies and nucleus size. The mean distance travelled between collisions or other interactions is called mean free path, λ.

2.1.1 Electron interactions with air

Energetic electrons interact with air in these ways that are relevant to this thesis: Elastic collisions, non-elastic collisions, emission of bremsstrahlung and annihilation with positrons. Electrons may ionize atoms and molecules by collisions, assuming they have enough energy to free a bound electron from the atom or molecule.

Exciting and ionizing collisions

Some collisions between particles cause atoms and molecules to be excited and ionized. If an electron collides with a molecule in the air, the electron can transfer some energy to the molecule. If the amount of energy is relatively small, the molecule will be excited. For some molecule A, this reaction can be written as follows: $e^- + A \rightarrow e^- + A^*$. When the molecule is later de-excited, a photon is released with the previously absorbed energy. The reaction can be written like this: $A^* \rightarrow A + \gamma$.

If the electron colliding with the air molecule transfers a large enough amount of energy, one or more electrons may be released from the molecule, ionizing the molecule: $e^- + A \rightarrow e^- + A^+ + e^-$. When the molecule later encounters and captures an electron, the electrons excess energy is released as a photon: $A^+ + e^- \rightarrow A + \gamma$.

Exciting and ionizing collisions are the most common processes for the electron energies in our experiments. Electron-electron scattering is called Møller scattering. This causes electrons to change directions, and it is an important factor for electron avalanches, which are discussed

in subsection 2.1.3.

Photon production by bremsstrahlung

An interaction between an electron and an atomic nucleus is sometimes called a Coulomb collision or Coulomb scattering because the Coulomb force is the main acting force. Such an interaction produces a photon by the process called bremsstrahlung. In general, bremsstrahlung involves the acceleration (change in speed, direction, or both) of an electrically charged particle. The term is perhaps most often used for electrons slowing down when passing through matter, and the name is German for braking radiation. Photons produced by bremsstrahlung are thought to be the high energy x-rays detected from laboratory sparks as reported by Dwyer et al. (2005b), Nguyen et al. (2010), and Kochkin et al. (2012) among others. The terrestrial gamma-ray flashes (TGFs) detected by satellites are also caused by bremsstrahlung from energetic electrons. Normally, bremsstrahlung photons are called x-rays no matter their energy, while photons from nuclear decay and other sources are called gamma-rays. We will call laboratory spark photons x-rays, and TGF photons gamma-rays, following the convention used in the literature (see Dwyer et al. (2012), page 143-144).

Figure 2.1 illustrates bremsstrahlung from a scattered electron. The photon's energy $E_\gamma = hf$, where h is Planck's constant, and f is the photon's frequency. This energy is equal to the electron's loss of kinetic energy:

$$E_\gamma = hf = E_{k,2} - E_{k,1} = \frac{1}{2} m_e \left(v_2^2 - v_1^2 \right) \tag{2.1}$$

The highest energy a photon may have is the entire kinetic energy of the electron, and this happens only if the electron is stopped completely while emitting a single photon (and not losing energy in other ways).

Electron-positron annihilation

This process is the opposite of photons creating an electron-positron pair: An electron and a positron collide and annihilate, and produce two or more photons (making sure to obey the conservation laws). Annihilation is shown in Figure 2.2. Due to the potential difference of 1 MV

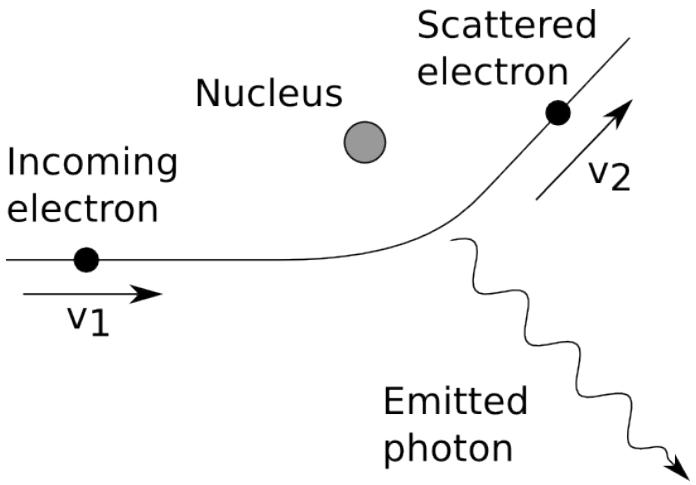

Figure 2.1: Bremsstrahlung is the emission of a photon when an electrically charged particle is acclerated by changing its speed, direction, or both.

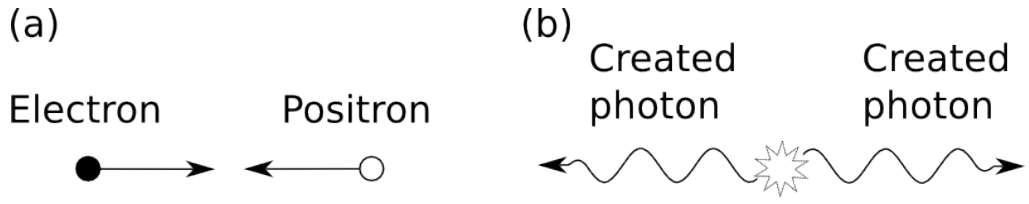

Figure 2.2: Annihilation of an electron and a positron. (a) The electron encounters its antiparticle, the positron. (b) The particles are annihilated, and in this case, two photons were created. Which products come out of the reaction are constrained by the conservation laws for momentum and energy among others.

in our laboratory sparks, we neglected any electron-positron pair production. If there are no positrons, there can be no electron-positron annihilation. Therefore, the annihilation process is not examined further. Keep in mind the process does play a role in the production of terrestrial gamma-ray flashes, where pair production occurs.

Bhabha scattering

Møller scattering is the name for electron-electron elastic collisions, while Bhabha scattering is the name for electron-positron collisions. Since we are assuming no positrons, we also neglect any effects of Bhabha scattering for this thesis.

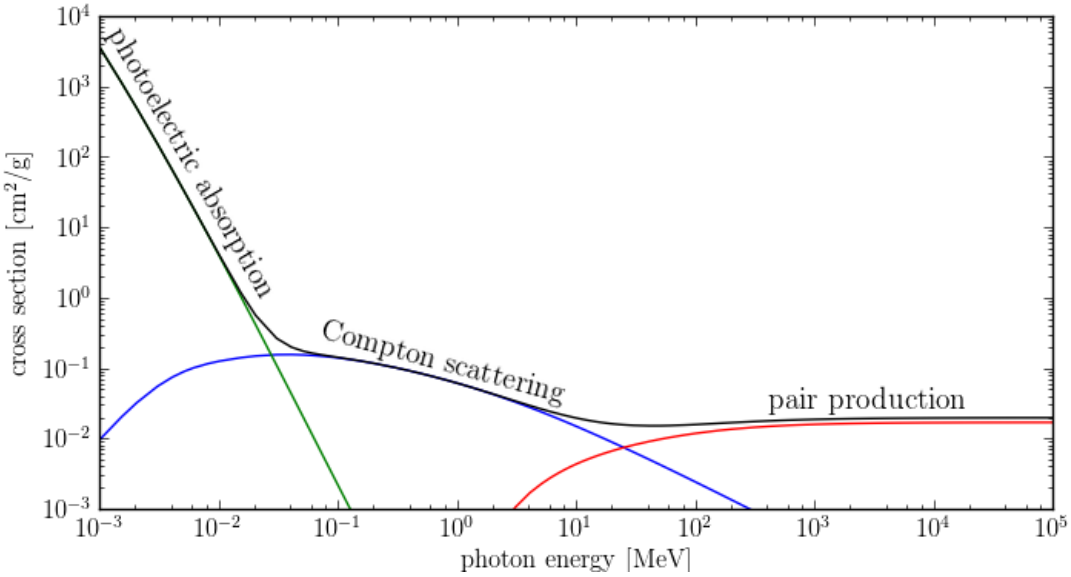

Figure 2.3: (Color) Photon interaction cross sections in nitrogen. The cross sections shown are as follows: The *black curve* on top shows the total cross section, the *green curve* on the left shows photoelectric absorption, the *blue curve* in the middle shows Compton scattering, and the *red curve* on the right shows electron-positron pair production. The main point of this figure is to show which process is dominant for different photon energy ranges. The data for the curves are from Berger et al. (1998).

2.1.2 Photon interactions with air

When we generate laboratory sparks, free electrons will be produced. They may come from ionization of the air due to the strong electric field, but electrons can also be generated by photoelectric absorption, Compton scattering, and electron-positron pair production. The last three effects are photon interactions with matter (in our case air).

Figure 2.3 shows the cross sections for photons in nitrogen, which is an approximation of air. As we can see, photoelectric absorption is dominant for low energy photons, where Compton scattering takes over as the dominant process. For high-energy photons, electron-positron pair production takes over as the most important process.

Photoelectric absorption

The process of photoelectric absorption is that an atom absorbs a photon while an electron is ejected from the atom. The electron's maximum kinetic energy is equal to the photons initial en-

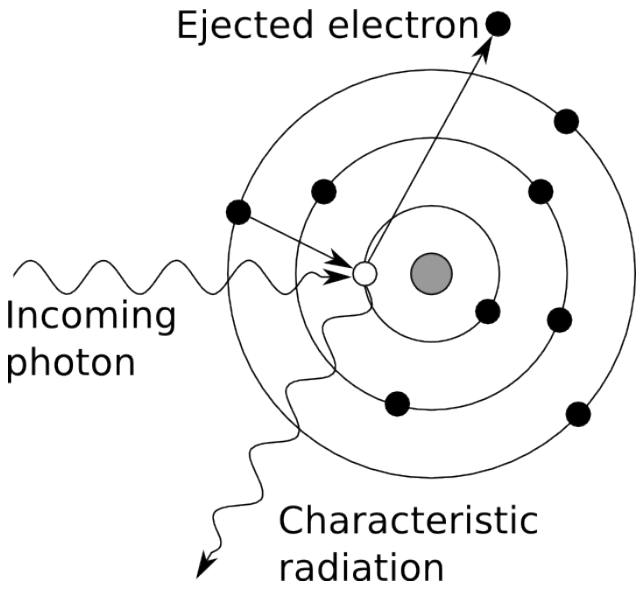

Figure 2.4: Photoelectric absorption of an incoming photon. The incoming photon is absorbed, and an electron is ejected. If there are any electrons in orbitals outside of the orbital of the ejected electron, one of them may fill the now vacant spot. This releases a photon of a wavelength characteristic to the atom. It is possible that another electron is ejected instead of the emission of the photon. This is called the *Auger effect*.

ergy hf minus ϕ, the energy required to remove the electron from the atom, where h is Planck's constant and f is the frequency of the photon.

$$\left(\frac{1}{2}m_e v^2\right)_{\max} = hf - \phi \tag{2.2}$$

This is the maximum kinetic energy of the ejected electron. As shown in Figure 2.3, this process is the most important for low-energy photons, up to around 30 keV. Figure 2.4 shows the concept of photoelectric absorption. For the expected photon energies in our experiments, photoelectric absorption is the dominant process for photons.

Compton scattering

Compton scattering is a process where a photon scatters off an electron, changes direction, and loses some energy. The energy is transferred to the electron. The original wavelength of the photon is λ_1, the new wavelength after scattering is λ_2, h is Planck's constant, m_e is the electron

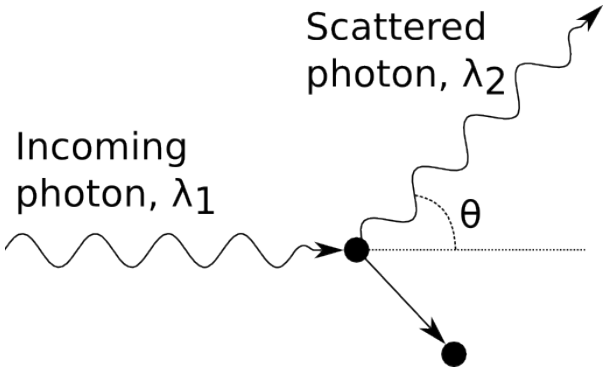

Figure 2.5: Compton scattering of an incoming photon with a wavelength λ_1 by an electron. The photon is scatter by an angle of θ with a new wavelength λ_2, while the energy lost by the photon is transferred to the electron.

mass, c is the speed of light, and θ is the scattering angle of the photon.

$$\lambda_2 - \lambda_1 = \frac{h}{m_e c}(1 - \cos(\theta)) \tag{2.3}$$

The photon's loss of energy is dependent on the scattering angle, not the original energy. The fraction $h/m_e c = 0.00243$ nm is called the *Compton wavelength of the electron.* The minimum value for the change of the wavelength is found when $\theta = 0°$: $\lambda_2 - \lambda_1 = 0$. The maximum value is found when $\theta = 180°$: $\lambda_2 - \lambda_1 = 2 \cdot 0.00243$ nm $= 0.00486$ nm. Compton scattering is the dominating process up to approximately 20 MeV. Figure 2.5 shows Comptown scattering.

Electron-positron pair production

For high energy photons, the dominating process is pair production. This process is (simply) the conversion of a photon into a particle and its antiparticle, an electron and a positron, while parameters like energy, momentum, charge and so on are conserved. The photon must interact with a nucleus for the conservation laws to hold when creating an electron-positron pair.

Figure 2.6 illustrates electron-positron pair production by a photon. The absolute minimum photon energy E_γ that can theoretically allow this is the energy required to create the rest masses of the electron and the positron: $E_\gamma = 2m_e c^2 = 1.022$ MeV. The kinetic energy of each of the electron and the positron, E_{e^-} and E_{e^+} is half the excess energy of the photon:

$$E_{e^-} = E_{e^+} = \frac{E_\gamma - 1.022 \text{ MeV}}{2} \tag{2.4}$$

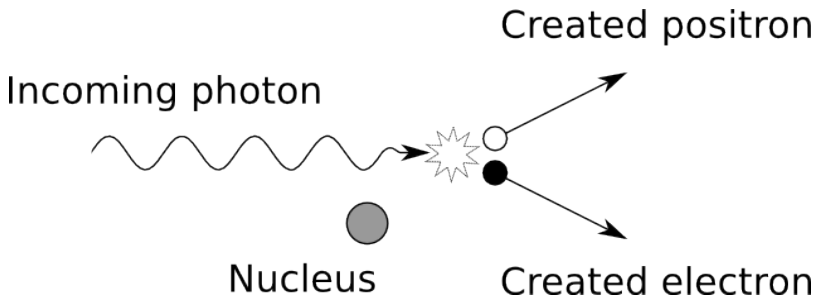

Figure 2.6: A photon interacts with a nucleus and creates a positron and an electron. The photon is destroyed, or transformed, in this process. Quantities such as momentum and energy are conserved for this process.

Pair production can be disregarded for our laboratory sparks at a voltage of 1 MeV, because the process requires minimum photon energies of 1.022 MeV and it is highly unlikely that any such photons will appear (except for cosmic ray sources).

2.1.3 Multiplication and scattering of energetic electrons

All the processes described above can occur together under certain circumstances. Let us assume we have a high energy electron in air, without an electric field. It will propagate, and interact with the air as described above. It may ionize atoms by freeing one or more electrons in a collision. Freed electrons may have enough energy to ionize even more atoms. In addition, the electrons may give off radiation due to bremsstrahlung, and if the photons have enough energy, they may produce electron-positron pairs, or at least ionize atoms by photoelectric absorption. The photons may also give off energy to electrons through Compton scattering. The photons and particles will be scattered away from the original particle's direction.

Thus, we can go from one initial particle to a large number of particles. This is called an *avalanche process*, see Figure 2.7. It is of course highly dependent on the energy of the initial particle. In subsection 2.2.1, this concept will be explored further for a situation where an electric field is present.

2.1.4 Runaway electrons

Wilson (1925) was the first to describe what we today call *runaway electrons*. The main idea is that the resistance electrons experience when moving through air varies with the kinetic ener-

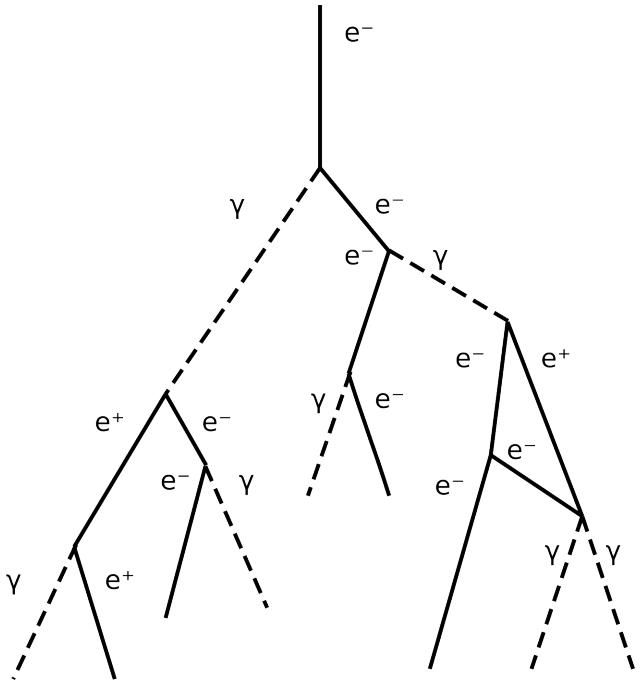

Figure 2.7: An energetic electron can cause an avalanche of secondary particles and photons by interacting with the air.

gies of the electrons, and there is a range of energies in which the resistance decreases for increasing energy. If a strong enough electric field is present, electrons may be accelerated due to the field, and gain more energy from this than they lose due to collisions and other interactions with the air. Such electrons are called runaway electrons. The loss of energy per path length is a statistical number, and is also called the effective friction force acting on the electrons, or the stopping power of the medium they are travelling in. The stopping power of dry air at standard temperature and pressure (STP) for electrons is shown by the *solid black curve* in Figure 2.8.

As shown in Figure 2.8, the friction force has a minimum value around electron energies of 10^3 keV. This minimum value corresponds to an electric field strength of 218 kV/m (Dwyer et al., 2012). This field is called the break-even field, since it's just strong enough to keep electrons of the right energy going. Dwyer (2003) showed by simulations that the actual minimum value for a field to drive electrons would be approximately 284 kV/m due to elastic scattering, because the electrons may change direction and no longer be aligned with the field. For other electron energies, larger field strengths than the numerical value for the friction force are also required. For electron energies lower than 10^3 keV, the average deflection of an electron due to Coulomb collisions will be greater, and thus the extra field strength required for continuous drift is greater.

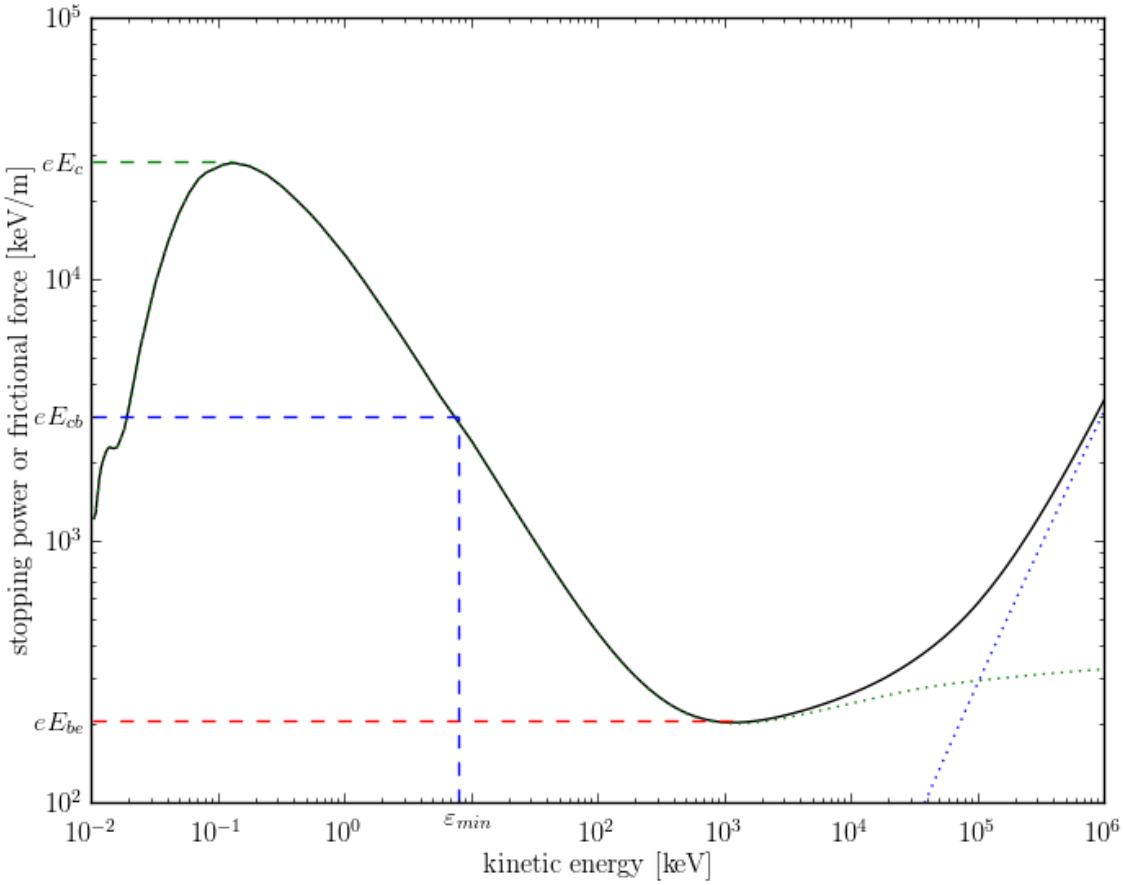

Figure 2.8: (Color) The effective friction force experienced by free electrons in dry air at standard temperature and pressure as a function of their kinetic energy. The *solid black curve* shows the stopping power, or friction force, experienced by electrons in air. This is the sum of the radiative stopping power and the collision stopping power, shown by a *dotted blue curve* and a *dotted green curve* respectively. The blue curve is the upper curve of the two on the far right. Radiative stopping power is the average energy loss per path length due to emission of bremsstrahlung. Collision stopping power is the average energy loss per path length due to Coulomb collisions that excite and ionize atoms. The *horizontal dashed blue line* in the middle shows the conventional breakdown electric field strength E_{cb}, and the *vertical dashed blue line* shows the corresponding kinetic energy ε_{min}, which is approximately 8 keV. ε_{min} is the minimum energy required for an electron to experience relativistic runaway, assuming electric fields can not be stronger than E_{cb}. The *dashed red line* below shows the break-even electric field strength E_{be} which is just barely strong enough to drive an electron that loses energy just to inelastic scattering and bremsstrahlung. The *dashed green line* on top shows the critical electric field strength E_c that would feed an electron energy at the same rate as the frictional loss rate. A field stronger than E_c would accelerate all electrons to relativistic energies. The data for the curves are from the International Commission on Radiation Units and Measurements. We collected the data from the National Institute for Standards and Technology (NIST) at `http://www.nist.gov/pml/data/star/`.

Rakov and Uman (2003) states that an electric field strength of approximately $3 \cdot 10^6$ V/m causes conventional breakdown and an electrical discharge, a spark. The conventional understanding is that any electric field stronger than this would discharge immediately, and thus be unstable. According to this understanding, electrons can not be accelerated to high energies by an electric field. The reason is that the field strength required to overcome the maximum frictional losses is around $3 \cdot 10^7$ V/m, as seen in Figure 2.8. An electron would require a field much stronger than the conventional breakdown field to increase its energy from rest to above ε_{min}. If such acceleration were to happen, the process would be called *cold runaway* or *thermal runaway*.

Dwyer et al. (2005b) detected $30 - 150$ keV x-rays from 1.5 MV laboratory sparks of around 1.5 m length. The only reasonable explanation is that they are caused by bremsstrahlung from energetic electrons. If a homogenous field of 10^3 kV/m were to accelerate electrons from rest, they would not get to energies higher than a few eV according to Figure 2.8, where they would not even show up on the left side. It is obvious that something happens to accelerate the electrons past the peak of the friction curve, and that does not fit into the simple model described above. One theory of how this may happen is discussed in the following section on streamers and leaders.

2.1.5 Streamers and leaders

Streamers and leaders are part of the process of electric breakdown of air. They form an electrically conductive channel that develops into an electrical spark. A streamer is *a self-propagating electrical discharge that propagates forward by the action of electron avalanches generated at the head of the streamer thanks to the high local electric field created by the concentration of charges at the head of the streamer* (Cooray et al., 2009). The two kinds of streamers are called positive and negative, and they develop in different ways. For natural lightning, the term leader is commonly used for the conducting channels, while both leader and streamer are used for laboratory sparks in the literature.

Streamers play an important role in the breakdown of laboratory spark gaps. They propagate between the electrodes, forming a conductive channel. When streamers bridge the gap, the current will greatly increase, the potential difference is discharged, and the breakdown is

complete.

For further depth in this topic, the reader is advised to look up Cooray (2003) and Gallimberti et al. (2002).

Positive streamer formation

Figure 2.9 shows the formation of a positive streamer. There is a positive charge region at the top and a negative charge region at the bottom of each of the four images, indicated by the horizontal lines.

Image a): An electron avalanche initiated by the electric field set up between the charge regions. The heavier positive ions do not move much while the electrons accelerate towards the positive charge region.

Image b): When the front of the avalanche reaches the positive charge region, the electrons are absorbed by that region, leaving behind a region of positive charges. The electrons emit photons by bremsstrahlung or by recombinating with a positive ion. These photons can ionize the air and cause even more avalanches.

Image c): The next bursts of electrons are partially absorbed by the positive charges in this region, and the region may even set up a strong enough electric field to ionize the air nearby and pull in electrons. This extends the plasma region growing from the impact of the initial avalanche, and it causes a new region to be positively charged, and the process continues.

Image d): The continuing process of the positive charge region at the end of the streamer ionizing the nearby air within a certain range. For simplicity, photons creating new avalanches are not shown here.

Negative streamer formation

Figure 2.10 shows the formation of a negative streamer. In each image, there is a negative charge region at the top and a positive charge region at the bottom.

Image a) shows an initial electron avalanche propagating away from the negative charge region. The electrons stop when the field is not strong enough to drive them further. They will attach to the neutral gas, and the space charge stays in place.

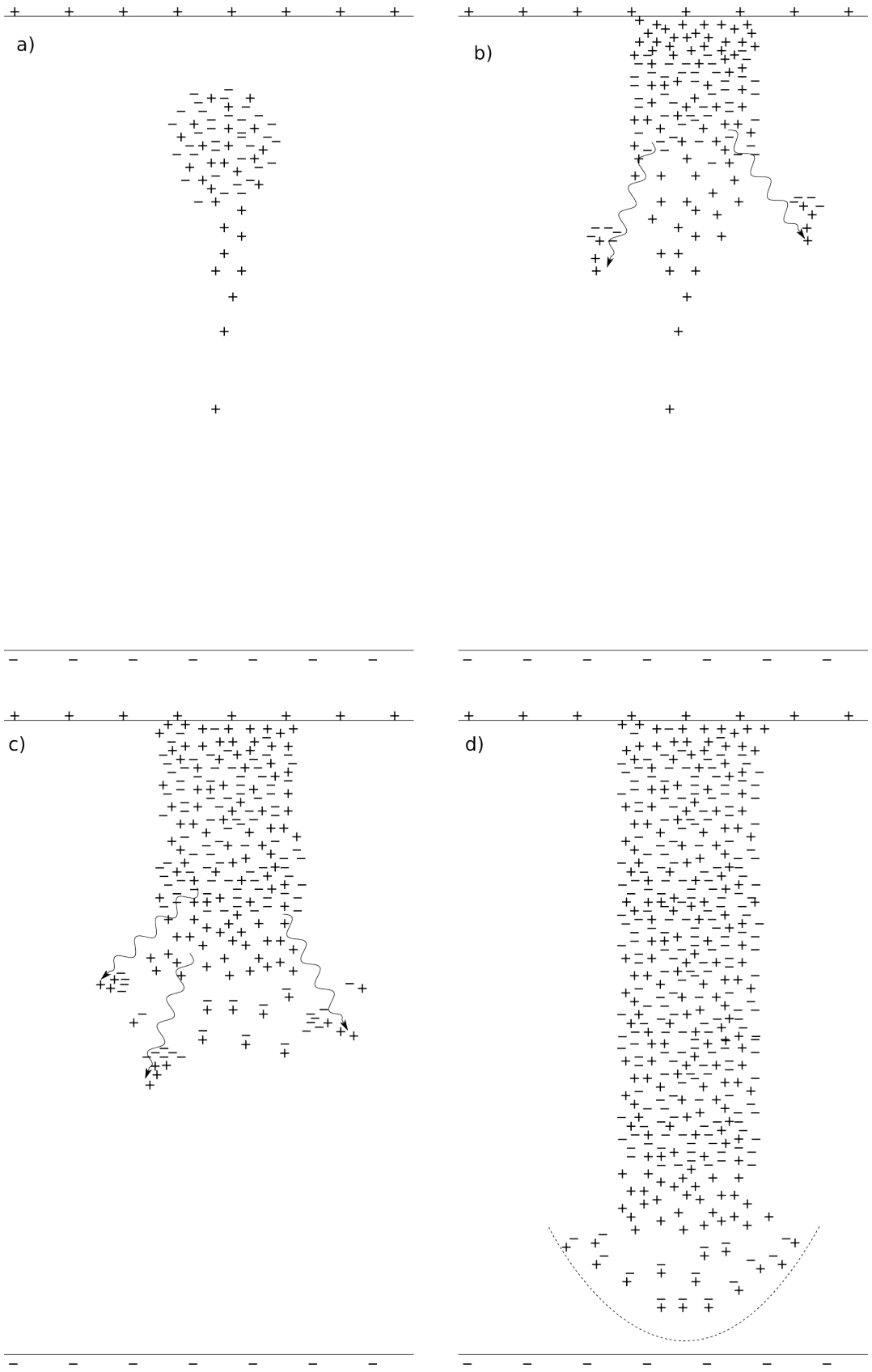

Figure 2.9: Formation of a positive streamer. Refer to the text for a description of the phases of formation. This figure is based on figures in Cooray (2003).

Image b) shows that the positive charges left behind may attract more avalanches. The electrons will partially neutralize the positive ions left behind by the initial avalanche. This process may be repeated, and makes the streamer grow towards the negative charge region as a positive streamer.

Image c) shows that the streamer is connected to the negative charge region. The tip of the streamer has a net negative charge that is supplied from the negative charge region on the top of the image, attracted by the positive charges left behind by an avalanche at the bottom of the image, and repelled by the negative charge region. There is also a new avalanche between the streamer tip and the previous avalanche.

Image d) shows that the streamer has extended even further, and that there is a new gap between the end of the streamer and the avalanche in front. This gap will fill later, and extend the streamer by another step.

For simplicity, this figure does not show photons initiating secondary avalanches. There will be such avalanches, as in Figure 2.9.

The field set up between charge regions is the energy source for the electrons and photons in our experiments, since we are using a negative high voltage electrode.

2.2 Introduction to terrestrial gamma-ray flash physics

In this section we'll introduce some theory not related to laboratory sparks, but that will still be useful for understanding what this thesis work is a part of. This section will also illuminate the discussion that will come later.

2.2.1 Runaway relativistic electron avalanches

Wilson (1925) reported electrons with certain energies in electric fields of certain strengths may have a higher rate of energy gain from the field than the rate of energy loss to the air around it, see Figure 2.8. Such electrons later became known as runaway electrons. Gurevich et al. (1992) showed that the runaway electrons may cause a multiplication of electron numbers due to elastic electron-electron scattering (Møller scattering) with atomic electrons. These interactions may transfer enough energy to the atomic electrons to eject them from the atom. Some of them

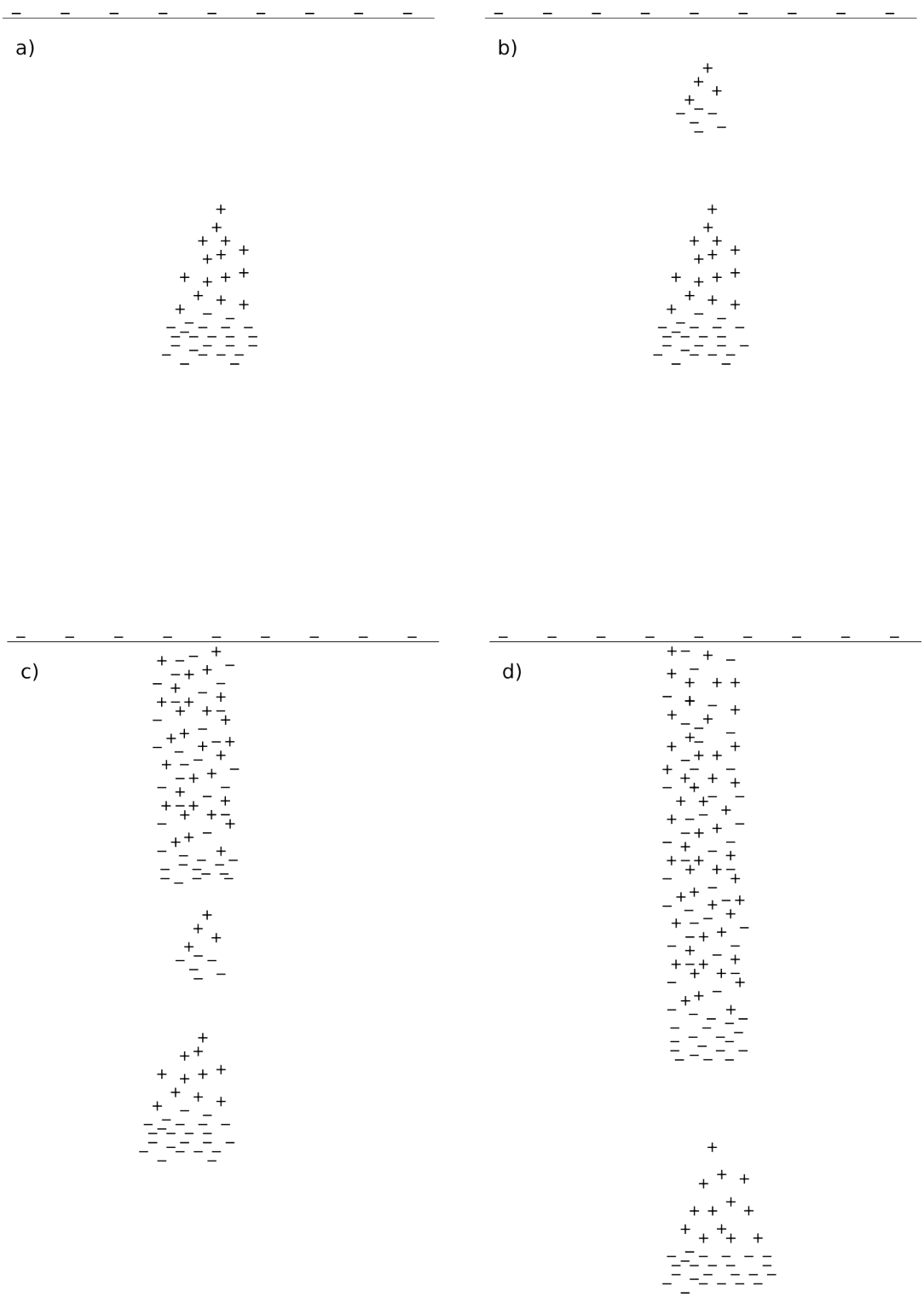

Figure 2.10: Formation of a negative streamer. Refer to the text for a description of the phases of formation. This figure is based on figures in Cooray (2003).

may even get enough energy to be in the runaway range. Thus the number of runaway electrons have multiplied, and they can in turn create a new and even larger generation of electrons. This kind of exponential growth is called avalanche multiplication. Since the electrons reach energies where relativistic effects are noticeable (and important), the full name of the phenomenon is relativistic runaway electron avalanche (RREA). Gurevich and Zybin (2001) performed a thorough theoretical study of RREAs.

The length required for the number of electrons to increase by a factor of e, e-fold multiplication, is called the *avalanche length* or the *avalanche growth length* λ, while the timescale for avalanche growth is τ. Dwyer (2003) and Coleman and Dwyer (2006) performed RREA simulations, and estimated that at sea level air density, the avalanche length and time is given by

$$\lambda = \frac{(7300 \pm 60)\ \text{kV}}{E - (276 \pm 4)\ \text{kV/m}} \tag{2.5}$$

$$\tau = \frac{(27.3 \pm 0.1)\ \text{kV}\mu\text{s/m}}{E - (277 \pm 2)\ \text{kV/m}} \tag{2.6}$$

where E is the electric field strength. These equations can be scaled for other air densities. The numbers were confirmed by independent simulations by Skeltved et al. (2014).

Coleman and Dwyer (2006) also estimated the propagation speed of the avalanches to be around $v = 2.65 \cdot 10^8$ m/s $= 0.89c$, where c is the speed of light. This number is pretty accurate for large variations of the electric field strength. This speed is the avalanche speed along the field, not the actual particle speeds, which can be very close to the speed of light.

If we assume that the flux of original energetic electrons is F_0, the flux of the RREA after a distance L is by definition

$$F_{\text{RREA}} = F_0 \exp(\xi), \quad \text{where } \xi = \int_0^L \frac{dz}{\lambda} \tag{2.7}$$

In a homogenous electric field, the avalanche length λ is constant, and this simplifies to

$$F_{RREA} = F_0 \exp(L/\lambda) \tag{2.8}$$

We will describe the experiment setup in detail in chapter 3. For our setup with a potential

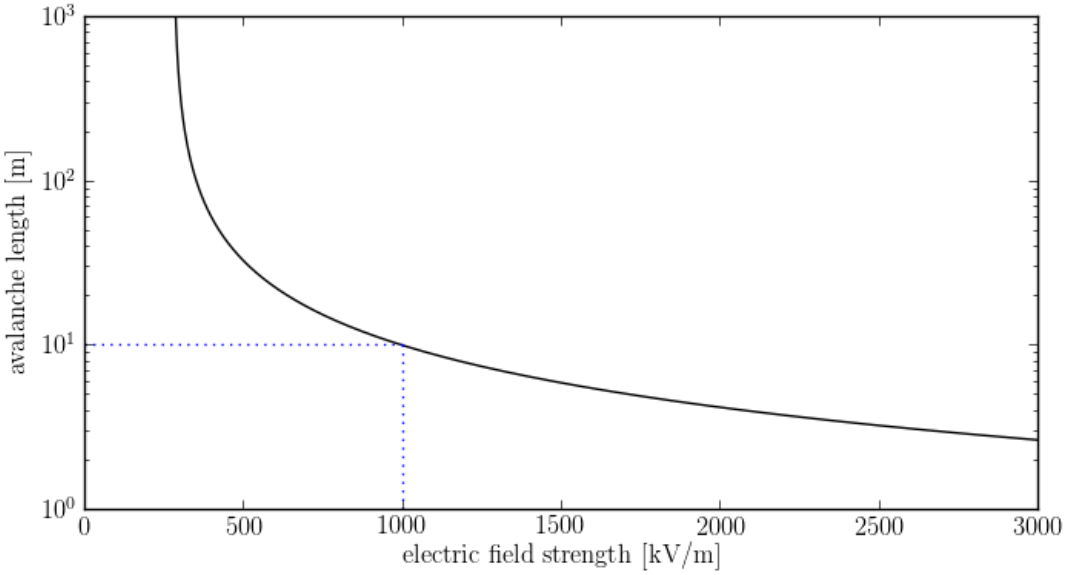

Figure 2.11: (Color) The length for e-fold multiplication of electrons for relativistic runaway electron avalanches (RREAs) as a function of the electric field strength, Equation 2.6. The *dotted blue lines* indicate that the avalanche length for a 1000 kV/m electric field is 10 m.

difference of up to 1 MV, and a spark gap of 1.07 m, the average electric field strength grows to around 1000 kV/m as the potential builds up. According to Figure 2.11, the avalanche length for our experiments is around 10 m or more, and we can neglect RREAs in our experiments. There is a possible exception regarding very strong electric fields in very small volumes, see subsection 2.2.4.

The average energy of electrons in a RREA is 7.3 MeV after a few avalanche lengths (Dwyer et al., 2012; Dwyer, 2004). The energy spectrum for runaway electrons per unit energy, for electron energies of a few hundred keV to several MeV, is given by Dwyer et al. (2012) as

$$f_{re} = \frac{F_{RREA}}{7.3\text{ MeV}} \exp\left(\frac{-\varepsilon}{7.3\text{ MeV}}\right) \tag{2.9}$$

where ε is the electron energy.

2.2.2 Source mechanisms of terrestrial gamma-ray flashes

The average spectrum recorded by the RHESSI spacecraft were compared to simulations of energetic electrons at different source altitudes by (Dwyer and Smith, 2005). They found that the

number of runaway electrons at the source should be about 10^{16} for a source at 21 km altitude and about 10^{17} for a source at 15 km altitude. Hansen et al. (2013) found that initial numbers of photons should be 10^{16} for 20 km source, and 10^{17} for 15 km source. Skeltved et al. (2014) found that the ratio of the numbers of energetic photons to the number of energetic electrons is between 0.1 and 1. Therefore, the numbers found by Dwyer and Smith (2005) and Hansen et al. (2013) fit well.

For a RREA to start, there must be at least one electron with energy above the threshold where the rate of energy gain is equal to the rate of energy loss (see subsection 2.1.4). The source electron(s) may stem from different sources. On page 5 of Dwyer (2008), the author states that the maximum flux of atmospheric cosmic rays and other sources of energetic background radiation is 10^4 $m^{-2}s^{-1}$ at thundercloud altitudes. The number is taken from Hillas (1972). Carlson (2009) states that $\sim 10^7$ is the largest justifiable seed population for RREA, based on work done by Carlson et al. (2008).

Dwyer (2004) found that the average energy an electron gains per avalanche length during RREA is about 7 MeV. Since RHESSI and Fermi has detected single photons of several tens of MeV (Smith et al., 2005; Marisaldi et al., 2010), at least three avalanche lengths are needed. Dwyer (2008) used reasonable assumptions for source cross-sectional area (100 km^2) and three avalanche lengths in the field region (electron multiplication of $e^3 \approx 20$). With an estimated flux of cosmic rays and other sources of energetic background radiation of 10^4 $m^{-2}s^{-1}$, there is a discrepancy of $\sim 5 \cdot 10^5$ or more. The total number of avalanche lengths required to reach an appropriate number by electron multiplication is 16. That means the total potential drop would have to be over 100 MV. Potentials this large are not as common as TGF observations, so comic rays and other background sources can not explain RHESSI TGFs alone. Therefore, other mechanisms must be at work to greatly increase the number of energetic seed electrons that can undergo RREA.

The two theories of how the number of avalanches might be amplified are the theory of relativistic feedback and the theory of thermal runaway from streamers and leaders. These will be explained next.

2.2.3 Relativistic feedback

The mechanism of relativistic feedback was introduced by Dwyer (2003). The main idea is that positrons and photons moving backwards relative to the RREA's general direction and can start new avalanches, see Figure 2.12. Photons may move backwards if they are created with velocity backwards. Positrons will move backwards relative to the avalanche, since the force they will experience from the electric field will work in the opposite direction of the corresponding force on the electrons. If the positrons and photons react and annihilate within the zone of the electric field, new electrons may be created, and thus new avalanches, which may themselves cause more feedback. If the positrons travel some distance before annihilating, they can even start avalanches by colliding with and transferring enough energy to electrons through Bhabha scattering. The relativistic feedback mechanism can become self-sustained, and stops relying on external seed particles. This depends on the feedback factor γ described by Dwyer (2003). If on average at least one new avalanche is started by each avalanche from the original seed particles, the process is self-sustaining. This lasts until the electric field is discharged. Dwyer (2007) showed that the discharge of an electric field can happen in less than a millisecond, and that the total flux of energetic electrons can be up to a factor of 10^{13} times larger than the flux from a RREA.

This process can rapidly provide a dramatic multiplication of the number of energetic electrons. This theory helps explain large bursts of x-rays produced by rocket-triggered lightning (Dwyer et al., 2003).

Dwyer (2003) also determines the upper limit for stable electrical fields as a function of the length of the field region. Note that this does not exclude the possibility of higher field strengths, but it does state that those fields will be unstable.

According to Dwyer (2008), Monte Carlo simulations that include relativistic feedback show that the maximum reasonable avalanche multiplication factor for realistic conditions is 10^5, and that $2 \cdot 10^4$ might be a more reasonable number. This also shows that many earlier simulations without relativistic feedback have greatly overestimated the avalanche multiplication factor.

In his M.Sc. thesis, Skeltved (2013) used the Geometry and Tracking 4 (GEANT 4) simulation toolkit to study RREAs in air and to study the relativistic feedback theory by comparing RREA parameters with existing results from other simulations. One of the results was that for a ho-

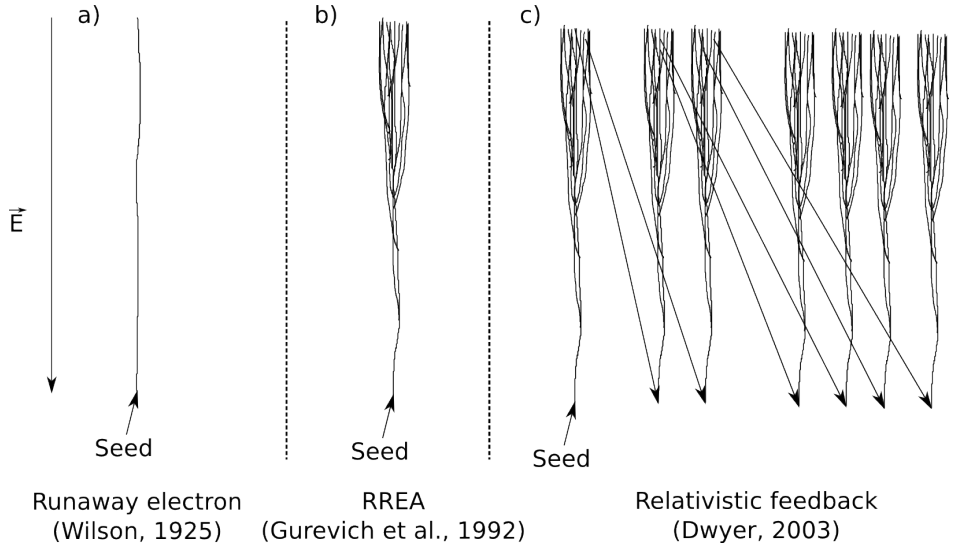

Figure 2.12: Schematic showing the evolution of theories leading to relativistic feedback. a) Runaway electron as described by Wilson (1925). b) Runaway relativistic electron avalanche (RREA) as described by Gurevich et al. (1992). The seed electron can create new energetic electrons, which can themselves become runaway electrons. c) Relativistic feedback seeding additional RREAs by photons or positrons travelling in the opposite direction of the electrons, as described by Dwyer (2003). This figure is inspired by figure 9 in Dwyer et al. (2012).

mogeneous electric field of 1 MV/m, in a 100 MV potential, the number of electrons from one RREA is 10^4. Using Equation 2.8, we get $\approx 10^6$. This indicates that earlier works may have overestimated the number of electrons. The number is in agreement with the numbers presented by Dwyer (2008).

2.2.4 Thermal runaway

The thermal runaway (or cold runaway) theory for production of TGFs was introduced by Dwyer (2004), but there was an issue regarding the necessary electric field strength. Moss et al. (2006) simulated the electric fields at streamer heads, which can be around ten times the conventional breakdown field strength E_{cb}, and found that electrons in the streamers could be accelerated to energies of 2-8 keV. This is important, because when this number is related to Figure 2.8, we see that the electrons were accelerated past the peak of the friction curve. This allows for relativistic runaway electrons without very high energy seed electrons. Depending on the potential and the electric field configuration, the high-energy electrons ejected from streamer tips can be accelerated even further, to several tens of MeV, and can be the source of TGFs.

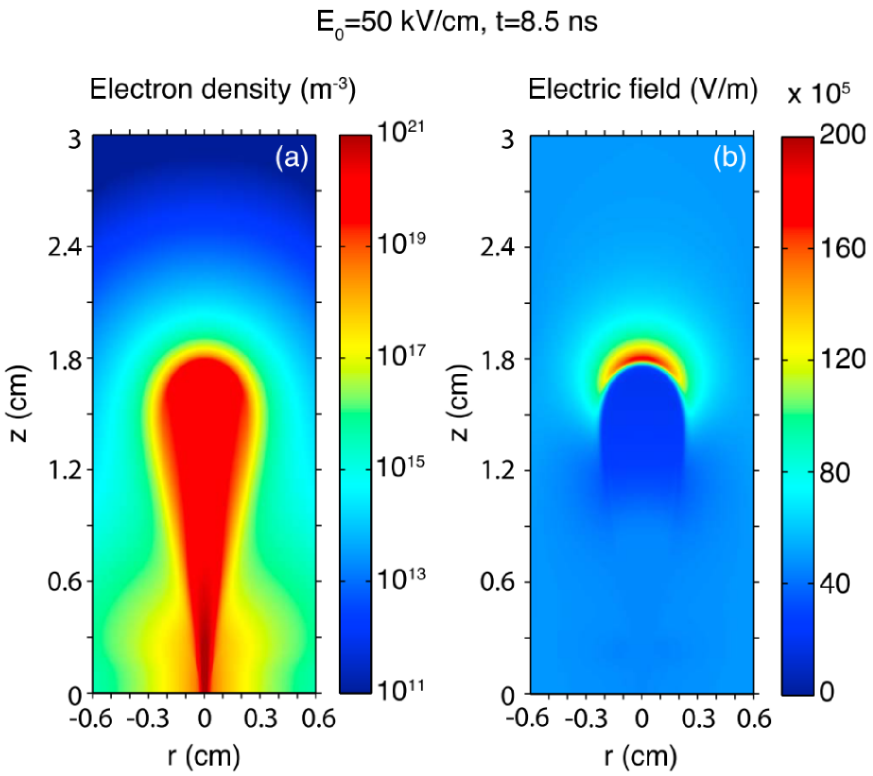

Figure 2.13: (Color) Simulation results from the work of Celestin and Pasko (2011). The image on the left shows the electron density configuration in a negative streamer, while the image on the right shows the electric field configuration. This figure is a copy of figure 1 in Celestin and Pasko (2011).

Celestin and Pasko (2011) expanded on the work done by Moss et al. (2006), and found that streamer tips can accelerate electrons to as much as 100 keV. Most electrons should end up with energies of several tens of keV, and the peak probability is around 60 keV. This is well beyond the limit of 8 keV that corresponds to the conventional breakdown field strength, see Figure 2.8. Thus, this process produces electrons with energies high enough to run away in electric fields weaker than the conventional breakdown field strength.

Figure 2.13 shows that the electric field generated by a negative streamer is much stronger than the ambient field E_0. The number of streamer tips are estimated to be 10^6, which brings the total number of electrons to around $10^{14} - 10^{16}$. If these electrons are then accelerated in the ambient electric field of the thundercloud through a few avalanche lengths, the number of electrons is suitable to cause TGFs.

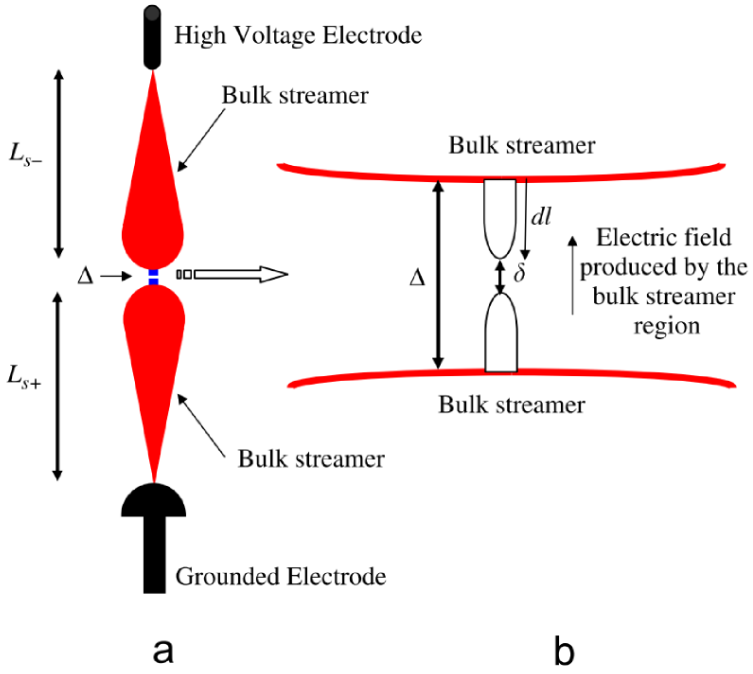

Figure 2.14: (Color) When streamers have ionized the air in a spark gap, a strong electric field can be set up between the streamer lobes. This figure is a copy of figure 3 in Cooray et al. (2009).

Implications of thermal runaway for long laboratory sparks

The population of electrons at several tens of keV ejected from streamer tips can be further accelerated in the field of a collapsing spark gap. When parts of the gap is ionized, a large part of the potential difference will be applied to a short distance in the air, see Figure 2.14. This can cause a strong field that can increase the energy of electrons to a few hundred keV, according to work by Cooray et al. (2009).

Chapter 3

Experiment setup

The experiment was carried out in the high-voltage laboratory at Eindhoven University of Technology (TU/e) in The Netherlands during the week of 21st to 27th of January 2013. In total, 950 sparks of 1 MV voltage were generated. A series of similar experiments had been carried out a year earlier, but with weak results, mostly due to a low number of sparks for each experimental setup.

A Marx generator generated the voltage necessary for sparks to form in the gap between the electrodes. Detectors made from scintillating fibers were placed in different geometrical configurations around the spark gap to examine different characteristics of the electrons produced by the electric field and processes described in chapter 2. Two $LaBr_3(Ce^+)$ detected x-rays during the experiments. These data are not the focus of this thesis, but they are being analyzed by others. The $LaBr_3(Ce^+)$ detectors and the oscilloscopes were located inside a metal cabinet shielding them from the influence of the strong electromagnetic field during sparks. Two high-speed cameras photographed the area around the high voltage electrode during the streamer build-up phase.

3.1 Laboratory layout

Figure 3.1 shows the Marx generator that generates the voltage, the electrodes and the spark gap. The electrodes and the detectors are shown in Figure 3.2. The spark gap is the volume of air between the two spiky metal electrode tips on the metal dishes on the right side of the image.

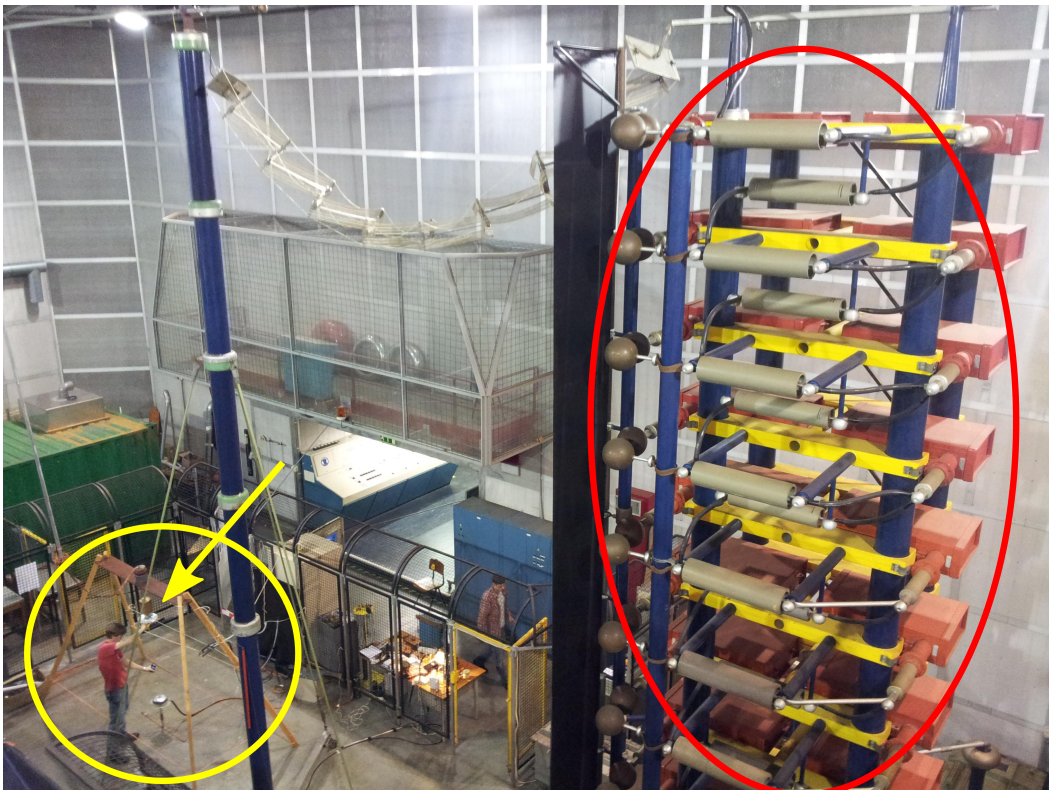

Figure 3.1: (Color) Overview of the laboratory. The big structure in the *red ellipse* on the right is the top of the Marx generator. In the *yellow circle* in the lower left, there is a wooden structure. The horizontal board on top supports the high voltage electrode, see the yellow arrow. The grounded electrode sticks up from the floor. See Figure 3.2 for a closer look on the electrodes and the spark gap. Between the Marx generator and the blue vertical column on the left side of the image, we see an open, yellow door, and a black fence. These are part of the safety measures of the laboratory. On the far side of the fence is the safe area, where the experimenters are during sparks.

The Marx generator is the large structure with the red boxes in the background.

3.2 Equipment

This section describes some different pieces of the equipment used for the experiments of this thesis.

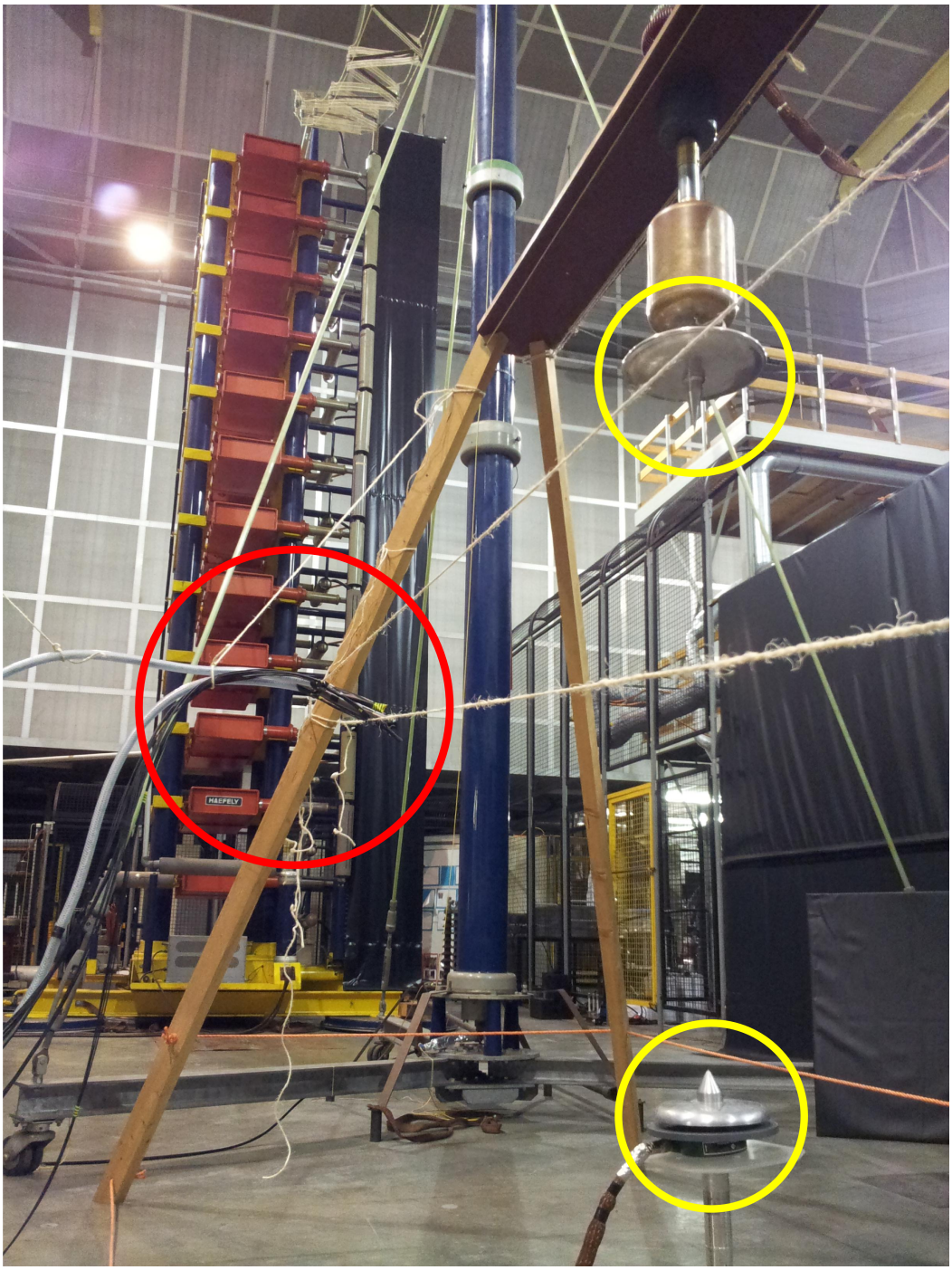

Figure 3.2: (Color) On the right side we see the two electrodes, the spiky metal pieces on the metal dishes in the two *yellow circles*. The bottom electrode is grounded. The electrode hanging from the wooden board is the high voltage electrode, connected to the Marx generator, which can be see in the background. Several pieces of white string are used to place the detectors in desired locations relative to the electrodes. The detectors can be seen in the *red circle*, with the optical fibers leading out of the left side of the picture towards the cabinet.

3.2.1 Marx generator

The Marx generator was the central machine in the experiment. Several capacitors were charged to a certain voltage in parallel, before suddenly switching to a series connection to cause a high voltage output of approximately 1 MV. The Marx generator generated standard lightning pulses with 1.2/50 µs rise/fall time.

3.2.2 Electrodes and spark gap

The voltage supplied by the Marx generator was applied to the pair of electrodes seen in Figure 3.2. Each electrode was shaped like a small, pointy cone on a dish. This was done to intensify the electric field, and differs from the rod-plane or sphere-plane geometries found in several previous scholarly articles (usually also using much shorter gap lengths). The length of the vertical spark gap between the electrodes' tips was 1.07 m long.

3.2.3 Scintillating fiber detectors

Due to the strong electric field around the spark gap we needed a detector that did not use electronics directly, or at least electronics shielded from electromagnetic radiation. We wanted to avoid any metal components close to the spark gap, because that would most likely affect the evolution of the spark. Therefore, plastic detectors were ideal. In short, each detector consists of five scintillating fibers, each spliced with an optical fiber, all together connected to a photomultiplier tube and an electrical cable to an oscilloscope.

We constructed four detectors from scintillating plastic fibers, and we used two detectors constructed after the same principles during the previous series of experiments. The matter in the scintillating fibers is excited when they absorb energy deposited by electrons, photons, and other particles that pass through or stop inside the fiber. This energy is released as visible light in the fiber. We used optical fibers to transmit the light to photomultiplier tubes. We spliced the scintillating and optical fibers as indicated in image a) in Figure 3.3. The ends of both fibers were polished, and they were glued inside the heatshrink plastic to hold the ends tight together. Image b) shows how of five fibers are grouped together to form a sheet of effective area. These detectors allowed us to avoid placing any electronics or metals close to the spark gap, exposed

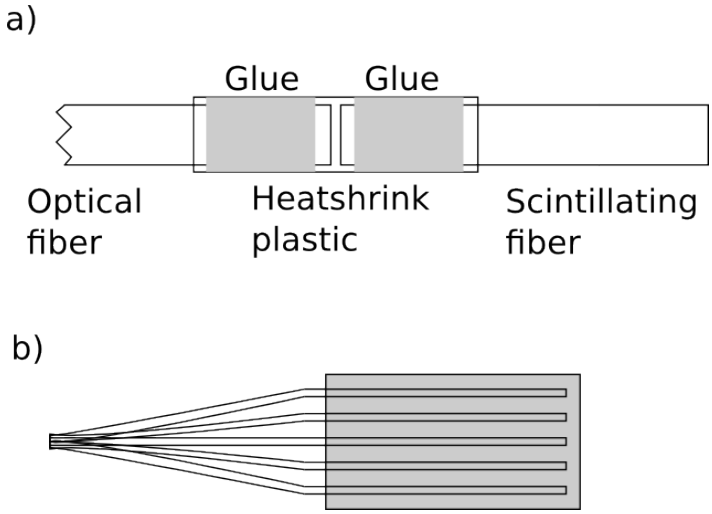

Figure 3.3: a) Splicing of scintillating fiber and optical fiber, using heatshrink plastic to hold the pieces together. Glue is applied to a section of each fiber before inserting it into the heatshrink plastic, to help hold the fibers in place relative to each other. The plastic is heated with hot air to make it shrink to hold the fibers together. b) Each detector is made up of five scintillating fibers held together in a fan formation with a thin layer of black plastic and tape shown in gray. In reality, the five fibers were closer together than shown in this figure. They are spaced here to illustrate the principle. The optical fiber ends are gathered into a bunch that are connected to the cabinet with the photomultiplier tubes and the oscilloscopes for readout.

to the strong electromagnetic field generated by the voltage and spark.

The length of the scintillating fiber was 10 cm, with approximately 9 cm exposed, because 1 cm was covered by the plastic that held the scintillating and optic fibers together. The length of the optic fiber was 3 m. The refractive index of the optical fiber is unknown, but as 1.62 is a typical value, we assume this value holds for our fibers. This causes a time delay of 16.2 ns between something hitting the detectors and the light reaching the photomultiplier tubes. The diameter of the scintillating fibers is 1 mm. The plastic that covers the sensitive part of the detector is 0.15 mm thick.

We refer to the four new detectors we made as UB1, UB2, UB3, and UB4. The two old detectors are referred to as H1 and H3. The fiber detector H3 was introduced after the initial 150 calibration sparks.

Oscilloscope	Channel 1	Channel 2	Channel 3	Channel 4
1	Voltage	Ground electrode current	High voltage electrode current	Camera
2	LaBr1	LaBr2	H1	H3
3	UB1	UB2	UB3	UB4

Table 3.1: The channels of the oscilloscopes were dedicated to the instruments as shown in this table. Voltage is the voltage measured over the high voltage electrode. Camera is the camera shutter. LaBr1 and LaBr2 are the two x-ray detectors. H1 and H3 are fiber detectors made during our previous series of experiments. UB1-4 are the four new fiber detectors.

3.2.4 LaBr x-ray detectors

Two $LaBr_3(Ce^+)$ scintillator detectors inside the shielded cabinet detects x-rays coming in through a 550 µm aluminum sheet window. These detectors are located significantly further away from the spark gap than the fiber detectors. The detectors were in the same location for the entire series of sparks, and the data could contain interesting information. This is being investigated by other researchers. For simplicity, these detectors are referred to as LaBr-detectors.

3.2.5 Oscilloscopes

In total, we used three oscilloscopes. Two of them had a sampling frequency of 5 GHz, the third oscilloscope's frequency was 10 GHz. This corresponds 10,000 and 20,000 data points in the 2 µs window we used. Each oscilloscope could read and store data from four channels. See Table 3.1 for overview, and Figure 3.4 for an example of the oscilloscope display.

To accurately compare signals in the different oscilloscopes and channels, we need to know what time offsets apply to different signals. Oscilloscope 1 is triggered by the Marx generator, and oscilloscopes 2 and 3 are triggered by oscilloscope 1. Therefore, oscilloscopes 2 and 3 will have a lower time reading than oscilloscope 1. The difference is 30 ns for oscilloscope 2 and 40 ns for oscilloscope 3. in addition, the instruments in the different channels have different offsets, like instrument response time and travel time from the instrument to the oscilloscope. A summary is given in Table 3.2. The table also provides an overview of the scaling factors for the different instruments, except for the fiber detectors, as these have been calibrated only relative to each other.

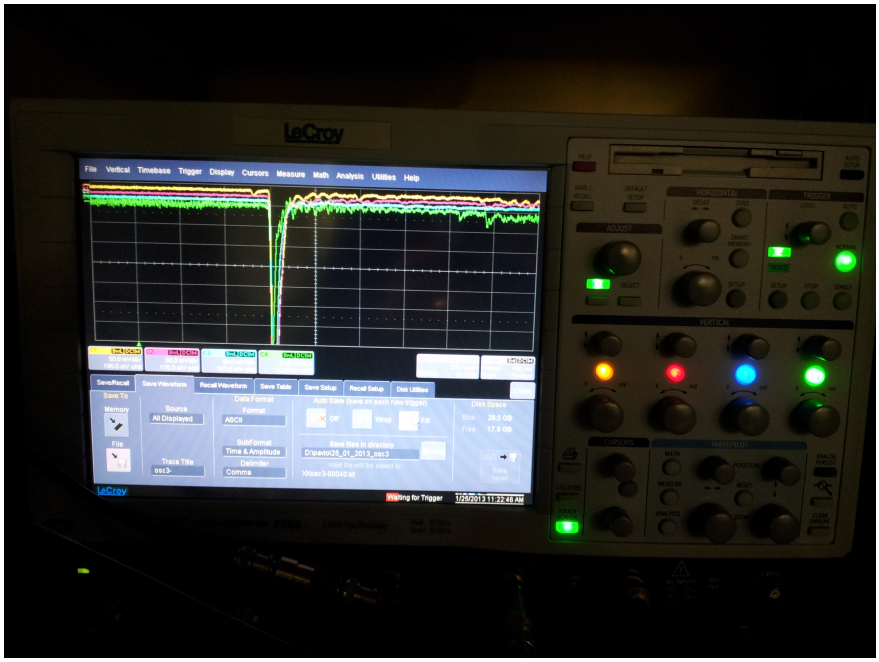

Figure 3.4: (Color) A photograph showing the display of one of the oscilloscopes for one of the sparks. The four colored graphs represents the four UB fiber detectors. For this particular spark, all detectors were hit hard, and all four channels are saturated.

Oscilloscope-Channel	Instrument	Scaling factor	1 equals	Offset [μs]
1-1	Voltage	0.08	1 MV	−0.0519
1-2	Ignd	0.8	500 A	−0.0336
1-3	IHV	9.8	500 A	−0.220
1-4	Camera	-	-	−0.0463
2-1	LaBr1	13.9	1 MeV	−0.053 + 0.030
2-2	LaBr2	9.6	1 MeV	−0.053 + 0.030
2-3	H1	?	?	−0.0645 + 0.030
2-4	H3	?	?	−0.0505 + 0.030
3-1	UB1	?	?	−0.069 + 0.040
3-2	UB2	?	?	−0.069 + 0.040
3-3	UB3	?	?	−0.069 + 0.040
3-4	UB4	?	?	−0.069 + 0.040

Table 3.2: The offsets in time for different instruments and oscilloscopes, and the scaling factors for converting the oscilloscope readouts to physical parameters. The numbers take into account instrument response times and signal travel times. All the question marks for fiber detectors indicate that we do not know the scaling factors for these detectors. As will be explained in section 5.5, we have done a relative calibration, but not absolute calibration, for these.

Hamamatsu R6231-01 photomultiplier data		
Gain (typical)	Rise time	Transit time
$2.7 \cdot 10^5$	8.5 ns	48 ns

Table 3.3: The gain is the amplification and it shows how much the signal is amplified. It is related to how easy it is to separate the signal from the electrical noise. The rise time is the time required for the signal to rise from 10 % to 90 % of the peak value. The transit time is the time from the incoming light enters the photomultiplier to the signal hits its peak value. The data are collected from the manufacturer's specifications: `http://www.hamamatsu.com/jp/en/R6231-01.html`

The dynamic ranges of the different channels of the oscilloscopes were changed several times throughout the week of experiments, because the signals from some sparks saturated the oscilloscopes. We tried to keep the sensitivities as high as possible to be able to see weaker signals, while also trying to avoid saturation. The actual data output is described in chapter 4.

3.2.6 Photomultiplier tubes

A photomultiplier tube is a highly light-sensitive device that outputs a greatly amplified, but proportional, signal relative to the number of photons that enters it. The photomultipliers used for fiber detectors were of the type Hamamatsu R6231-01. Some data for this photomultiplier provided by the manufacturer can be found in Table 3.3.

Each group of five optical fibers was connected to one photomultiplier. The ends of optical fibers (see Figure 3.3) were inserted through small holes in the photomultipliers container. These holes were closed by filling the gaps with black paint to make sure no light got into the container except for through the fibers. The PMTs were connected to the oscilloscopes through 1.5 m long electrical cables, which contribute with 5 ns to the time offsets.

3.2.7 Cameras

During our experiments, two cameras (see Figure 3.5) photographed the streamer zone with varying exposure times of around 50 ns. The cameras were inside a metal box, and the cables were shield by a metal hose. The images are not analyzed in this thesis. See Kochkin et al. (2012) and Kochkin et al. (2014) for analysis on similar images.

Figure 3.5: (Color) At the bottom, we see the two cameras pointed at the spark gap. At the middle and the top, we see the electrodes and the spark gap. On the left side of the photograph, we see part of the door of the cabinet.

3.3 Detector positions

During the week of experimenting, we used four different kinds of geometries for the fiber detectors. One was used to calibrate the detectors, while the other three geometrical setups were used to collect data. All setups are described below. The positions are important because different distances will cause different attenuations of electrons and photons moving from source location(s) to the detectors.

As mentioned, the LaBr detectors were in the same position for the entire series of sparks. The position was 110 cm vertically above the floor, and 206 cm in horizontal distance from the ground electrode. The spark gap is 107 cm long, and the vertical distance from the floor to the ground electrode is 55 cm. There are unfortunately inconsistencies in the other position measurements. For some of the detector position measurements, the positions are uncertain by a few cm. These uncertainties are given in the tables of detector positions.

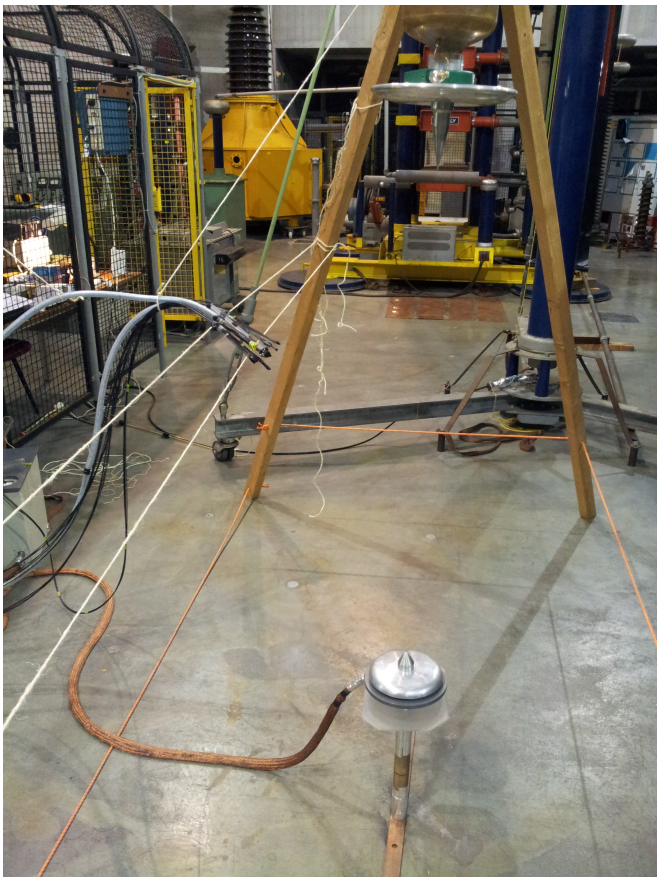

Figure 3.6: (Color) The detectors were placed right next to each other for calibration. They are turned slightly down to expose as much of their area as possible to the electrons and photons coming from an assumed source location above. The detectors are held in place by string and tape in order to avoid placing metal objects close to the spark gap.

Calibration geometry

The calibration setup is shown in Figure 3.6. All the fiber detectors were placed next to each other in the same location. This was done to justify the assumption that all the detectors would be hit by approximately the same amount of electrons and photons, and thus approximately the same total energy. At the end of the week, we ran another round of sparks with the detectors in the calibration setup. The positions are given in Table 3.4.

Radial geometry

The detectors were placed in a radial geometry. We assumed a source point close to the high voltage electrode. The idea behind this setup is that if a beam from the source location will hit

Detector	Vertical floor	Radial GND	Radial HV	Horizontal gap (calculated)
UB1-4, H1	110	84	80	62.1 ± 1.4
UB1-4, H1, H3	112	88	80	64.7 ± 2.3

Table 3.4: Detector positions for the two rounds of calibration. All measurements in cm. The positions of the detectors are given in vertical distance from the floor, radial distance from the ground electrode, radial distance from the high voltage electrode, and the calculated horizontal distance from the spark gap. The first line corresponds to the first round of calibrations. The number of sparks with this setup was 150. The second line shows the positions for the 50 sparks in the second round of calibration.

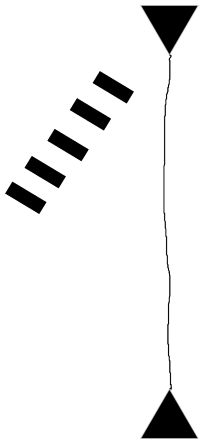

Figure 3.7: Radial geometry detector setup, seen from one side. The triangles represent the electrodes, while the rectangles represent the detectors.

all the detectors, and they will experience roughly the same intensity of incoming electrons and photons, except for the attenuation due to the travel distance. The setup is shown in Figure 3.7, and the positions are given in Table 3.5.

The greater differences between measured and calculated position for UB1 and for H1/H3 are attributed to the way we measured the horizontal distance. Since the distances from the static locations of the electrodes are easier to measure accurately, the calculated values for the horizontal distances will be used.

Azimuthal geometry

The detectors were placed in an azimuthal geometry around the spark gap, see Figure 3.8. There is no reason to assume the phenomenon on average is biased towards sending electrons and photons in certain azimuthal directions. Still, this experimental setup can help determine if

Detector	Vertical floor	Radial GND	Radial HV	Horizontal gap (measured)	Horizontal gap (calculated)
UB4	146	100	40	39	39.0 ± 2.4
UB3	140	104	60	59	57.9 ± 2.1
UB2	128	104	80	74	73.2 ± 0.8
UB1	117	109	100	93	89.5 ± 0.2
H1/H3	106	116	120	110	105.2 ± 1.0

Table 3.5: Radial geometry detector positions. All measurements in cm. The positions of the detectors are given in vertical distance from the floor, radial distance from the ground electrode, radial distance from the high voltage electrode, and horizontal distance from the spark gap (measured and calculated). H1 and H3 are right next to each other, since H3 was not part of the previous calibration. The number of sparks with this setup was 100.

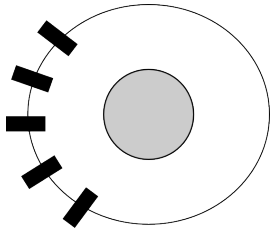

Figure 3.8: Azimuthal experimental setup, seen from above. The gray circle is the electrode, while the black rectangles are the detectors. For the two setups, we used about 15° and 37°, due to the about 20 cm and 50 cm internal distances at about 77 cm distance from the spark gap.

there is such a bias. We did three series of sparks with this setup. The second series had broader separation of the detectors, and the third also had the detectors lowered towards the floor. The positions for these experiments are given in Table 3.6. The detectors are listed in the same as the order they were placed in. That means that the detectors over and under one in the table were the neighbours of that detector during the experiment.

Polar geometry

The detectors were placed in polar geometry around the assumed source point close to the high voltage electrode, see Figure 3.9. This setup can help us find out if there is a bias regarding electrons and photons moving up or down from where they are produced. The detector positions are given in Table 3.7.

Detector	Vertical floor	Radial GND	Radial HV	Horizontal gap (calculated)
H3	125	107	84	78.2 ± 2.8
H1	125	106	84	77.5 ± 2.1
UB1	125	106	84	77.5 ± 2.1
UB2	125	106	84	77.5 ± 2.1
UB3	126	108	84	78.6 ± 2.7
UB4	127	110	84	79.8 ± 3.4
H3	124	107	92	82.8 ± 1.0
UB1	126	102	80	72.3 ± 0.9
H1	131	105	79	72.6 ± 0.1
UB2	130	106	80	74.1 ± 0.8
UB3	128	108	84	78.2 ± 1.4
UB4	129	111	88	82.2 ± 0.6
H3	92	78	97	67.9 ± 0.8
UB1	96	77	92	64.6 ± 0.5
H1	98	80	90	65.4 ± 2.1
UB2	99	80	90	65.5 ± 1.3
UB3	101	86	90	69.4 ± 3.2
UB4	97	81	88	64.3 ± 5.0

Table 3.6: Azimuthal geometry detector positions. All measurements in cm. The positions of the detectors are given in vertical distance from the floor, radial distance from the ground electrode, radial distance from the high voltage electrode, and the calculated horizontal distance from the spark gap. The internal spacing of the detectors is about 15° for the first series of 100 sparks, and about 37° for the last two series of 100 sparks. The detector positions for the three series are divided by horizontal lines in the table. The total number of sparks was 300.

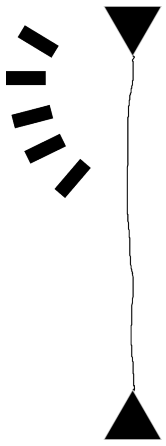

Figure 3.9: Polar geometry detector setup, seen from one side. The triangles represent the electrodes, while the rectangles represent the detectors.

Detector	Vertical floor	Radial GND	Radial HV	Horizontal gap (calculated)
UB1	149	121	76	75.5 ± 0.7
UB2	136	109	77	72.7 ± 0.2
UB3	121	96	79	68.6 ± 1.1
UB4	108	84	84	64.8 ± 0.4
H1	94	70	86	55.4 ± 2.7
H3	86	59	88	47.3 ± 2.9

Table 3.7: Polar geometry detector positions. All measurements in cm. The positions of the detectors are given in vertical distance from the floor, radial distance from the ground electrode, radial distance from the high voltage electrode, and the calculated horizontal distance from the spark gap. The number of sparks with this setup was 100.

Attenuator	Thickness [mm]
Very thin	0.45
Thin	1.45
Medium	3.45
Thick	5.95

Table 3.8: Attenuator data for the series of attenuator tests.

Attenuation geometry

The second calibration geometry was also used for attenuation testing. We put different kinds of plastic attenuators over the sensitive parts of the detectors. We did three series: 100, 100, and 50 sparks. The detector locations were the same as for the re-calibration sparks, and is given in Table 3.4.

The order of the detectors was UB1, UB2, UB3, H1, H3, UB4. There were three different attanuators: UB2 was covered by the thin one, UB3 by the medium one, and H1 by the thick attenuator. For the second set of attenuator tests, the locations were kept the same, and an even thinner attenuator was made. UB2 was covered by the very thin attenuator, UB3 by the medium one, and H1 by the thick attenuator. For the second series, the optical fibers of the H1 detector was covered by a plastic tube of 3 mm thickness. This was done to further reduce the chance of any light from the spark getting into the fibers, thus making it even more reasonable to believe any signal came from the scintillating fibers. The attenuator data are given in Table 3.8. The number of sparks for each of these two series were 100.

We also did one series of 50 sparks with the following configuration: UB3 was still covered

by the medium (1.45 mm) attenuator, and was the only detector with an attenuator. The optical fibers of UB2 and H1 were covered by the 3 mm plastic tube, none of the other detector's optical fibers were covered. This was done to investigate whether covering the optical fibers had any impact on the signals. If it did, it would mean that some of the measured signal could stem from the scintillating fibers, and some from the optical fibers. This would mean that we would have to figure out how much of the signal was caused by each of the types of fibers. All positions were the same as for the two previous series of sparks.

3.4 Safety measures

Due to the potential for bodily harm to experimenters working with high-voltage equipment, several safety measures are in place. The Marx generator and the electrodes are in an area enclosed by metal fences. Before the equipment can be operated, certain conditions must be met. There are doors in the fence, and they must be closed and a grounding rod must be placed in front of one of the doors. The doors to the laboratory must be closed. A button must be pressed. If a door is opened, the button is switched off. This ensures that experimenters are aware of anyone entering the laboratory through other doors. Experimenters are required to wear ear protection gear. Before any spark is fired, experimenters yell out a warning.

The sparks generate ozone in the air, which can be a health hazard if the concentration gets to a high enough level. Therefore, spark generation is regularly stopped and laboratory doors opened to ventilate.

We know that laboratory sparks generate x-rays (Dwyer et al., 2005b). There is a possibility that these x-rays could be harmful to experimenters, especially for large amounts of sparks. As far as we know, there has not been any dosimeter tests to determine the actual radiation dose per 100 or 1000 sparks.

Chapter 4

Data

In this chapter we describe the data we collected during the experiments, before we describe data analysis methods in the next chapter. We present the structure of the raw data, and some typical events found in the data. The reader should be aware that the labels on the vertical axis varies from figure to figure, but generally stays constant within one figure. This is done because some detector hits are so strong that if all plots in this thesis were made with those in mind, many weaker detector hits and details in the data would be impossible to see.

4.1 Description of the data

Two of the three oscilloscopes are identical, but all three are quite similar. The notable difference is that one of the oscilloscopes have twice the sampling frequency of the other two. This means one oscilloscope has twice as many data points over the same period of time. Oscilloscope 1 and 2 collect 10,000 data points over 2 μs, while oscilloscope 3 collects 20,000 data points.

For each spark, each oscilloscope saves voltage measurements and the corresponding time measurements. Time measurements are typically in the range $[-0.2\,\mu s, 1.8\,\mu s]$. The zero-point of the times for oscilloscope 1 is when the oscilloscope receives the high-voltage trigger for rising voltage, while the others are zeroed when they receive the trigger from oscilloscope 1. The electrical breakdown occurs around 1.5 μs. Detector hits usually occur in the range $[0.45\,\mu s, 0.85\,\mu s]$. This is know from visual inspection of the data and experience of previous similar experiments.

As discussed in chapter 3, the oscilloscopes do not start at the same time, and the different

channels have different time offsets due to the experiment setup and the components. Therefore, all plots of data in this thesis will be made taking these offsets into account. The offset numbers can be found in Table 3.2.

4.1.1 Housekeeping oscilloscope

Oscilloscpe 1 is called the housekeeping oscilloscope, since it collects data on the hardware: voltage, electrode currents and camera on/off status. The data typically looks like the example shown in Figure 4.1.

4.1.2 Detector oscilloscopes

Oscilloscope 2 collects data from the two LaBr detectors, and from the H1 and H3 fiber detectors. H3 was not used for the first 150 sparks. The data from these oscilloscopes varies a lot more than the data from oscilloscope 1. It's hard to say what "typical data" would look like. One example is given in Figure 4.2, which shows the detector data from oscilloscopes 2 and 3 for the same spark as in Figure 4.1.

4.2 Typical events

In the previous section, we saw some raw data. The data varies from spark to spark, but most of it can be placed in one of the categories of this section. To get an overview of what the data may look like, we will describe typical events measured by the detectors.

4.2.1 Blank (noise)

For some sparks, no detectors are hit by electrons or photons, or the detectors are hit by something so weak that it is indiscernible from the electrical noise of the electronics. The different detectors, photomultiplier tubes, and oscilloscopes seem to have different levels of noise. An example of the noise can be seen in Figure 4.3. The noise and noise reduction is discussed further in section 5.1.

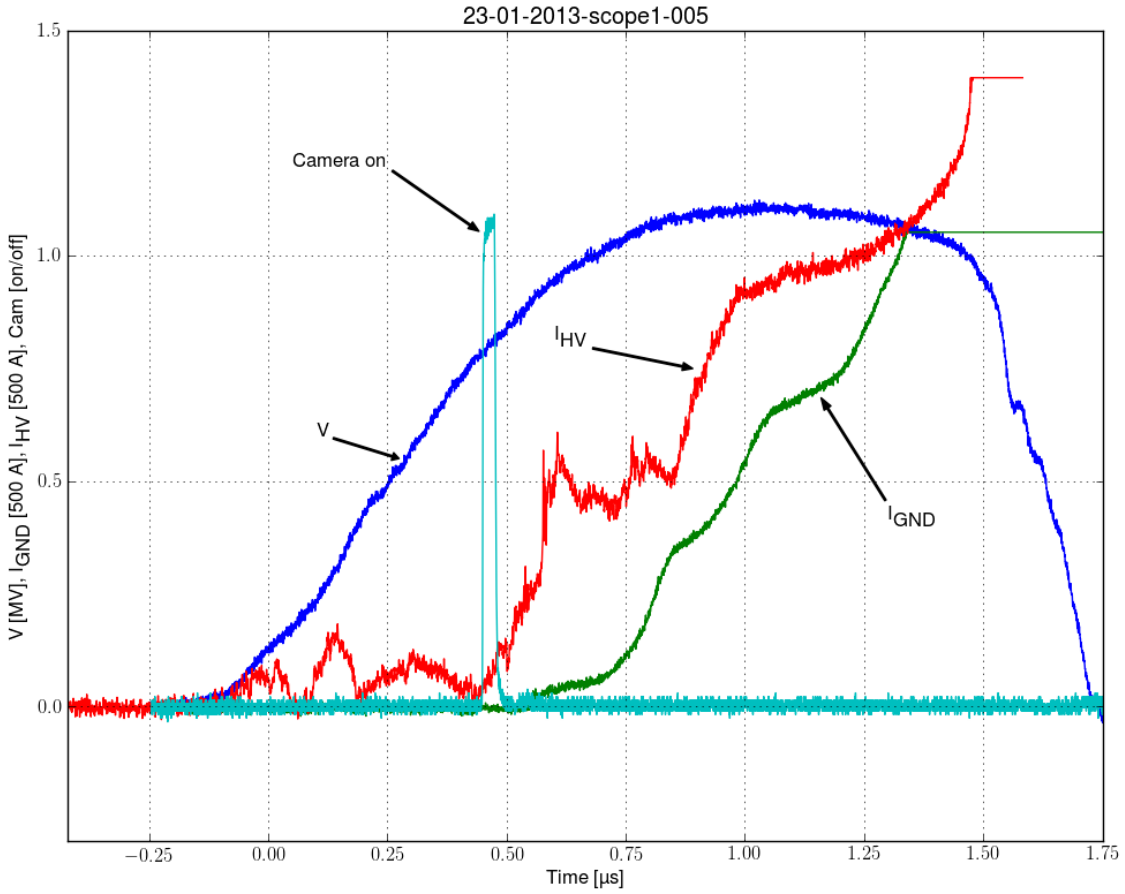

Figure 4.1: (Color) Typical data from oscilloscope 1, the housekeeping oscilloscope. The *blue line* shows the voltage, the *green line* shows the current in the ground electrode, the *red line* shows the current in the high voltage electrode, and the *cyan line* shows when the camera takes a photograph. The two current plots rise to a level where they seem to suddenly stay at a constant level. This is due to the oscilloscope channels becoming saturated. See subsection 4.2.6 for more. The title indicates which spark event the data is from: 23-01-2013 is the date. The number 005 is the fifth spark of the day.

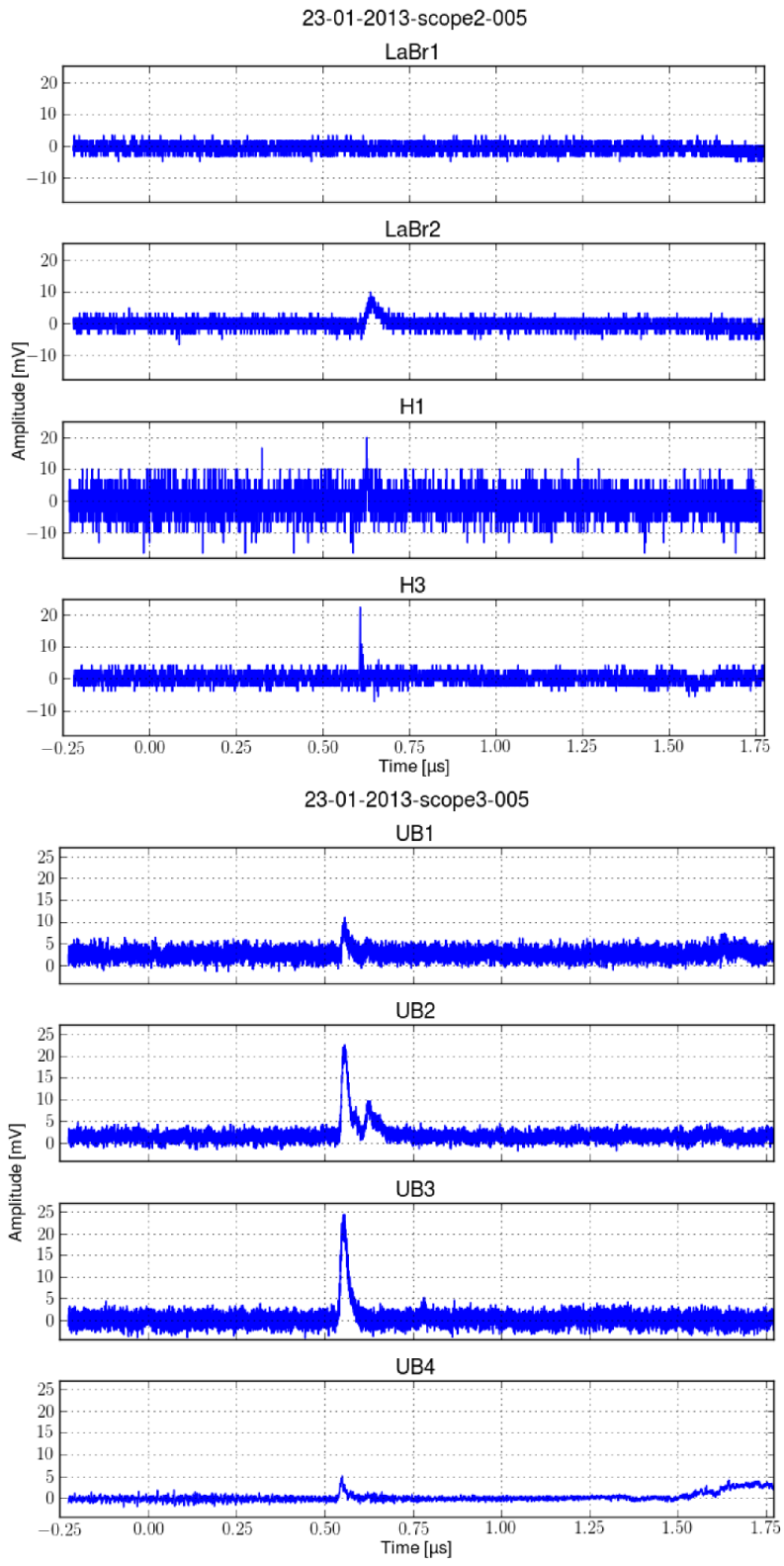

Figure 4.2: Detector data for all eight detectors. For each channel, time is given in µs along the horizontal axis, and amplitude is given in mV along the vertical axis. Data is typically plotted like this to make it easier to read data for each detector. Note that for each oscilloscope, all vertical axes are scaled to the same values. This is done to make it easier to compare the amplitude of a detector hit once calibration is done.

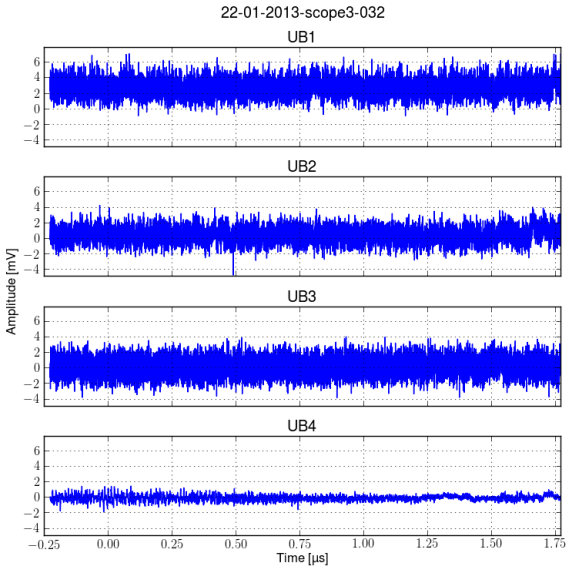

Figure 4.3: This figure shows what the data may look like when nothing happens. It is worth noting that the noise in the different channels has different magnitudes, and that the average values are different. The different averages are caused by the offset setting of the oscilloscope during the experiments.

4.2.2 Detector hit

If a detector is hit by electrons or photons, there will be a signal in the corresponding oscilloscope channel. Detector hits may be easy to notice in the data, as shown in Figure 4.4. Other detector hits can be much more difficult to find because of the noise. We will explain one tool for finding these in subsection 5.1.2.

4.2.3 Weak detector hit

Detectors may experience weak hits (small amounts of energy deposited by electrons and photons). These hits may be difficult to see in the data, as they do not stand out very much from the noise. An example can be seen in Figure 4.5. Weak hits like this one can be easier to find with data analysis methods. This is discussed in chapter 5.

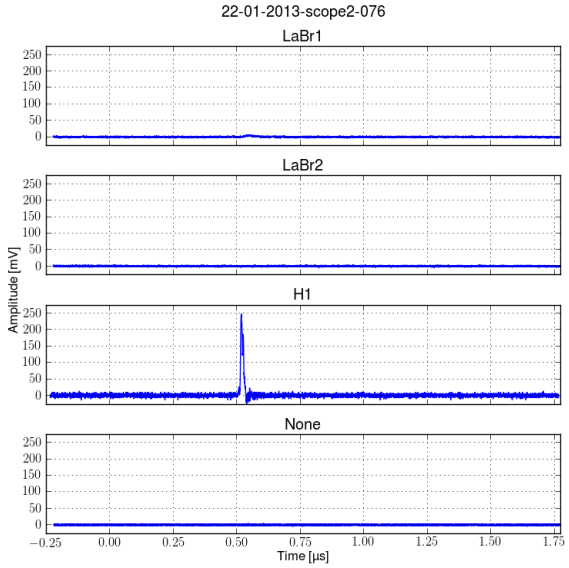

Figure 4.4: This figure shows data when a detector is hit. In the plot of UB1 data, we can clearly see something standing out from the noise around $t = 0.50$ µs. Channel 4 is labelled "None" because the H3 detector was not connected for this spark.

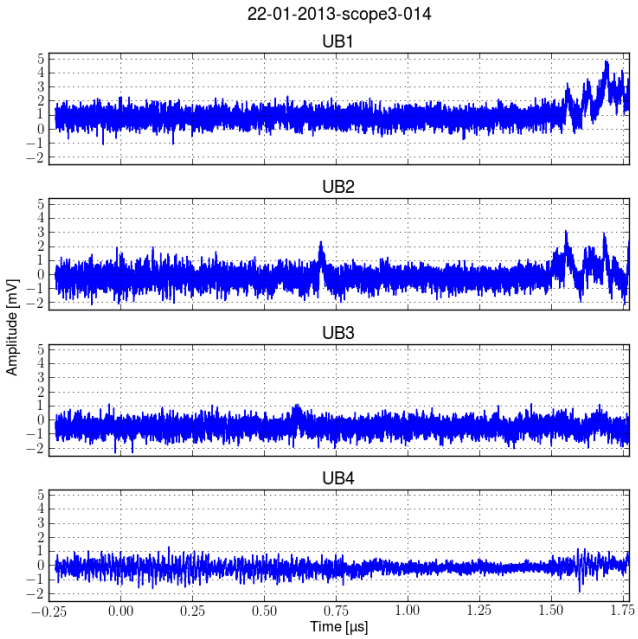

Figure 4.5: The signal from UB2 at $t = 0.70$ µs is weak, and can hardly be discerned from the noise. At the right end of the plot, there is increased noise, which is actually of the same amplitude as the hit earlier. There is also similar noise at the end of the plot of UB1. This kind of noise at the end of a spark event correlates with the discharge of the spark, and is dismissed as light leaks, see subsection 4.2.7.

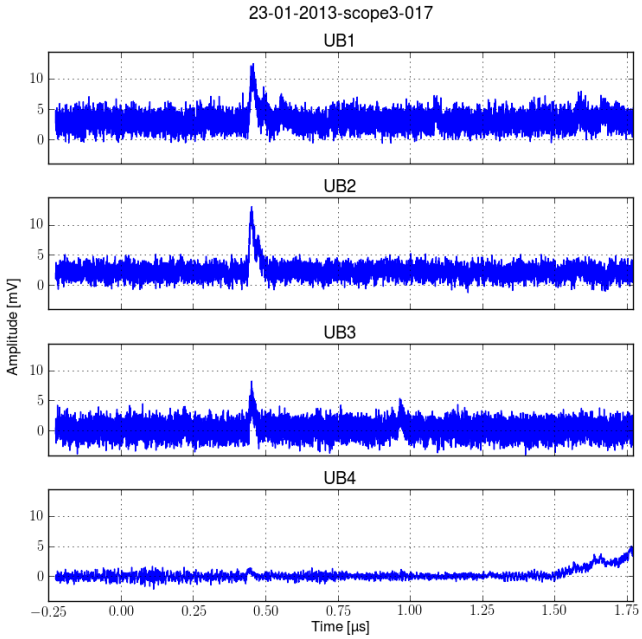

Figure 4.6: At $t = 0.45$ µs, it is clear that at least detectors UB1, UB2, and UB3 are hit. It seems like there might also be a small bump in the signal from UB4 at the same time.

4.2.4 Simultaneous hits

For some sparks, multiple detectors are hit at the same time (or very close in time). Depending on detector setup geometry, this indicates that the detectors are hit by electrons or photons from the same source. We should keep in mind the possibility that simultaneous hits can be caused by different sources. An example of multiple simultaneous hits is given in Figure 4.6.

4.2.5 Double hit

Sometimes, detectors are hit more than once for a single spark. Of course, any peak in the plots might be the sum of two hits (counting a hit as one or more electrons or photons depositing energy). When the plots look like what is shown in Figure 4.7, it is obvious that a detector was hit (at least) twice.

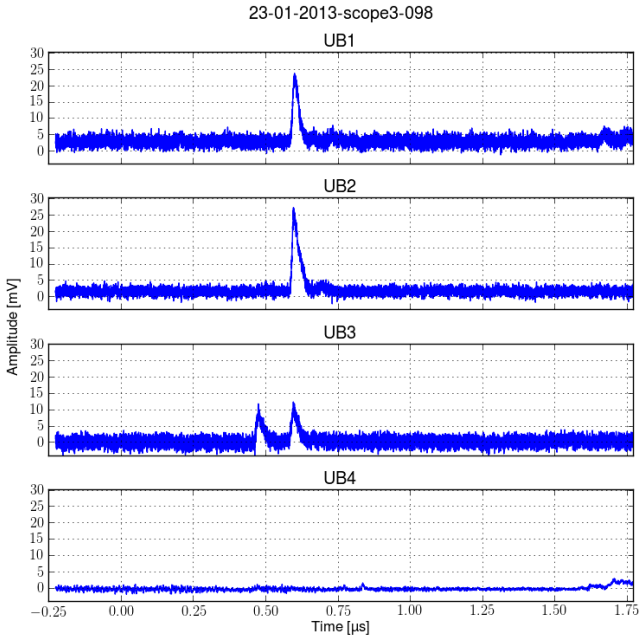

Figure 4.7: At $t = 0.45$ µs and at $t = 0.60$ µs, UB3 is hit. It is clear that the two hits are separate, and that one of them is correlated in time with hits in UB1 and UB2.

4.2.6 Saturation

The oscilloscope channels may be saturated by strong signals. This depends on the sensitivity selected for each channel. High resolution of the data is desirable, but this requires a more narrow voltage range. This led to some channels being saturated for some sparks, when the detectors were hit by more energetic or just a larger amount of electrons and/or photons. An example of saturated channels is shown in Figure 4.8. There is a cut-off and a horizontal line where the peak should be. The cut-off in this figure occurs at around 400 mV for LaBr1 and LaBr2, and at 700 mV for H1. The maximum value would be even larger if we could have captured the entire signal. Comparing this to the peak values of Figure 4.7 of 25 mV, we see that saturation covers up very energetic events.

Due to the way we used offsets and scaling during the experiments, some channels will saturate at different voltages than other channels for some or for all sparks.

When the oscilloscopes are saturated, we frequently observe signals that look like ripples in water, or the after-quakes of earthquakes. This effect is deemed likely to be caused by the electronics, as there is no reason to believe that electrons and photons are emitted for a much

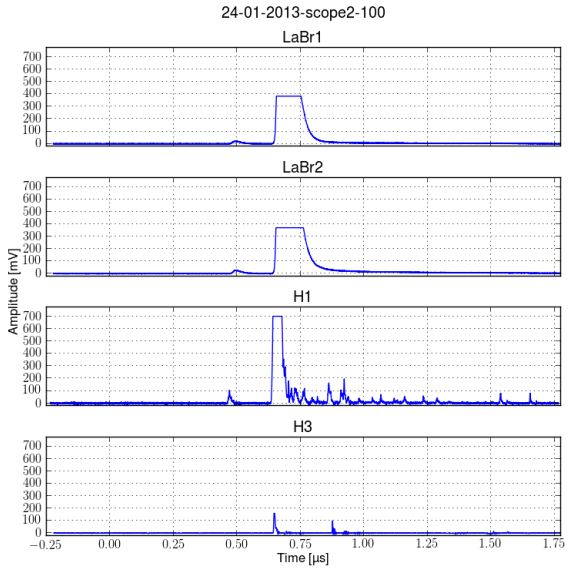

Figure 4.8: When detectors are hit by highly energetic electrons or photons, or hit by a large amount of electrons or photons, the oscilloscope can be saturated. This results in a cut-off, and the peak is not measured. Comparing this to the shape of peaks that are not saturated, we see that the saturated signals cover up extremely energetic events.

longer and different period of time for some sparks. These ripples can be quite big. The biggest peaks of the ripples in Figure 4.8 are on the scale of 200 mV, while the hit peaks of some events can be around 25 mV. This poses a problem when trying to find the peaks that corresponds to detector hits, and will be further discussed in chapter 5.

4.2.7 Light leaks

For some sparks we found large signals towards the end of the plots. An example of these signals is shown in Figure 4.9. The timing correlates well with the actual spark discharge. It is worth noting that the light leaks occurs mostly in series of sparks. Since it is consistent in timing and shape, and usually occurs for every spark in a series, it is very unlikely to be the regular electron or photon hits.

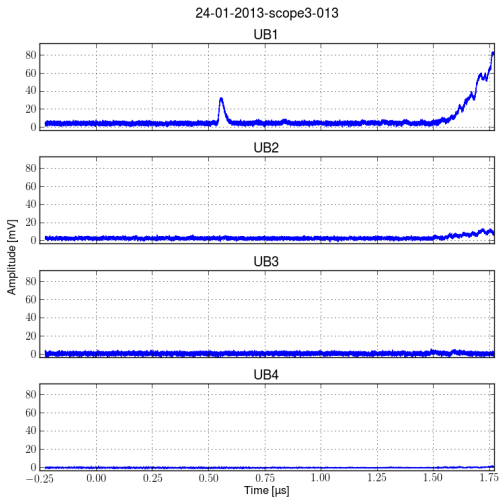

Figure 4.9: The signal in UB1 rises drastically towards the end of the time window. It rises to around 80 mV, which is twice as big as the hit at $t = 0.55$ µs. While not as dominant, the signal in UB2 rises to close to 15 mV towards the end, which is a value that could be found at regular hit peaks. The shape of these light leaks is very different from the shape of regular hits. Regular hits typically rise sharply, almost vertically, then fall off exponentially. The shape of the light leak signals in this case is slower rise, with several small peaks and valleys.

4.3 Discarded data

For some sparks, some channels record very unusual data, that are entirely different from almost all other data. Three examples are shown in Figure 4.10, Figure 4.11, and Figure 4.12. We do not know what caused these measurements. It could be some malfunction of the electrical equipment or corrupted data, it could be particle showers from extremely energetic cosmic rays. Since these are so very different from the rest of the data, it seems unlikely that they are caused by the same physical mechanism. Also, since they are so different, the same analytic methods would not apply to them. These and other extreme data are not used in the actual data analysis.

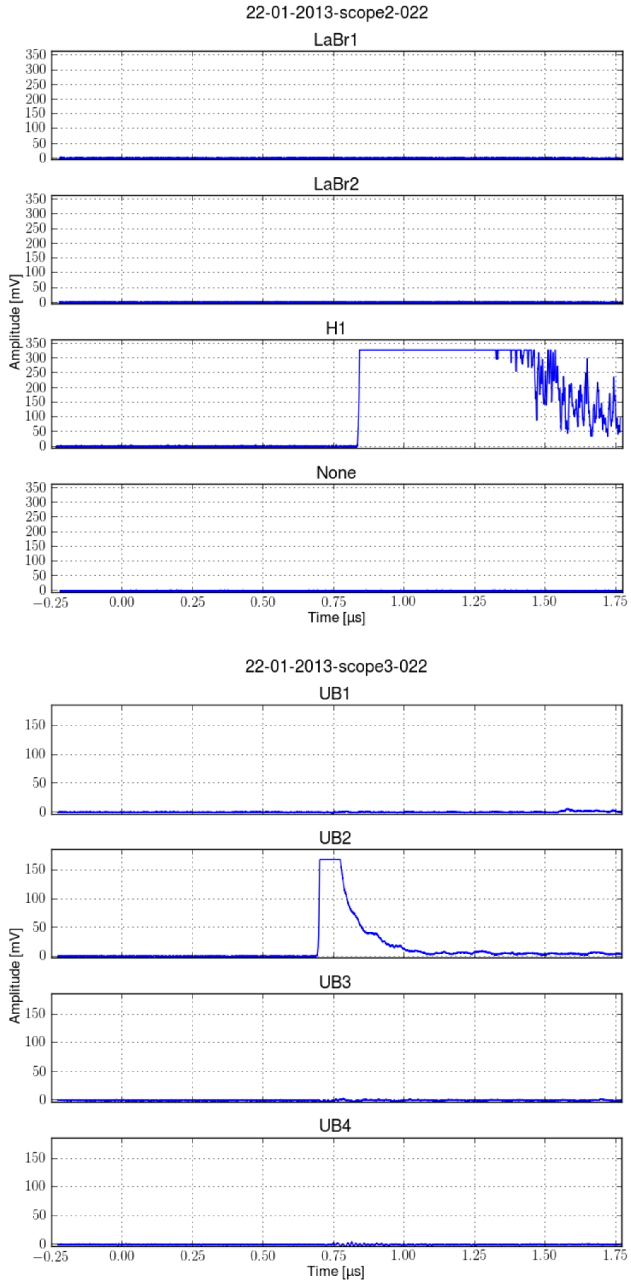

Figure 4.10: The data for this spark is particularly confusing. Detectors H1 and UB2 er both saturated at great levels, but not at the same time for this to be caused by the same source. In addition, none of the other detectors are hit, and this is one of the calibration sparks. This means that one detector at the end and one detector in between the other detectors measure enormous signals while nothing hits the other detectors. No single particle should be able to saturate detectors like this (they would pass through before depositing enough energy), and particle showers would hit the other detectors.

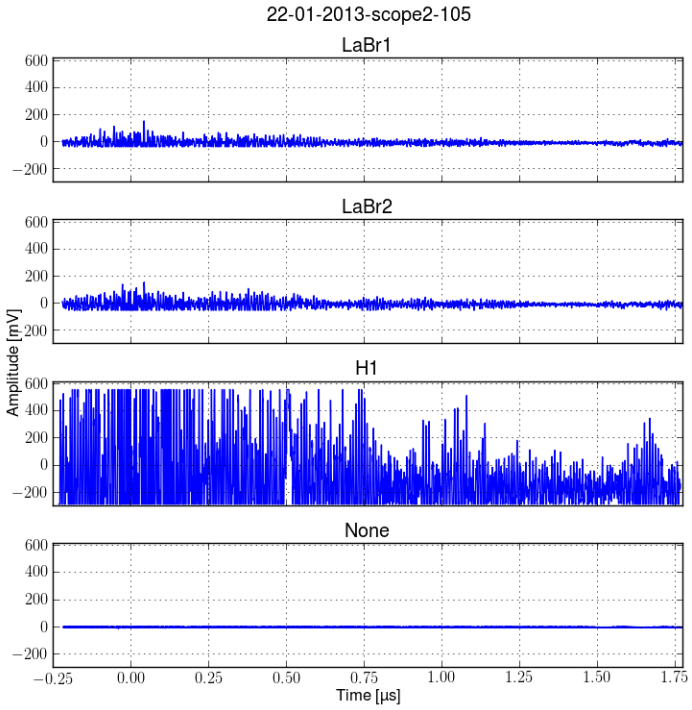

Figure 4.11: The signal in H1 for this spark is saturated many times by very thin peaks, that seem to be falling off in amplitudes. This could possibly be the ripples that usually follow saturations, but if it is, it would have to be saturation from something hitting the detector well before the voltage charge-up over the spark gap. There is a range of points just after $t = 0.50$ µs that could be a typical peak on top of the strange data. It is also entirely unusual to see data like this in the LaBr detectors. There are several very high very thin peaks before the time we usually see peaks from the spark, and much lower values after this.

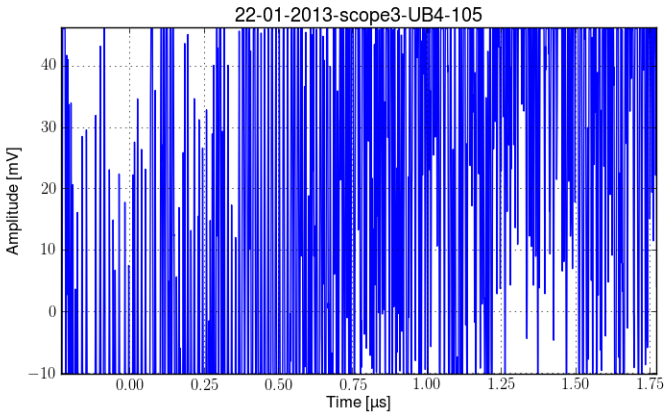

Figure 4.12: The signal from UB4 is varying wildly between positive and negative saturation.

Chapter 5

Data processing

In the previous chapter we explained what the data can look like. Here we will explore some ways of processing the data, before we perform the actual data analysis in the next chapter. The goals of the data processing are to find the peak magnitudes combined with the peak timings, and to estimate the relative sensitivities of the fiber detectors. If the signals were free of any electrical noise, even the simplest algorithms could find the peaks. In reality, there are complicating factors.

We will discuss the noise in the signals, saturation of the channels, "false" hits like the light leaks or the ripples after saturation, and different criteria for automatically finding peaks. Finally, we will discuss different methods of performing the relative calibrations of the fiber detectors. These calibrations will let us compare the signals from different detectors for different geometrical setups and enables us to perform a quantitative analysis of the data. To obtain calibrations of high quality, we first have to address some issues as mentioned above.

5.1 Noise

We will use the word noise about anything in the signal that is not caused by the electrons or photons of interest. Most notable is the continous variation of the signals, as seen in Figure 4.3. If this noise was not present, we could use the basic numerical derivative to find rising edges, falling edges, and peaks. This method does not work as intended if used on the raw data, since the values rise and fall randomly from point to point, and not all changes in the sign of the

derivative indicates a peak from the detectors being hit. This issue can be solved by reducing, or ideally even eliminating the noise, or by designing a different algorithm for identifying peaks. We will do both, starting with noise reduction, after we take a closer look at the noise.

5.1.1 Description of the noise

We will begin by describing some characteristics of the noise. These will be used to find peaks later. The basic idea is to look for data that deviates significantly from the noise. We will define the mean and the standard deviation of the noise first.

If we calculate the mean value for one channel for the entire plot, we get something like the solid red line shown in Figure 5.1. In the same figure, we can also see the values for 1, 3, and 5 standard deviations over the average. These lines show that it would be difficult to set a threshold to say something like "All data more than x standard deviations from the average is a peak." The problem in this case is that the light leak at the end creates a signal magnitude more than twice as strong as the peak, and the width of the light leak peak is quite large. For other plots, similar issues arise from different causes. When channels are saturated, or when peaks are wide, the averages and standard deviations are skewed.

Figure 5.2 shows the same data, with one major difference: The average value and the standard deviation is calculated only from the first 20 % of the data. The data file covers 2 µs, so 20 % is 0.4 µs. The data starts at -0.2 µs, and peaks do not appear as early as 0.2 µs. Therefore, this method calculates the average and the standard deviations based on the noise. This reduces the average value, and greatly reduces the standard deviation. The three dashed lines show 1, 3, and 5 deviations from the average. It is clear that the peak is easily identified by a criteria of the form "x standard deviations from the average". We will use the averages and standard deviations of the noise for later algorithms, and these are always calculated from the first 20 % of the data points. The symbol σ will be used for the standard deviation of the noise as defined here, unless otherwise noted.

The number 20 % is chosen because it is large enough to give reasonably trustworthy measurements of the noise, while not being so large that it includes actual peaks that would skew the measurements of the noise. For simplicity we assume the noise has a normal distribution with standard deviation σ. For oscilloscope 3, we expect around 3,200 points to be over 1 σ, 27

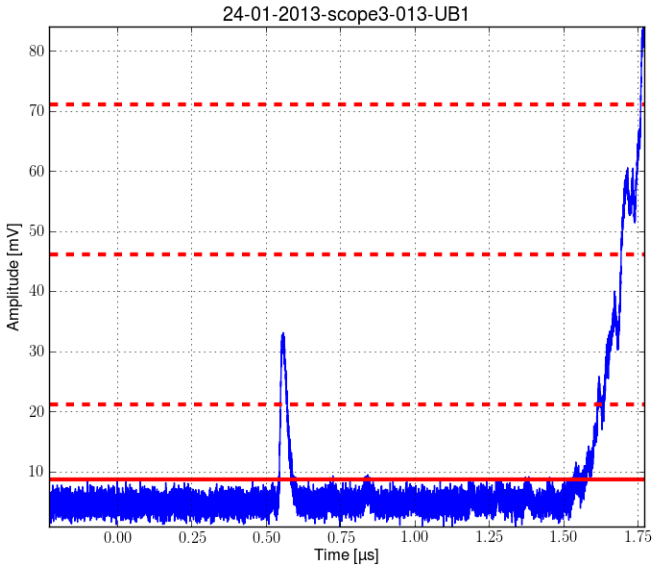

Figure 5.1: (Color) A plot of the data for one channel for one spark *in blue*. The average value for the entire plot is shown by the *solid red line*. The three *dashed red lines* show the values of the average plus 1, 3, and 5 standard deviations, where the standard deviation is calculated from the entire plot.

points over 3 σ, and 0 points over 5 σ. The numbers for oscilloscope 2 are half of these.

Figure 4.8 shows the "aftershocks" or "ripples" in the data after a channel has been saturated, in channels 1-3. These ripples have magnitudes much larger than the noise on the left side of the peaks. These ripples are also part of the noise of the signal in the sense that we do not want to detect these when running peak detection algorithms.

As can be seen in Figure 4.6, the data of some channels (channel 1 in this case) are not centered around 0. The absolute voltage value of a peak magnitude is not important, while the deviation from the background or noise level is important. Therefore, data will be offset equal to the average of the noise in each channel. This is done simply to make sure data in all channels are centred around 0, so visual inspection of plots is simplified.

Because of the light leaks discussed in subsection 4.2.7 and the fact that peaks are almost always found before 1 µs, we will use a cut-off at 1.2 µs when performing automated searches for peaks.

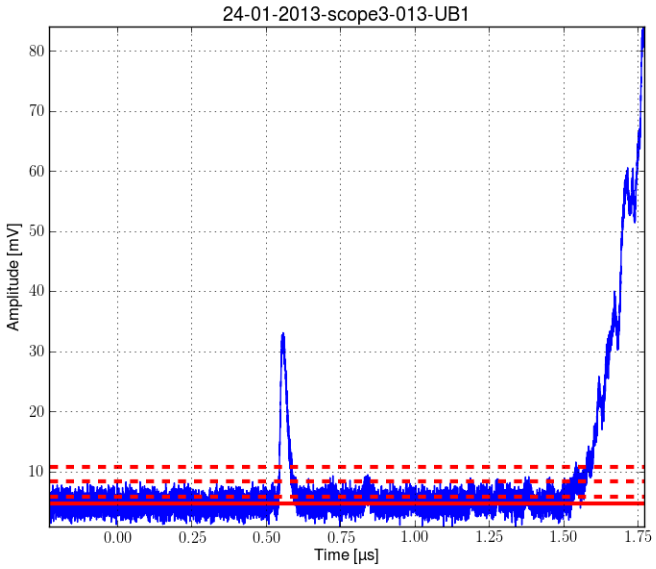

Figure 5.2: (Color) A plot of the same data as in Figure 5.1 *in blue*. The average value for the first 20 % of the data is shown by the *solid red line*. The three *dashed red lines* show the values of the average plus 1, 3, and 5 standard deviations, where the standard deviation is calculated from the first 20 % of the data points.

5.1.2 Smoothing of noise

One way to detect peaks is to look for data points that are much higher than the average value of the noise. One one way to define this is to use a certain number of the standard deviation of the noise. Different thresholds will yield different results. Using a high threshold, we do not catch all peaks. Using a low threshold, we get several false positives, because of the variation in the noise. There is no threshold that will let us detect all peaks and get no false positives. To reduce the amount of false positives from the noise, we introduce the following method to smooth the noise.

The noise is assumed to be random around a constant value, so it should average out to this constant value. The smoothing method is simply to find the average of a data point and its nearest neighbours, for each data point. The method is symmetric as long as it is possible, taking the same number of points on each side of each data point. This does not work for the beginning and the end of the data file, since there are not any more points on the outside. This is circumvented by using as many as possible on the outside, and using the specified number of points in the inside. The smoothing is used to find the time of a peak maximum, but the actual

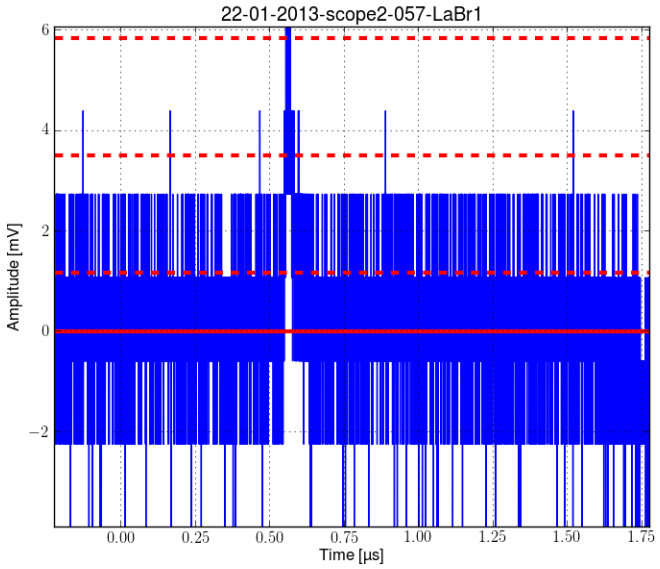

Figure 5.3: (Color) A plot of the data from one channel, including a *solid red line* indicating the average value of the noise, and three *dashed red lines* that show the values of the average plus 1, 3, and 5 standard deviations of the noise. Both the average and the standard deviation is calculated from the first 20 % of the data points.

value for the peak is taken from the raw data, to reduce the impact of averaging the values.

Figure 5.3 shows raw data with lines for average value, and 1, 3, and 5 standard deviations over the average. These values are computed from the first 20 % of the data points, as discussed in the previous subsection. The peak value around $t = 55$ µs is close to 5 standard deviations over the average. It is the only value this high, and could thus be found by an algorithm searching for values over 5 standard deviations over the average.

In the next two figures (Figure 5.4 and Figure 5.5), the smoothing method is applied, using two different smoothing window widths. This reduces peak magnitude, but also noise and noise standard deviation magnitudes. The peak magnitudes are around 8 and 17 of the noise's standard deviations over the average value of the noise. These peaks can be found with algorithms with much stricter criteria, while finding false positives from the noise is even less likely. The smoothing window widths of 3 and 21 data points are quite narrow compared to the full length of a data file of 10,000 or 20,000 data points over 2 µs.

In other cases, much wider smoothing windows might be necessary to see very weak hits. Figure 5.6 shows raw data for a certain detector for a certain spark. Around $t = 0.45$ µs, we see a

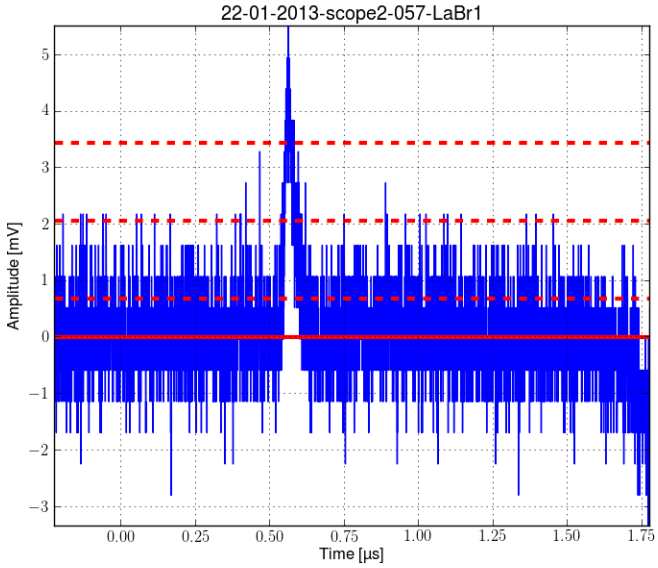

Figure 5.4: (Color) A plot of smoothed data from the data used in Figure 5.3. The smoothing is done as described in this subsection, with a smoothing window width of 3 data points. Every value plotted here is the average of itself and one point on each side of it in the raw data. This reduces the maximum value of the peak, but also reduces the magnitude of the noise, and the value of the standard deviation.

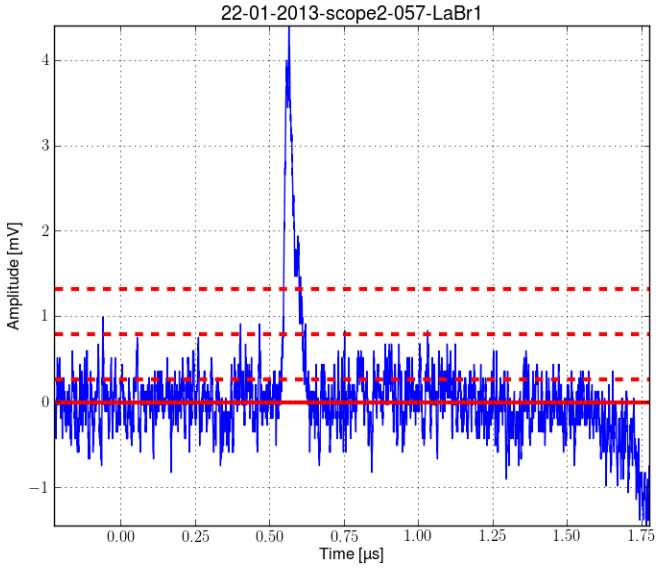

Figure 5.5: (Color) A plot of smoothed data from the data used in Figure 5.3. The plot is made in the same way as in Figure 5.4, but this time with a smoothing window width of 21 data points. Every value plotted here is the average of itself and ten points on each side of it in the raw data. This further reduces the maximum value of the peak, but also reduces the magnitude of the noise, and the value of the standard deviation.

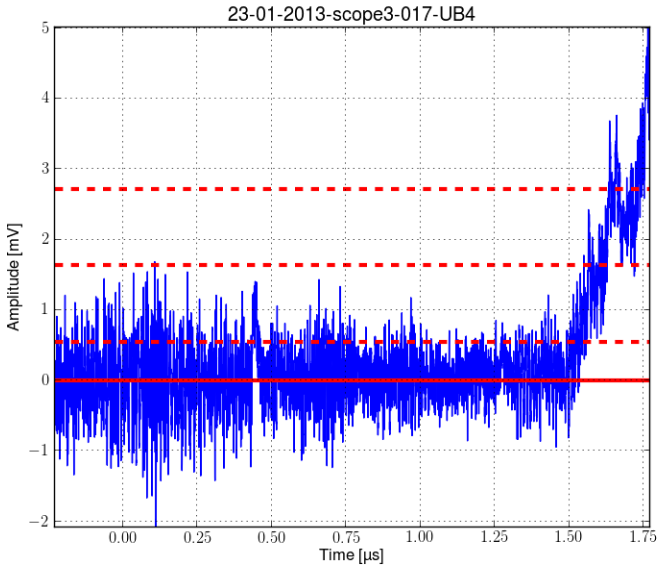

Figure 5.6: (Color) A plot of raw data from UB4, which typically shows the lowest magnitude peaks. Around t = 0.45 µs, there is an interval where all values are over the noise average. The *red lines* are defined as for the previous figures.

range of data points where all the values are over the average of the noise. The data is smoothed with a window width of 21 and plotted in Figure 5.7. This is the same window width as the one that made the peak in Figure 5.5 greatly stand out from the noise, but in this case it hardly makes a difference. Expanding the smoothing window to 51 data points decreases the amplitude and the standard deviation of the noise, and the peak value stands out enough from the noise to be identified by an automated algorithm. This is shown in Figure 5.8.

Of course, one might question whether this is a real hit or not. We argue that it is, since it is happening within the regular time interval for hits, and peaks like this do not show up in the noise in the first 0.5 µs of any of the data files. The peak can even be seen in the raw data in the first of these figures, where there seems to be a lack of low values for a short time interval. This is exactly what a hit looks like.

Since it is obvious that the maximum values of peaks are reduced by smoothing, the idea is to use smoothing to locate peaks, and to find maximum peak values close to where the smoothed data has a peak. This is further explained and tested in section 5.2.

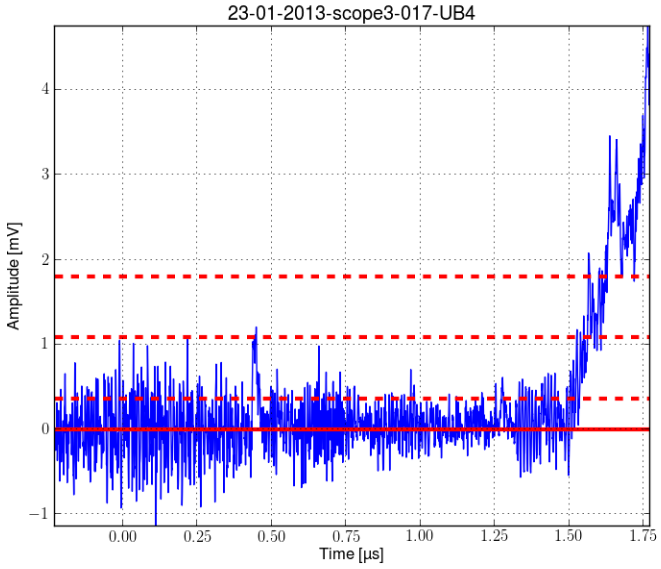

Figure 5.7: (Color) The same data as in Figure 5.6, smoothed with a smoothing window width of 21. The peak at t = 0.45 µs stands out more, but is still no greater than the amplitude of the noise, at 3 times the standard deviation of the noise. The *red lines* are defined as for the previous figures.

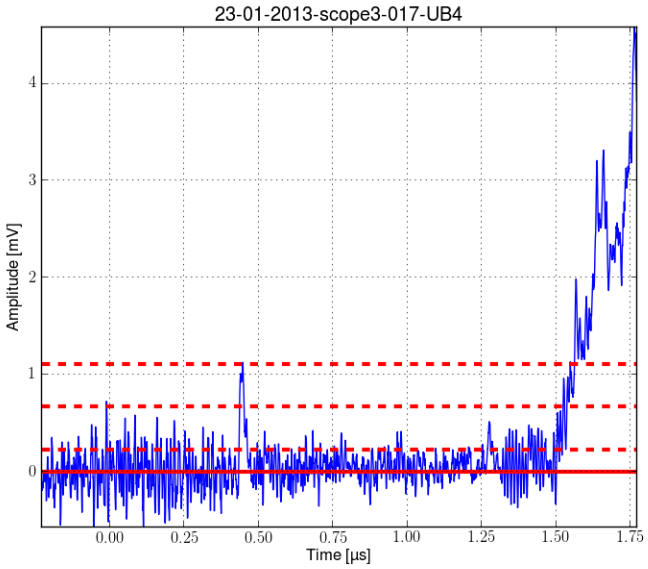

Figure 5.8: (Color) The same data as in Figure 5.6, smoothed with a smoothing window width of 51. The amplitude of the peak at t = 0.45 µs is now at 5 standard deviations of the noise, and it stands out clearly from the noise. The *red lines* are defined as for the previous figures.

5.2 Error by smoothing

As we showed in the previous section, the smoothing algorithm makes it easier to find peaks. It also reduces the magnitude of the peak, and the maximum value after smoothing can be shifted along the time axis, depending on how the data reacts to the smoothing in each case. These issues are discussed in this section.

5.2.1 Amplitude attenuation due to smoothing

When we use the smoothing routine described above, peak amplitudes will be reduced. Therefore, smoothing is used to find the timing of peaks, and actual peak amplitudes are found by checking the raw data at the time of the peak in the smoothed data. The smoothed data can have peaks at different times than the raw data. Therefore, the value found in raw data at the time of a peak in the averaged data can be lower than the actual maximum value in the raw data. It is of interest to know the magnitude of the reductions of the values. For some sparks, some channels registers more than one hit. To simplify the test of the smoothing, we will just use the maximum values from each data file.

We found the maximum values for each data file for the raw data, and the times of the maximums in the smoothed data, for smoothing window widths of 5 and 51 data points. The raw data values at these times are compared to the raw data maximum values in Figure 5.9. In this figure, we see that the points are mostly gathered in upper right corner of the plot. The most interesting aspect of the plot is that several points indicate that the attenuation is negative. This is caused by data files with no peaks (just noise), where the maximum in the smoothed data occurs at a time where the corresponding data point in the raw data is negative. This happens mostly for 51 width smoothing. Figure 5.10 is made by selecting only data files where at least one point is at least 5 σ over the average. The figure shows that for 51 width smoothing, some points still indicate negative attenuations. These are caused in the same way as the negative attenuation points in the previous figure.

Figure 5.11 shows the attenuations due to smoothing when only considering data files with peaks over 35 σ. For 5 width smoothing, all peaks will be at 90 % or more of raw data peak values. For 51 width smoothing, some points indicate great attenuations. We explored some of

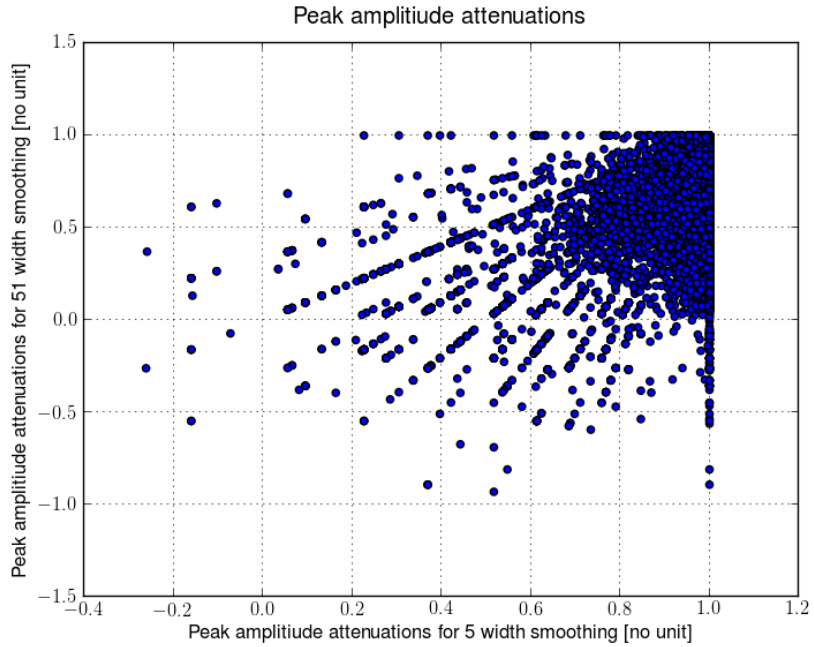

Figure 5.9: The peak value attenuations due to smoothing for all data files, for smoothing window widths of 5 and 51 points. Each point corresponds to data for one channel for one spark. The horizontal coordinate of the point indicates the attenuation of the maximum value when the data is smoothed with a 5 width smoothing window. The vertical coordinate indicates the same for a 51 width smoothing window.

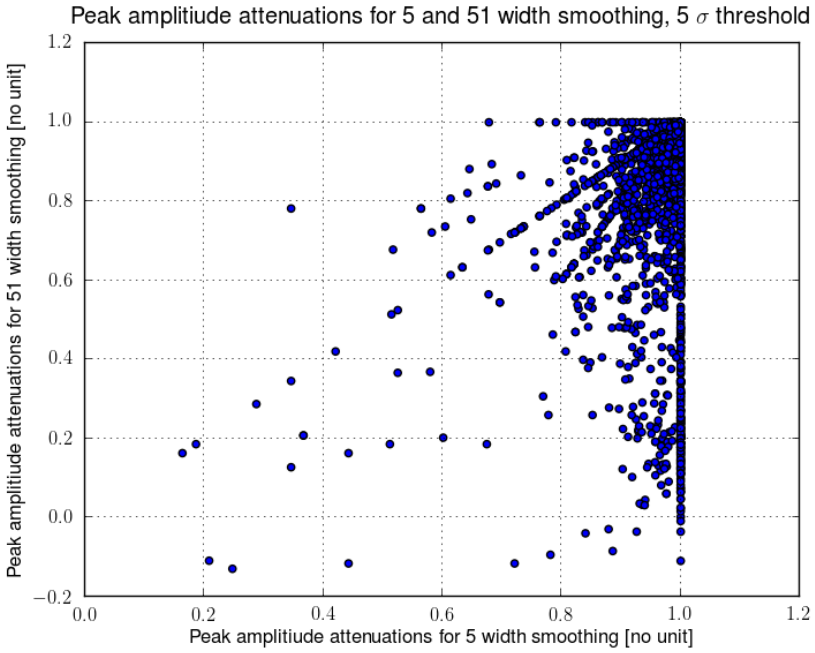

Figure 5.10: The peak value attenuations due to smoothing for all data files, for smoothing window widths of 5 and 51 points, for peaks over 5σ amplitudes.

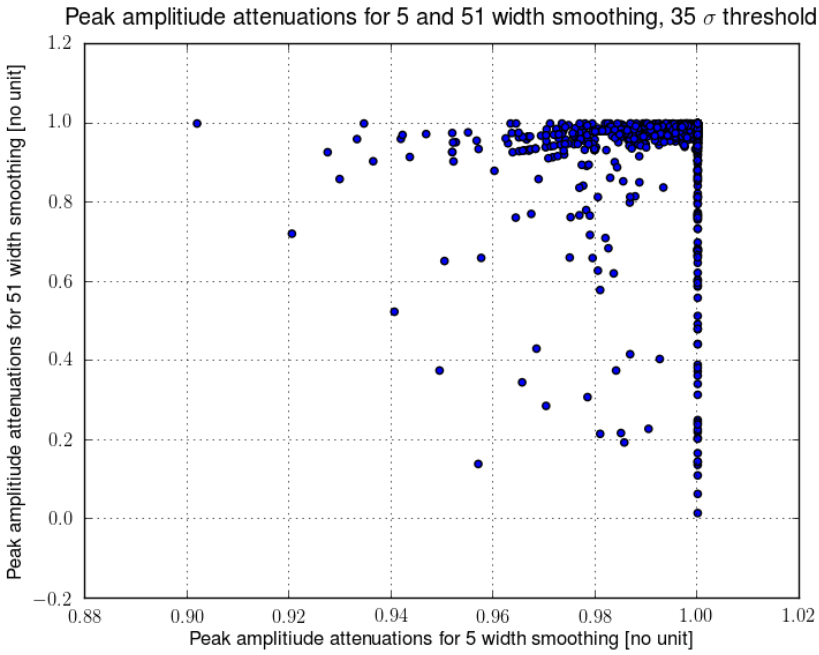

Figure 5.11: The peak value attenuations due to smoothing for all data files, for smoothing window widths of 5 and 51 points, for peaks over 35σ amplitudes.

these points, and found that these are caused by extremely thin peaks. One example of this is shown in Figure 5.12 and Figure 5.13. The maximum value in the smoothed data is slightly to the right of the maximum value in the raw data. Since the raw data is of a much lower magnitude at this point, the calculated attenuation is great.

5.2.2 Time offsets due to smoothing

Some of the issues with smoothing are caused by the time offsets of the maximum values. To examine the time shifts due to smoothing, we plotted the time shifts for smoothing window widths of 5 and 51 against each other, as seen in Figure 5.14. Since this is done for all data files, there are 7600 points in this figure. Many of the points represent time offsets for data files with no peaks from detector hits (just noise). When there is no hit peak, smoothing may remove a very thin noise peak while not entirely removing another noise peak, which can be anywhere in the data file (except for after 1.2 µs, which is excluded). Therefore, these data files are very susceptible for large time offsets.

To get a better picture of how the smoothing shifts the time of maximum values, we exam-

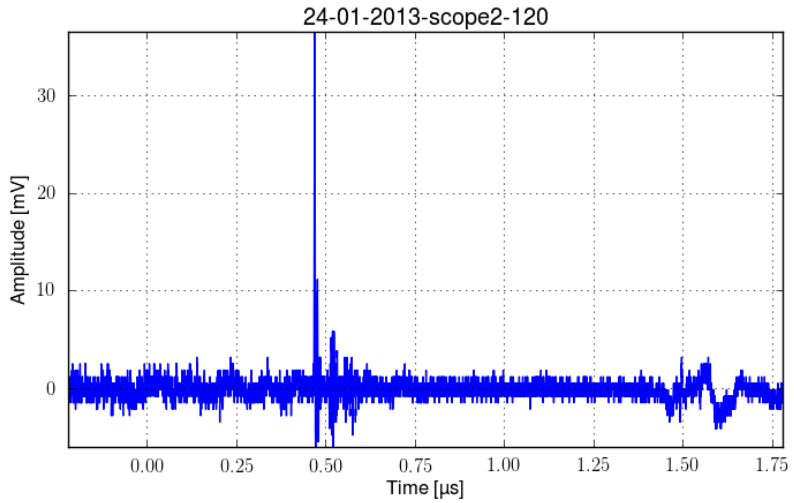

Figure 5.12: Plot of the data for a data file with an extremely thin peak.

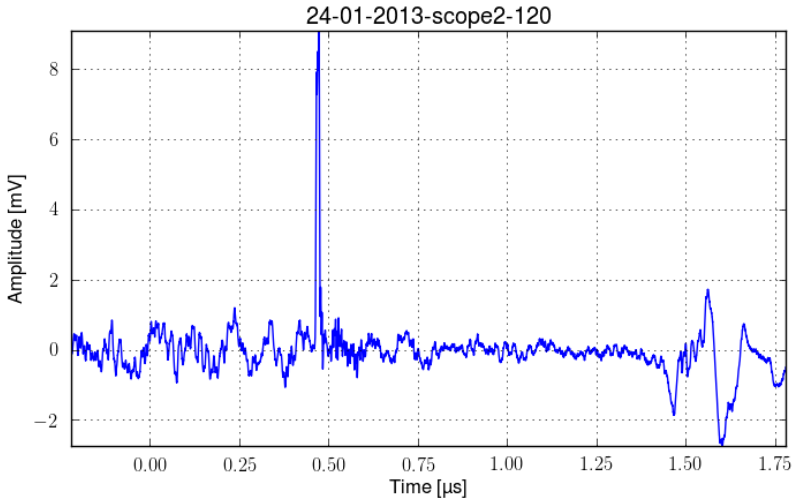

Figure 5.13: Plot of the same data as in Figure 5.12, smoothed with a smoothing width of 51 data points. Note that the maximum value is much lower after smoothing.

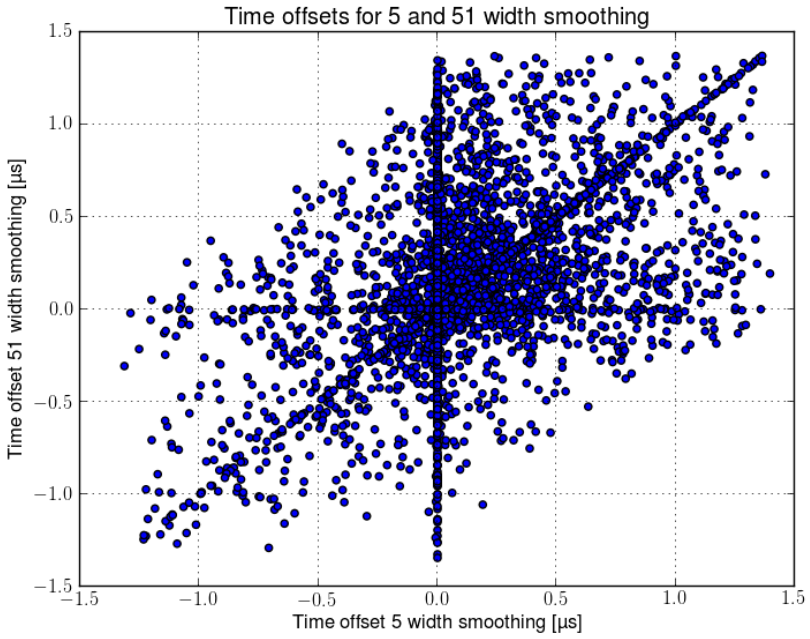

Figure 5.14: The time offsets of the maximum values due to smoothing, for all 8 detector channels, for all 950 sparks, for smoothing window widths of 5 and 51 points. Each point represents one data file. The horizontal coordinate indicates the time offset of where the maximum value is before and after smoothing with a 5 width smoothing window. The vertical coordinate indicates the same for a 51 width smoothing window.

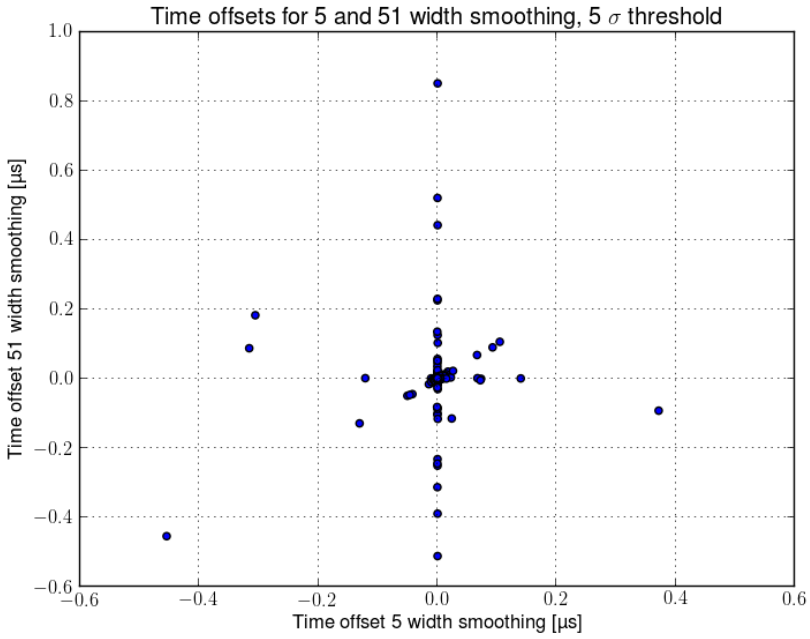

Figure 5.15: The time offsets of the maximum values due to smoothing, for any data file where the maximum is more than 5σ over the average value of the noise.

ined two selections of the data files. The first selection was done based on the criterion that the maximum value of the data file was more than 5 σ over the average. This selection includes 2624 of the 7600 files. The second selection consisted of files where the maximum was more than 35 σ over the average. This selection includes 1110 of the 7600 files.

The time offsets for the first selection are shown in Figure 5.15. When comparing this to Figure 5.14, it is important to note that the range of the axes is narrower, and that only around 12 points are far from the center, which means that the variations are much smaller for this set of data. If 12 points are far from the center, there are an overwhelming 2612 points close to the center (low offsets for both smoothing window widths).

Since a maximum value of five times the standard deviation of the (unsmoothed) noise, 5σ, is a very small peak, we also examined how the smoothing affects larger peaks. Figure 5.16 shows the time offsets for the second selection of data (maximums over 35 σ). The figure has even more narrow ranges for the axes. Only around 10 of the points in the figure are not in the central cluster. That leaves 1100 points in the central cluster. This means that for the vast majority of cases, the time offsets for large peaks is almost negligible.

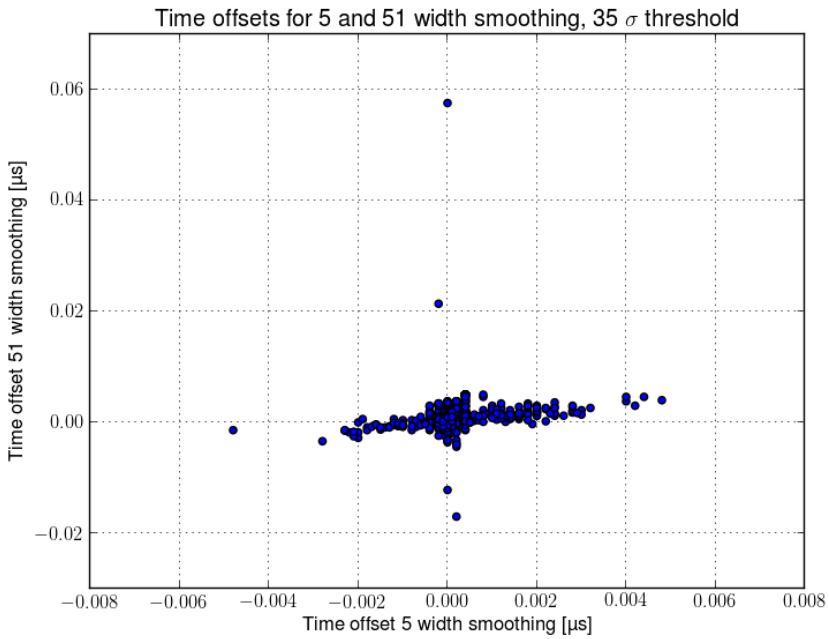

Figure 5.16: The time offsets of the maximum values due to smoothing, for any data file where the maximum is more than 35 σ over the average value of the noise.

	Smoothing width 5		Smoothing width 51	
Peak amplitude	0.5 percentile	99.5 percentile	0.5 percentile	99.5 percentile
5 σ	-0.094 µs	+0.0166 µs	-0.087 µs	+0.0576 µs
35 σ	-0.0021 µs	+0.0032 µs	-0.0036 µs	+0.005 µs

Table 5.1: The table shows the limits for a range of values that contain 99 % of the points for Figure 5.15 and Figure 5.16, for the two peak amplitude thresholds of 5 and 35 σ.

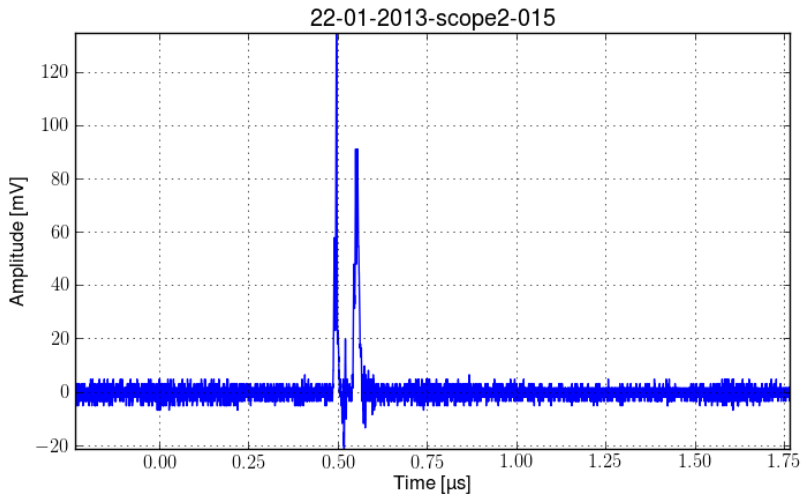

Figure 5.17: The raw data for the outlier at the top of the plot of Figure 5.16. The first peak is the tallest.

The ranges that contain most of the data points for the peak time offsets can be found in Table 5.1. The ranges are narrow, especially for larger peak amplitudes. The main reason that the smoothing width of 51 has a wider range than the smoothing width of 5 is that very thin peaks are more heavily affected by the wider smoothing width.

We have examined all outliers for both Figure 5.15 and Figure 5.16, and they fall into one of three categories. One category consists of data with two peaks, where the smoothing reduces the maximum values so that the tallest becomes lower than the other smoothed peak. This is illustrated by Figure 5.17 and Figure 5.18. The other category consists of data with noise, where there is just one or a few data points with high values, that simply disappear during the smoothing, illustrated by Figure 5.19. The greatest time offsets fall into this category. The third category contains offsets caused by slight saturation, where some consecutive data points have the same value. The method used to find maximum values will use the first occurrence of the value. After the smoothing, the point which was previously the first of the points of the same value will be lower than at least some of the others, since it is averaged with more low values from the rising edge.

All in all, the time offsets for large peaks are negligible with very few exceptions. Time offsets for smaller peaks may be a slightly bigger problem, which is easily solved by visual inspection of the plots.

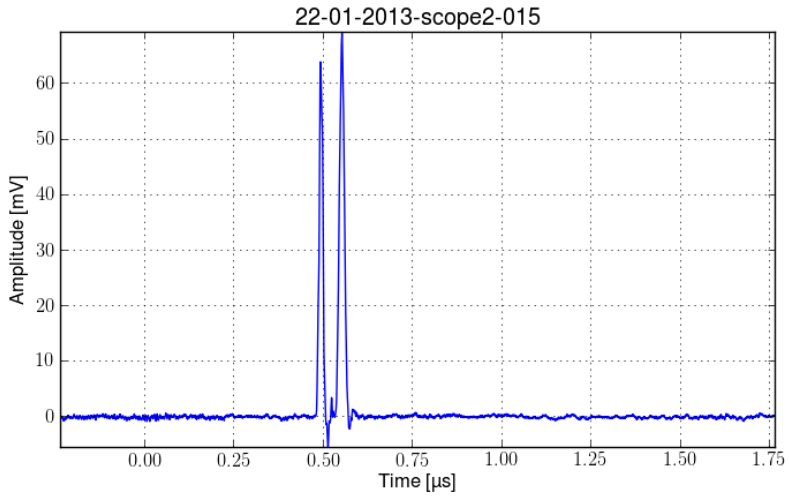

Figure 5.18: The data from the same detector and spark as Figure 5.17, smoothed with a smoothing window width of 51 data points. The second peak is now the tallest.

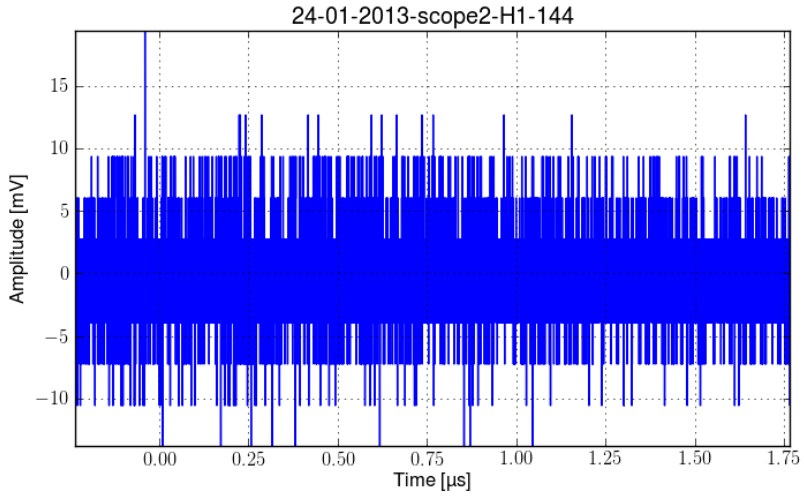

Figure 5.19: The raw data for the outlier at the top of the plot of Figure 5.16. There is a very thin peak (one or just a few data points) with a value higher than the rest of the noise around $t = -0.05\,\mu s$.

The reader is advised to keep in mind that the analysis of the smoothing is done using just the simplest method; looking for the maximum value. More sophisticated methods combined with visual inspection will provide less of a time offset, and thus less peak value attenuation.

5.3 Saturation

As shown in subsection 4.2.6, some peaks saturated oscilloscope channels. The events where one or more channels are saturated are the most energetic events, and in some respects the most interesting events. Unfortunately, it's hard to analyze them when we just do not have the data. Of course, one could try to estimate the actual peak value for saturated channels.

To estimate peak values, we would need to decide on a typical shape for peaks. As can be seen in several figures in chapter 4, peaks seem to have different shapes. Some seem to be symmetric Gaussian curves, while the larger peaks are not typically shaped like Gaussian curves. The larger peaks (including saturated peaks) seem to be shaped like an almost vertical rising edge, and falling off as a decaying exponential.

We have tried to determine a starting point, the peak point, and an end point, and use these to estimate a Gaussian shape curve to non-saturated peaks. This provided estimations of peak values both smaller and larger than the actual peak value. In the sample of data used, errors of ±30% were common, and greater errors also occurred. For saturated peaks, the shape seems to be even less like the Gaussian curves. Therefore, the error when using this method on saturated peaks is expected to be even larger. This thesis does not attempt to estimate these shapes, and therefore ignores saturated data. This is unfortunate, but at least we can be quite confident that the data we do use are correct.

Another issue that would complicate matters if we used data from saturated channels is that the different channels saturate at different levels. This means that it can be difficult to even compare saturated data from different channels. This is due to the different offsets to each channel while recording data. It was done to make visual inspection of the data easier while experimenting, but it had this unfortunate effect.

5.4 Peak recognition

As we have previously shown, sometimes the noise does exceed 5σ, while some peaks from detector hits are smaller than this value. Therefore, just searching for maximum values does not find all peaks, and using all data over 5σ would find many false positives. In addition to that, some detector channels experience double hits for some sparks. These will not be found be simply finding each data file's maximum value. We expanded the criteria for defining a peak in the data in several ways.

We tested a set of parameters with certain values, visually inspected the data to see if real peaks and double peaks were identified, and that false peaks were not. Issues were identified, values of one or more parameters were changed, and the process was repeated until we were satisfied with the success rate of the method.

In the end, the criteria for defining something in the data as a peak were as follows. First, the data was smoothed with a smoothing width of 3 (just to reduce the highly frequent oscillations of the noise on top of the signal). If at least 22 out of 25 consecutive points are at least 5σ (of the smoothed noise) over the average value, a peak has begun, and the time is noted. This is done to recognize a rising trend, and also comes into play for double peaks.

While on a rising edge, the maximum value seen so far is continuously recorded. If the value of a certain point is below 2.5σ, the peak is over and the time is noted. The reason for using 2.5 instead of 5 is to allow for rising edges to have some points below the threshold for the start of a peak.

If the value of a certain point is below half of the maximum value seen so far in this peak, and at least 22 of the next 25 points are also below half of the maximum, a falling edge has started.

While on a falling edge, the lowest value seen so far is continuously recorded. If the value of a certain point is below 5σ, the peak is over and the time is noted. If a value is over 1.5 times the lowest value seen so far, and at least 22 of the 25 consecutive values are, a new peak is starting (double peak). The time is noted for end of one and start of a new peak.

It is possible to be on a rising or falling edge at the cut-off at 1.2 µs. If so, the peak is defined to instantly end at this point. Any such peaks are likely to be ripples after a channel is saturated.

The method described above is used to find the start and end of peaks. The actual values

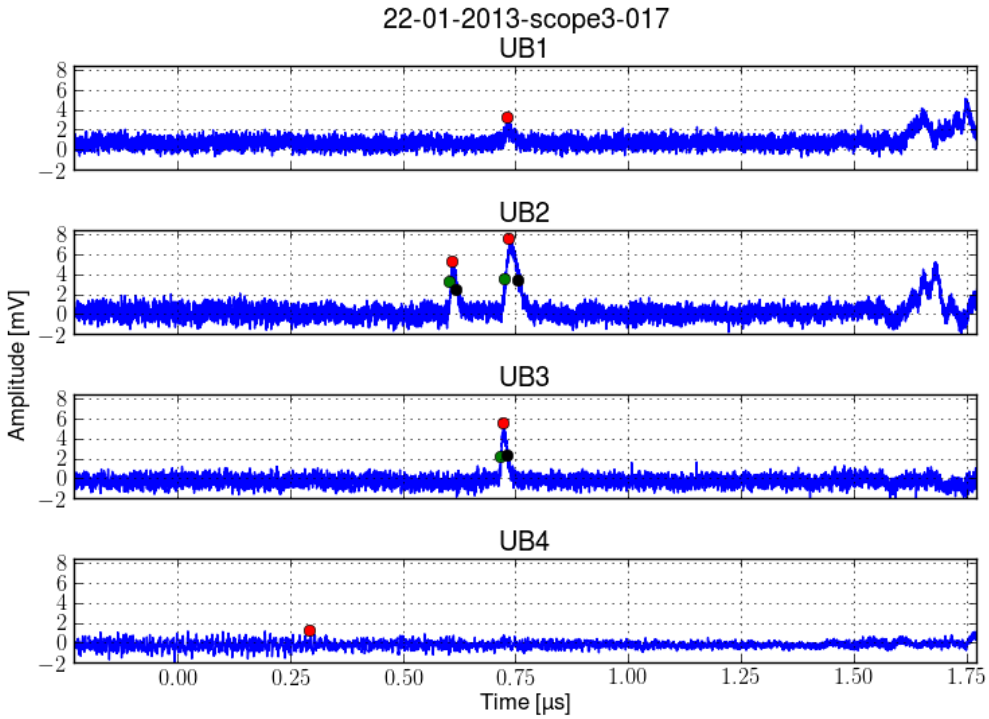

Figure 5.20: (Color) The automatic peak recognition method find beginnings and ends of peaks, and the maximum value between them. The start of a peak is marked by a *green dot*, the end of a peak by a *black dot*, and the peak maximum by a *red dot*. If no peaks are found, the maximum value is marked by a *red dot*.

are found from the raw data (even though the 3 point smoothing width does not make much of a difference). The peak value is defined as the maximum value between the points of the start and the end of a peak. An example is shown in Figure 5.20 which shows that both peaks in UB2 are detected. There are no peak detections at the end where there are some light leaks, because these are after the cut-off. The points for when the peaks start and end can seem to be quite high up on the peaks, but these are very small peaks. As previously discussed, lowering the threshold increases the amount of false positives.

The method is not perfect, and it is unlikely that any automated method of reasonable scope will be able to find all peaks and find no false positives. Visual inspection of the plots with the dots is useful for determining if the method is working acceptably well. Inspection of the plots can also help us include missed peaks, or filter out false positives.

5.5 Relative calibration of the detectors

Our fiber detectors were not standard equipment with manufacturer's data sheets for converting voltage readings to energy deposited in the detector. We performed relative calibrations of the detectors that let us compare signal strengths for different channels and let us estimate the relative amounts of energy deposited in the detectors.

The relative calibrations were done based on the data collected during the 200 calibration sparks, see section 3.3. For this setup, all detectors were placed right next to each other (ordered UB1, UB2, UB3, UB4, H1). This was done to justify the assumption that they all received the same amount of energy for each spark.

There is also the issue of how to actually compare the signals from different detectors. Several methods have been suggested, some have been tried. They all pose different challenges in defining the method in a robust way. The following section briefly describes different methods that could be used for comparing signals in two different channels. For all methods, a cut-off is applied at $t = 1.2$ µs.

- Maximum value in both data files.
- Maximum value in a data file paired with the maximum value in the other file within a limited time window.
- Integration of the signal in each data file.
- Integration of the part of the signal that is over 5 σ, for each file.
- Integration of the data from the beginning to the end of a peak, and comparing to the integration of a peak in another channel at roughly the same time.

By comparing signals for two adjacent detectors for the 200 calibration sparks, we can estimate a linear fit, which is an indication of the relative sensitivities of the two detectors. In the following subsections, we will describe in greater detail the methods of calibration mentioned above.

5.5.1 Maximum values

This is probably the simplest way of calibrating the detectors: Find the maximum value in the data file, and compare it to the maximum value in a data file for another detector for the same spark. Do this for all data files for each pair of detectors.

5.5.2 Simultaneous maximum values

This method is like the previous, but more sophisticated: Find the maximum value in a data file, and find the maximum simultaneous value for another detector for the same spark. The requires a definition of "simultaneous". In this context, we will use a time window of ±0.03 µs. This seems to be sufficient, based on visual inspection combined with trial and error with several different window widths.

An advantage of this method is that it can pick up weak hits ($< 5\sigma$) that would otherwise not be detected. This helps us compare signals with the same cause.

The method also requires us to decide between two options: 1) Use all pairs of data files. 2) Select just those pairs where it looks like the detectors were hit by anything at all (at a time close to the maximum of the first file).

5.5.3 Full integration

This method of calibration uses numerical integration of the signal as a measure of the energy deposited in a detector. The idea is that the integration of the noise will cancel out, leaving behind only what is caused by the signal itself.

There's very little difference between the results when using the common methods of numerical integration called the rectangle method and the trapeze method.

This and the next integration method does not take into account that for some sparks, some detectors seem to be hit twice, while others are hit once. Integration of the entire file would make it seem like the hit in one detector was much larger than in the other.

For some sparks, it seems like the average value of the noise changes. These data files cause outliers because integrating the noise does not cancel out. For data files with large peaks, this is not a big problem, since the area under the peak is much larger than the area under a shifted

baseline. For smaller peaks, this is a bigger problem. The cause of these shifts has not been further explored. There are only a few of these cases, and they matter only for this particular method.

5.5.4 High integration

This method is similar to the previous method, but it integrates only the part of the signal that is above 5 σ. This relies on the assumption that the signal from the hit in the detector will be the dominating part of the full signal for points over 5 σ. This is reasonable, especially for large peaks.

Unfortunately, as we showed in subsection 5.1.2, some peaks are hidden among the noise. This method of integrating would introduce a significant bias of missing weak hits, or at the very least underestimating them.

5.5.5 Peak integration

The final method integrates the signal from the beginning to the end of a peak, and compares it to the the integration of a peak in another channel at approximately the same time. If there is no simultaneous peak to compare it to, there are two options: 1) the peak is not used, or 2) the noise in the other channel between the same points of time is integrated and compared to the peak integration.

This method inherits the same issues as were mentioned in the other integration methods above. It does not perform well for small peaks, because a significant part of them is lost before peakstart and after peakend are defined, see Figure 5.20.

5.5.6 Linear regression

We applied a linear regression method to the points to obtain linear fits to the data. The most common method to use is the method of least square deviations (LSD). This method attempts to minimize the sum of the squares of the deviations from the linear model. An alternative is a similar method known as least absolute deviations (LAD). This method attempts to minimize the absolute value of the deviations from the model. This means that outliers are weighted

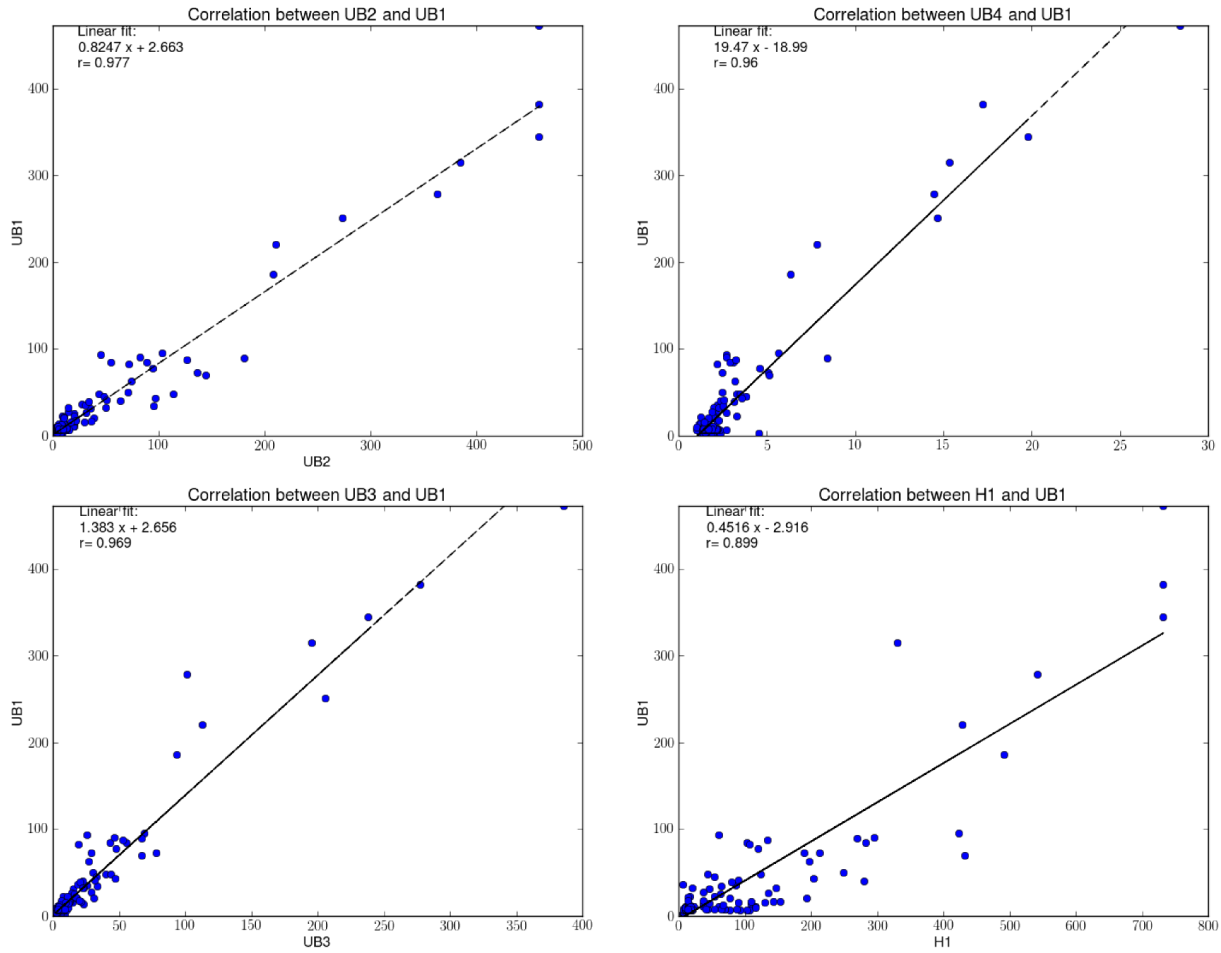

Figure 5.21: Relative calibrations of UB1 with UB2, UB3, UB4 and H1 using the maximum value method described above. The linear regression is done using least square deviations.

less. We used LSD to perform the relative calibrations of the detectors by the maximum values calibration method.

5.5.7 Calibration results

In this subsection we briefly present the results of the calibrations. First, Figure 5.21 shows the linear fits for calibrating UB2, UB3, UB4 and H1 to UB1.

The linear fits are listed in Table 5.2. By using these fits, UB1 will be the basis for the comparison of signals. The fit for H3 to UB1 is very poor, and is not included. It is difficult to get a relative calibration of H3, since it was not included in the initial 150 calibration sparks, but only for the last 50. Since the detectors are not hit during every discharge, there is not a lot of data to

Detector	Linear fit	r-value
UB2	$0.8247x + 2.663$	0.977
UB3	$1.383x + 2.656$	0.969
UB4	$19.47x - 18.99$	0.96
H1	$0.4516x - 2.916$	0.899

Table 5.2: This table shows the linear fits for comparing signals in UB2, UB3, UB4 and H1 to signals in UB1. These fits were made using maximum values and a least square deviation method.

use for the calibration.

Chapter 6

Discussion

First, we will discuss the calibrations of the fiber detectors. Second, simulations and detector sensitivities. Third, other analyses that could be done using the data we have collected and prepared for analysis. Fourth and last, we will discuss limitations to the work and results in this thesis not explored elsewhere.

6.1 Calibrations

The calibrations we have performed are done using the maximum value method described in section 5.5. Any analysis that builds on the calibrations will of course rely on the calibration, and there is no guarantee that the selected method is the one best suited for our kind of experiments. Below, some issues and concerns regarding the calibrations are discussed.

6.1.1 Equal energy deposited

The relative calibrations of the detectors were performed assuming they all receive the same amount of energy for each of the 200 calibration sparks. To justify the assumption, we placed the detectors right next to each other. Unfortunately, this assumption does not really hold for all sparks (and maybe not for any sparks). Two examples of are shown below.

Figure 5.20 shows that the detectors UB1, UB2 and UB3 are hit by relatively weak signals at almost the same time, while UB2 are also hit by something before the other hits. UB4 is not hit by anything. H1 is not shown, but is not hit by anything for this spark. This implies two things:

1) That three detectors next to each other on one end of the line of detectors are hit at the same time, while the two detectors at the other end are not hit. 2) That one detector between other detectors are hit by something none of the others detect. It is a weak signal, so it is conceivable that it was just too weak for the signal to be visible in the other channels.

Figure 4.10 shows that UB2 and H1 are saturated, while the other detectors are not hit by anything that creates a visible signal. Since UB2 is located between other detectors, this and similar (but much less energetic) events provide evidence contrary to the original assumption. It is possible that the signals measured here are not real, but it seems unlikely that two different oscilloscopes should malfunction within the same 2 μs window, around the same time that we usually see detectors hit.

We have discussed some problems with the assumption that all detectors receive the same amount of energy at the same time. Still, for most of the sparks, the assumption seems to hold true. We regularly see all detectors hit at the same time, with either all or no channels being saturated.

6.1.2 Different calibration methods

The observations in the previous subsection introduce a dilemma regarding the relative calibrations. One option is to use the algorithms for relative calibrations on the data from all sparks. Another is to look at the data and apply the algorithms only to data where it's clear that a pair of detectors are both hit. The first option may very well decrease the reliability of the calibration. One reason is the imperfect assumption that a pair of adjacent detectors are hit by the same amount of electrons and photons with the same energies. The other option may introduce an error due to possible error or bias when deciding for which sparks a pair of detectors are both hit. Since detectors are not always hit at the same time (see Figure 5.20), a method that takes timing into account might be the most appropriate for comparing signals in different channels.

We have presented five different methods that could be used for performing a relative calibration of the detectors. It seems reasonable that taking simultaneousness into account should provide a more accurate calibration. It may be more suitable to compare areas than just peak values. A definite answer to this issue is difficult to ascertain.

The downside to using more sophisticated methods of comparing signals is that they require

us to make some decision on what the criteria should be, and this could introduce some bias. In addition, methods requiring manual input are very time consuming.

We should keep in mind that some data were removed as described in section 4.3, and that saturated data is ignored. It might be worthwhile to do the calibrations again if a suitable way of estimating values for the saturated data is found.

6.1.3 Indirect calibrations

A consequence of performing this kind of relative calibrations of the adjacent detectors, is that by transitive properties of the linear relations, we indirectly get relative calibrations between all the detectors. The implication is that even though we assume only that adjacent detectors receive the same amount of energy, we implicitly assume that all detectors receive the same amount of energy. If UB1 and UB2 are hit equally hard, and UB2 and UB3 are hit equally hard, then UB1 and UB3 are also hit equally hard, and so on. To assess the validity of the calibrations, one could also perform relative calibrations of all pairs of detectors directly.

6.1.4 Linear regression

There is no defined "best" way to perform a linear regression. Least square deviation (LSD) is guaranteed to have just one solution, while least absolute deviation (LAD) can have infinitely many solutions. On the other hand, LAD is more robust regarding outliers. In our case, outliers occur mostly when using automated methods that do not require simultaneous hits in both detectors being compared. When the automated methods are complemented by visual inspection and manual filtering of the registered data, outliers should appear less often. Therefore, it can be reasonable to use LSD when manual filtering is applied, and to use LAD for the simpler automated methods.

6.2 Sensitivity analysis

To be able to perform data analysis, we need to know whether the signals from our fiber detectors stem from electrons or photons (or both). We have performed a sensitivity analysis to

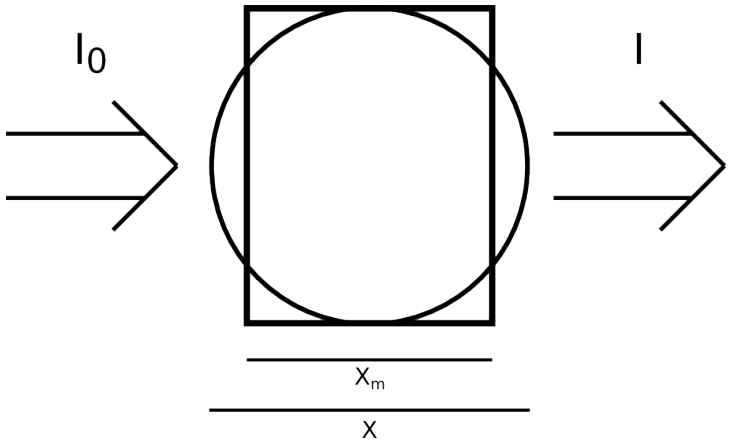

Figure 6.1: The circle represents a 1 mm detector fiber, while the rectangle represents a plate of the average thickness of the detector. The diamater of the circle is X, and the thickness of the plate is X_m. This average is $\pi d/4 \approx 0.785$ mm. I_0 represents the intensity of an incoming beam of photons, while I represents the intensity of a beam of photons after passing through the detector, from left to right.

estimate the detectors' sensitivities for electrons and photons of different energies. This consists of two simulations: 1) The attenuation of the intensity of the flux of photons of different energies while passing through a detector, and 2) the energy deposited by electrons of different energies while passing through (or stopping inside of) a detector.

Both simulations are set up in the same way. Each detector consists of five pieces of round pieces of plastic, 1 mm in diameter, covered by a 0.15 mm sheet of plastic. The amount of material the electrons and photons have to pass through differs depending on where they hit the detector. To simplify, we used a plate of the average thickness of the detector in the simulations, see Figure 6.1.

The electrons and photons start right outside of the shielding that covers the detector, and move through it in a direction perpendicular to the detector's length. This means they pass through the plate in Figure 6.1 in the way indicated by the arrows.

The photon sensitivity analysis was performed based on data from the bibliography of photon cross sections by Hubbel (1994), which we collected from the National Institute of Standards and Technology (NIST) at `http://www.nist.gov/pml/data/xraycoef/`. The electron sensitivity analysis was performed based on electron stopping power data from the International Commission on Radiation Units and Measurements, which we collected from NIST at `http://www.nist.gov/pml/data/star/`. For both cases, we used data corresponding to a

plastic scintillator (vinyltoluene based), with a density of 1.032 g/cm^3. This is not the exact same material as the material in the actual plastic scintillators used, which has a density of 1.05 g/cm^3. but it seems reasonable to assume the materials are similar. Unfortunately, the data is limited to photon and electron energies from 10 to 1000 keV.

6.2.1 Sensitivity to photons

This simulation relies on the exponential attenuation law for a narrow beam of monoenergetic photons:

$$\frac{I}{I_0} = e^{\left(-\frac{\mu}{\rho}\varrho\right)} \tag{6.1}$$

where I_0 is the initial intensity and I is the intensity after the beam has passed through the material. μ/ρ is the mass attenuation coefficient with units cm^2/g. The numerical values are found in tables for different photon energies. Finally, $\varrho = \rho\delta$ is the mass thickness, which is the amount of mass the photons will pass when moving through material of thickness δ with mass density ρ. In our case, Equation 6.1 can be rewritten by substituting $\rho\delta$ for the mass thickness ϱ and $\pi d/4$ for the thickness δ.

$$\frac{I}{I_0} = e^{\left(-\frac{\mu}{\rho}\rho\pi d/4\right)} \tag{6.2}$$

For each photon energy, we found the intensity after the beam had passed through the shielding, and the intensity after the beam had passed through the fiber. The difference between the intensity before and after the fiber is the fraction of photons that interacted with the detector material and deposited energy. The fractional decrease of the number of photons inside the detector is shown in Figure 6.2.

The highest photon intensity decrease in the detector happens for low energy photons. This means that higher energy photons are more likely to pass through the detector without interacting. All photons of 30 keV or more has less than 2 % chance of interacting with a fiber while passing through.

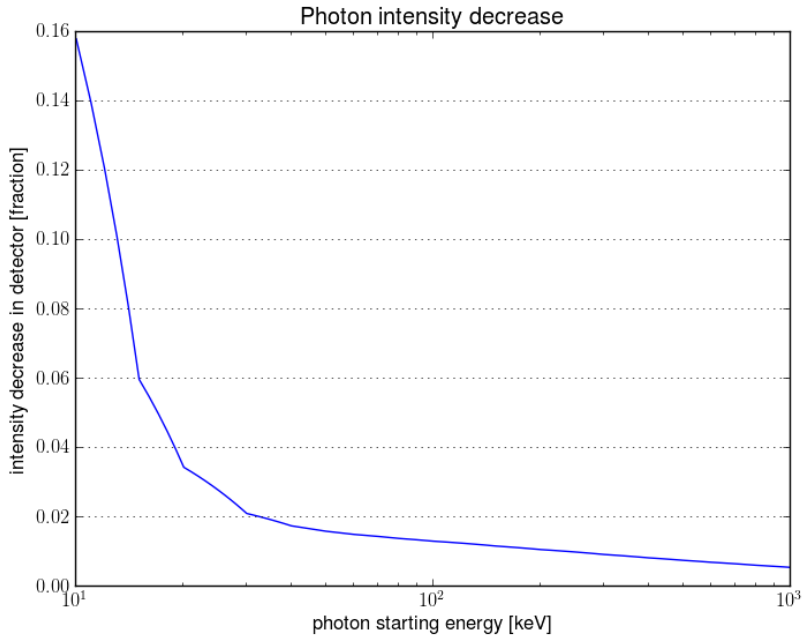

Figure 6.2: The fraction of the photons in a beam that is absorbed in the fiber, as a function of photon energies. This can be seen as the probability that a single photon is absorbed in the detector.

6.2.2 Sensitivity to electrons

This simulation follows single electrons of different starting energies moving through the detector. In our simulations, electrons moves in steps of 0.001 mm, and the expected energy loss for each step is computed based on the stopping power for each electron's current energy. If the current energy is not in the table of stopping powers, linear interpolation is used to estimate the stopping power. For energies below 10 keV (the lower limit of the data range), the stopping power for 10 keV is used. This is done only for a few steps for each electron before they lose the remaining energy.

The process continues until the electron stops (loses all its energy), or until it passes through the fiber. The energy deposited in a fiber is shown in Figure 6.3. 100 keV is the minimum energy required to get through the shielding. The stopping power graph for electrons in plastic has a shape similar to the one for electrons in air (Figure 2.8). Higher energy electrons will experience less frictional losses per step, and electrons will get progressively further into the detector. Because of the diminishing frictional force at higher energies, an electron that stops just before

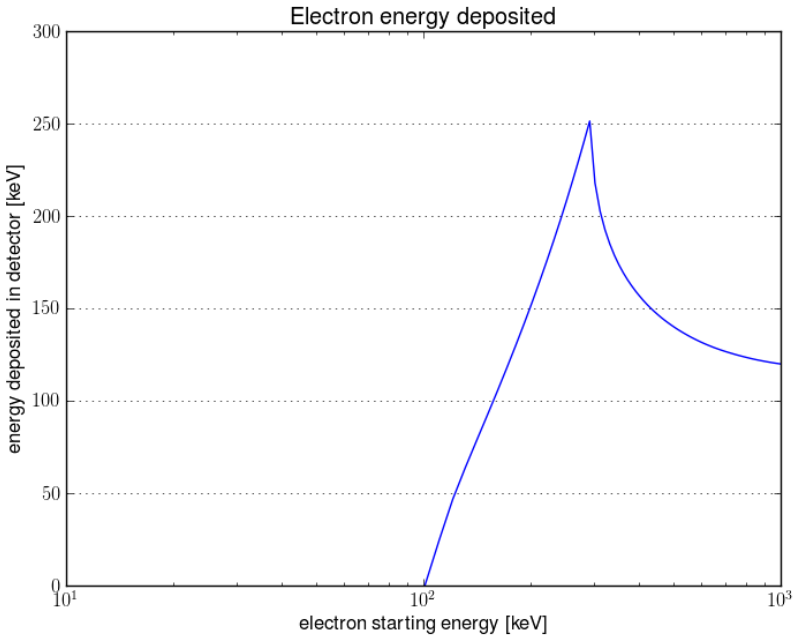

Figure 6.3: The amount of the electron energy that is deposited in the fiber, as a function of electron energy. All electrons starting at less than 100 keV stops within the shielding around the detector. All electrons between 100 and 300 keV stop inside the fiber, depositing all their energy in the shielding and the fiber. All electrons at 300 keV or more pass through the fiber, depositing only part of their energy.

leaving the fiber will deposit the most energy within it. At 300 keV, the electrons get through the detector with 44 keV spare energy, and for increasing energies, the deposited energy is decreasing.

To simplify comparison between sensitivities to electrons and photons, we also present the energy deposited as a fraction of the initial energy in Figure 6.4. The maximum at around 290 keV is at around 85 % energy deposited in the detector.

6.2.3 Electron stopping power in air

The previous simulation was performed for electron energies as they reached the shielding. In reality, they will have to pass through some distance of air from where they are produced to get to the detectors. Passing through air also reduces electron energies. We simulated electrons moving through air with no background electric field, and with a homogeneous electric field in the direction of the electron propagation. The simulations used data for electron stopping

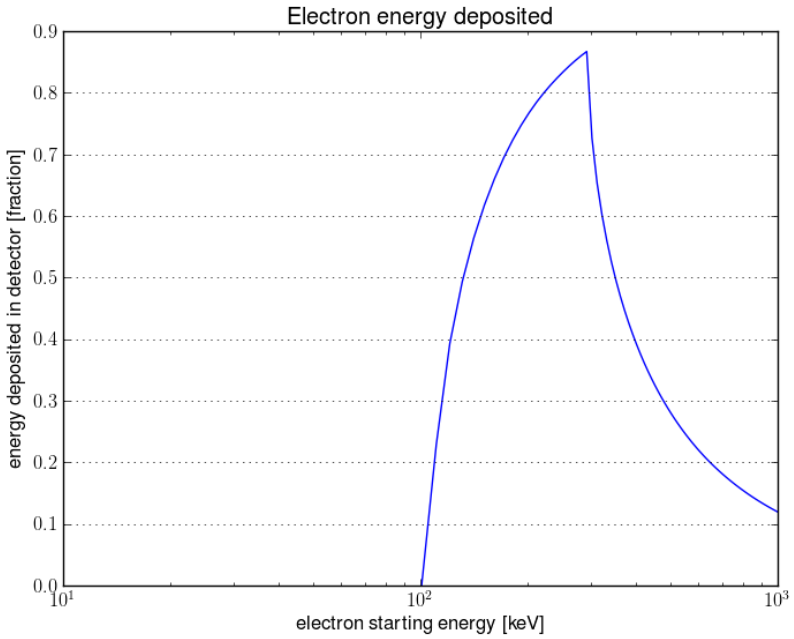

Figure 6.4: The fraction of energy deposited in the fiber by electrons of different energies.

power in air from the International Commission on Radiation Units and Measurements, which we collected from NIST.

The simulations are done similar to the previous one. Each electron moves a short distance. The stopping power is found in the data table, or by linear interpolation. If the electron energy is less than 10 keV, the stopping power for 10 keV is used for the last steps. For each step, the electron energy is reduced according to the stopping power. For the case with an electric field, electron energy is increased according to the field strength and step length. When an electron's energy reached zero, the simulation for that electron ended. For the runaway cases, the simulation was stopped at 1000 keV. The electric field used in this simulation was a homogeneous field of 1000 kV / 107 cm, and electrons were moving along the field (opposite of the field's direction).

Figure 6.5 shows the simulation with no electric field. 150 keV electrons have a range of around 25 cm, 300 keV electrons a range of 78 cm, and 450 keV electrons a range of 140 cm. Electrons at 60 keV or less move less than 7 cm before stopping. Figure 6.6 shows the simulation where electrons are accelerated by moving parallel to the electric field. The threshold for electrons to become runaway electrons is at 34.7 keV. Electrons of lower energies than 25 keV stop after short distances of just 5 cm.

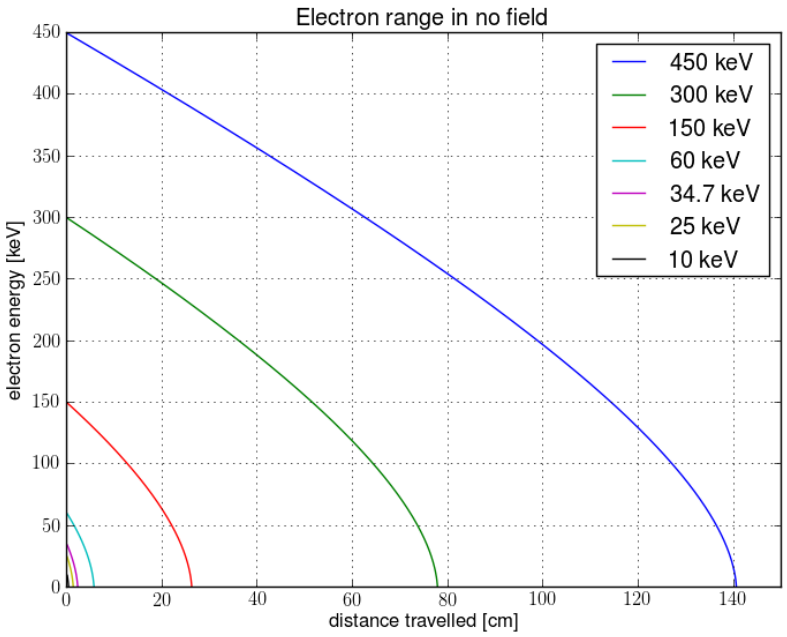

Figure 6.5: (Color) The range of electrons of different starting energies moving through air.

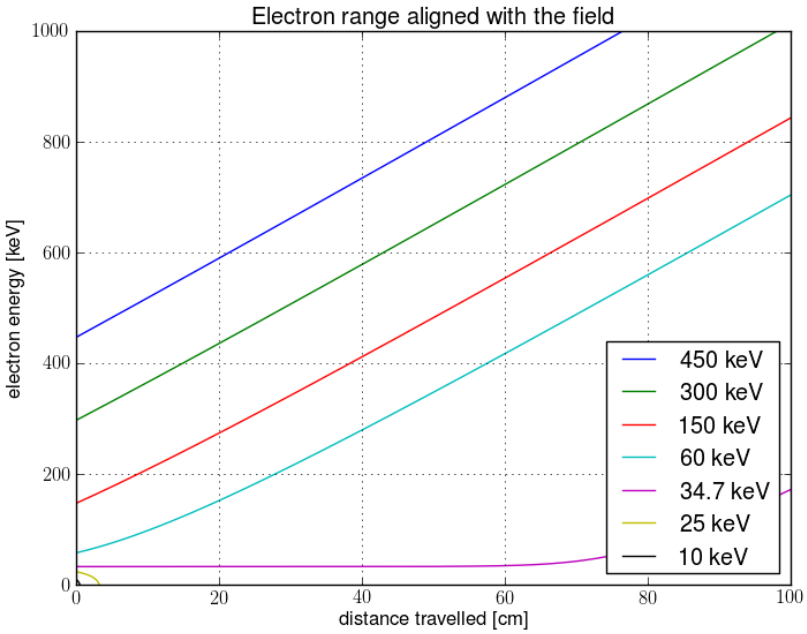

Figure 6.6: (Color) The range of electrons of different starting energies moving through air parallel to a homogeneous electric field of approximately 1000 kV/m. Electrons with less than 34.7 keV starting energies stop after a short distance. Electrons with more than 34.7 keV starting energies become runaway electrons.

6.2.4 Comments

Since we do not have absolute calibrations of the detectors, we do not know at what levels of deposited energy the signal becomes discernible from the noise. This leads us to a mostly qualitative discussion.

We will begin by addressing the effects of the available data, or rather the data we do not have. Both the photon and the electron sensitivity simulations are done using data for 10-1000 keV. For the electron simulations, we expect no significant change if we had been able to use data for lower energies. When an electron's energy is reduced to 10 keV, only a few more steps are needed before the rest of the energy is lost in the detector. For photons, we will refer to Figure 6.2. We expect lower energy photons to have an increasing intensity reduction within the detector, up to a certain point where they no longer get through the shielding. Even though we expect more photons to be absorbed, we expect the low energy photons to not produce peaks in the data, because the deposited energy is reduced. We know that the photons from visible light does not produce peaks, or we would have constant saturation of the channels. Therefore, at low enough energies, photons are not detected.

Sensitivity to photons

We refer to Figure 6.2, which shows the fraction of a beam of photons that are absorbed in a detector fiber. For 10 keV energy photons, around 16 % of the photons entering the shielding are expected to be absorbed in the detector. For higher energies, fewer photons are expected to be absorbed. For 30 keV, only 2 % of the photons will be absorbed, and for 300 keV, the rate is only around 1 %. For the energies in the data (10-1000 keV), the fraction is decreasing towards zero. However, more energy might be deposited from 1 % of the 300 keV photons than from 16 % of the 10 keV photons. This depends on the spectrum of photon energies.

We know that the detectors are more sensitive for low energy photons than high energy photons, only a few percent of the higher energy photons will deposit energy in the detectors. We can not know for sure what range of photon energies deposits the most energy in the detector. It can be several low energy photons, a few high energy photons, or some combination.

Sensitivity to electrons

We refer to Figure 6.4, which shows the energy deposited in the detector by electrons of different energies. Our detectors are not able to detect electrons with less than 100 keV when they reach the detector, and are most sensitive for electrons of 300 keV. For higher electron energies, the deposited energy seems to level off at around 120 keV. All electrons of 200 keV or more deposits at least 120 keV. Again, we do not know at what levels of deposited energy the peak in the signal is discernible from the noise. Therefore, we can not know for sure what the minimum electron energy must be for it to be found in the data. We do know that it must be at least 100 keV, since all electrons with less energy are expected to be absorbed in the shielding.

The electron energies mentioned above are the energies at the time when electrons reach the shielding. If this movement happens to be directed so that the electrons gain energy from the field, the original energy could be as low as 35 keV. Figure 6.6 shows that ~ 35 keV is the threshold for electrons to run away in a homogeneous 1000 kV/m electric field if they move along the field. Since the actual field is not a homogeneous field along a line from the source location to each of the detectors, the actual lower limit is higher than 35 keV.

The field used in simulations is a simple field of around 1000 kV/m. The actual field varies, and rises towards this value. At the typical times when we see detectors being hit, the potential difference is around 800 kV, which means that even a homogeneous field over the entire gap would be around 800 kV/m. Two consequences are that the runaway limit is higher than 35 keV, and that any acceleration or deceleration of electrons is less than for the simulated numbers.

The lower production energy limit for electrons to be detectable also depends on the distance from the source location to the detectors. For a beneficial field configuration, a longer distance between source and detector location allows electrons to gain more energy, and thus the limit is lower than for other combinations of locations and field configuration.

For combinations of field configurations and source and detector locations where electrons are decelerated by the field while moving towards the detectors, only electrons that start at more than 100 keV will be detectable. This also applies to scenarios where the field strength is negligible in the volume where the electron moves. As shown by Figure 6.5, electrons lose energy over quite short distances in air with no field. In the extreme case where we neglect any effects from the field after electron production, electrons would need a minimum of around 200 keV to

reach detectors with 100 keV left, depending on source and detector locations.

When considering the range of electrons in air, it is useful to consider the distances we expect electrons to be moving. In chapter 3 we presented several tables of detector positions. For most of the experiments, the distances from the high voltage electrode to the detectors are around 80 cm. In the absence of an electric field, an electron should start at around 350 keV to have 100 keV left when it reaches the detectors. Aligned with the field, electrons over 35 keV will be accelerated to over 100 keV in less than 80 cm, and will thus be detectable. The electric field will in general accelerate electrons toward the ground, away from the negative high voltage electrode. If electrons are produced above the detectors, they will gain some energy from the field. If they are produced below the detectors, they will lose some energy to the field.

We have several cases of just one detector being hit (or even saturated) when they are placed right next to each other, and we know that our detectors are most sensitive to high energy electrons and low energy photons. It seems unlikely that one detector is hit by many low energy photons, and that no photons hit the nearby detectors (when we see no signal in other channels). Therefore, we expect these cases to be caused by single higher energy electrons rather than lots of photons that happen to hit just one detector. A simulation of the expected flux of electrons from streamers and the subsequent flux of photons could provide expected numbers of electrons and photons of different energies, and help settle this case.

To summarize: The minimum energies electrons need to be created with to be detectable are around 35 and 200 keV, depending on field configuration and the locations electrons are produced in relative to the detector locations. We know that the detectors are more reliably sensitive for electrons, at least for energies over a certain level. We believe that the signals are caused by electrons.

6.2.5 Angle of incidence

The simulations of electrons and photons passing through a plate is an approximation for a circular fiber. In reality, some electrons and photons will pass through the fiber along the diameter (longest distance), and some will pass through closer to the edge (shorter distance). This causes them to deposit more or less energy in the detector than what is calculated in our simulations.

In addition, electrons or photons will most likely not hit the fibers head-on, but at some

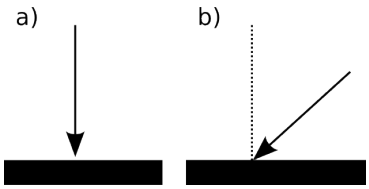

Figure 6.7: The two arrows indicate electrons or photons hitting the detectors head on or at some angle of incidence.

angle of incidence. Image a) in Figure 6.7 indicates electrons or photons hitting the detector in a direction perpendicular to the fiber length. This is how the simulations were run. Image b) indicates electrons or photons going through the fiber at an angle. In this case, they will have to pass through a thicker layer of shielding before getting to the scintillating fiber, but they will also pass through more of the fiber.

This has three effects for electrons: 1) The threshold for electrons to make it into the scintillating fiber is increased, depending on the angle of incidence. 2) The energy deposited for electrons between 100 and 300 keV is decreased, because they lose more to the shielding. 3) The electrons that passed through the fiber (plate) in our simulations would travel a longer distance inside the fiber, and thus deposit more energy. The higher threshold to get into the detector causes the curve in Figure 6.4 to shift to the right. The increased energy deposit for electrons that passed through the detector causes the rising edge to extend, and the curve on the right side of the peak to be shifted up.

For photons, different incidence angles will increase the travel distance through the shielding and through the detector. This means that the shielding absorbs a greater fraction of the initial number of photons in a beam. It also means that the fraction of remaining photons that are absorbed in the detector increases. Depending on the angle of incidence, a greater or smaller fraction of the initial number of photons are absorbed in the detector.

To summarize: Incidence angles greater than zero increases the sensitivity for higher energy electrons, but decreases sensitivity for lower energy electrons, and raises the threshold for electrons to be detected at all. Increasing the incidence angle also changes the sensitivity for photons. This change can be an increase or a decrease, depending on the angle.

6.3 Other analyses

We will describe some other analyses that could be done using the data we have collected. These will to some degree use work presented here.

6.3.1 Electron source locations

To estimate a source location for the electrons, we have created a limited model for simulating electrons. We choose different locations in and around the spark gap, determine the expected relative signal strengths, and compare these to the actual relative signal strengths. This is done for the polar experimental setup.

The space in and around the spark gap was divided into cells. Due to geometrical symmetry, some sections of the space around the spark gap are ignored. We simulated electrons of starting energies of 350 keV moving from each cell in a homogeneous electric field. The electron energies when the electrons reached the detector was compared to the simulations in subsection 6.2.2 to find the expected deposited energies in each detector. The relative levels of expected deposited energies were compared with the relative levels of the measured signal strengths (after applying the calibration scalings). The location of cell that produces the lowest magnitude sum of the square deviations between estimated and measured relative signal strengths is saved.

The process was repeated for all sparks for the radial experiment setup, but even for a 33-hour long run of the program, the grids were not fine-meshed enough. For future simulations, the code should be optimized, run on better hardware, or be allowed longer run-times. An example of what the result would look like can be seen in Figure 6.8. Together with a view along the horizontal axis of this figure and a top-down view the three-dimensional distribution of source locations could be determined. Due to time limitations, this work could not be completed in this thesis.

Similar simulations could be performed for photons to estimate where they would need to start to produce the observed relative signal strengths. The electric field geometry used in the simulations could also be improved.

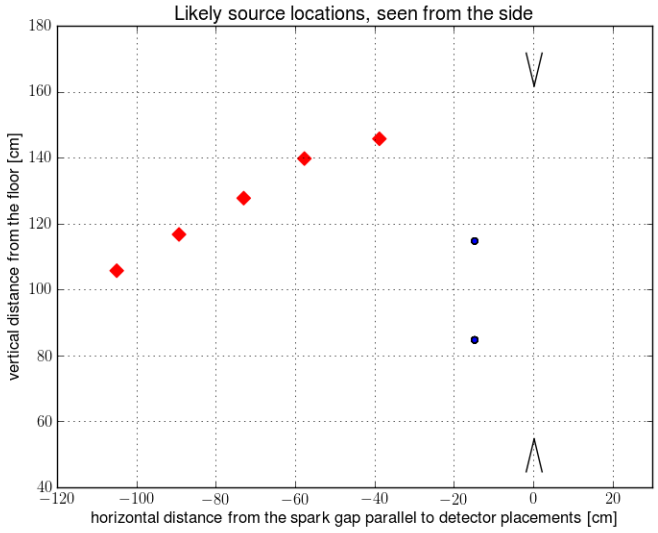

Figure 6.8: (Color) Estimations of electron source locations, seen from the side of the spark gap and the polar geometry detector setup. The *red squares* represent detector positions, the *blue circles* represent estimated source locations for some sparks. The two *black triangles* at 0 on the horizontal axis represent the two electrodes.

6.3.2 Other simulations

Our simulations of electrons and photons passing through the detectors could be improved by giving them a range of angles of incidence. We could also simulate using a circular cross-section, instead of the rectangular one we did use. If one can find suitable data for the absorption of photons in plastic for low energy photons, the sensitivity analysis could be extended. The electron sensitivity analysis would likely not change significantly even if we did have the correct stopping powers for energies below 10 keV.

Based on the electron numbers and energies found in the streamer simulations of Celestin and Pasko (2011), one might be able to simulate the electrons and photons produced by them. It might be reasonable to assume that the electrons produced in streamer tips have some directional distribution. One option is a two-dimensional normal distribution. An example is shown in Figure 6.9. Assuming a beam like this from different source locations, one could try to fit the simulation to data from the LaBr x-ray detectors. They were active and in the same location for all 950 sparks. This could help us set some constraints on source locations and beam size. For quite a few of the sparks, just one of the two detectors is hit.

Since the LaBr-detectors are properly calibrated, we know the energy deposited per peak.

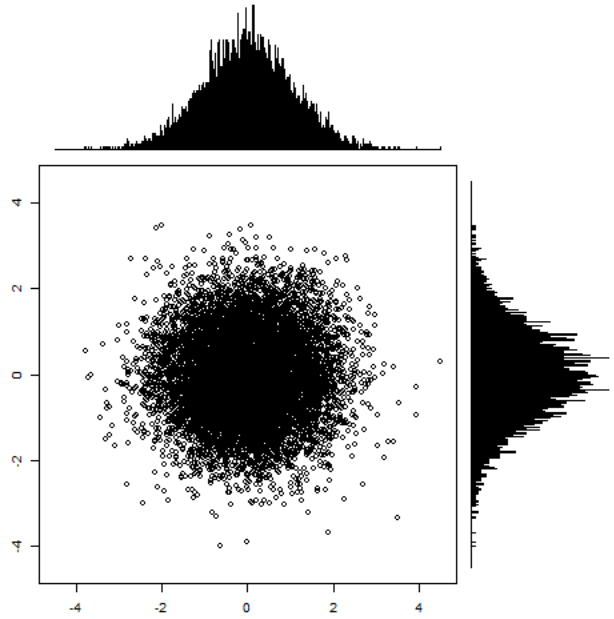

Figure 6.9: An example of a sample of a two-dimensional normal distribution.

Examining the recorded spectrum could grant insight in the spectrum of photons, which could again grant insight in the spectrum of electrons producing these photons. The detectors are likely to be hit by several photons per peak for at least some of the peaks. One could study how the detectors react to x-rays of different energies hitting the detector at almost the same times to be able to discern between peak shapes from single x-rays of higher energies and peak shapes from several x-rays of lower energies.

Similar simulations could also be done for the different detector geometries described in chapter 3. This would use the sensitivity analyses for electrons and photons to estimate expected relative peak sizes, since we do not have absolute calibrations for the detectors. If the result of such work does not fit the measured data, one explanation is that there might just not be such a beam for these experiments.

6.4 Limitations

We will briefly explain some limitations and factors that should be taken into account regarding the work in this thesis, that have not already been explored elsewhere.

For the radial and polar geometry setups, some of the detectors may cause a "shadow" on

other detectors by blocking electrons from reaching them. This depends on the source location. This would cause the detectors to receive less energy than they otherwise would in a certain position for a certain source location.

The oscilloscopes and the other electronics are not perfectly identical, and we do not know how much this matters, or if it matters at all. There seems to be different magnitudes of noise in the different channels. One explanation is differences in electronics. Another is differences in the fiber detectors.

The assumption that the noise in the data follows a normal distribution may be incorrect. We do sometimes see single data points over 5 σ. These can have some other explanation than just the random variation of the noise. This issue is handled in part by introducing the more advanced methods for peak recognition. Signal processing is a field of its own, and even more sophisticated methods could be implemented.

We did not measure the humidity or air pressure in the laboratory. We assume them to be the same for all sparks. The sparks produce ozon, which changes the composition of the local atmosphere. We could notice the smell, but we do not know how much there actually was, or if it makes a difference for the generation of sparks or the propagation of electrons.

The source location most likely varies from spark to spark. This can affect all comparisons of measurements in some way, since the energy deposited varies with the distance electrons travel before hitting the detectors.

We do not know for sure whether the detectors amount of energy transformed to light inside the fiber detectors is directly proportional to the energy deposited in the detectors. We do not know for sure that the photomultiplier tubes output a voltage directly proportional to the incoming energy. Still, we have assumed direct proportionality in all elements.

The last item may be the most important: We do not know what knowledge of laboratory sparks can be applied to natural lightning. The atmospheric conditions are different. The potential differences and the electric field configurations are different. If nothing else, at least knowledge of laboratory sparks can help us decide which aspects of lightning to study, and how to do so.

Chapter 7

Summary

7.1 Summary and conclusions

In this thesis, we have presented a brief review of literature relevant to terrestrial gamma-ray flashes (TGFs) and laboratory sparks. We presented theories governing laboratory sparks and some theories of TGFs. The experiment setup and the raw data has been thoroughly described. We have developed and discussed different tools and methods for data processing and performed a relative calibration.

We have also discussed whether the signals from the detectors are caused by electrons and photons, and argued that they are most likely caused by electrons. A model for estimating the source locations for the electrons have been suggested, but is not fully developed. Finally, we discussed several issues and limitations with the work presented here. The objectives stated in section 1.3 have been met. Taking the development of the model(s) for electrons and photons moving through air and the detectors into account, objectives have in a way been exceeded.

7.2 Recommendations for future work

The work presented here has prepared the way forward for future analyses. There is great potential for future work. In our experiments, we had a total of 950 sparks. Most previous scientific papers on laboratory sparks use well under 100 sparks. We have collected and prepared a great amount of data, both from the LaBr detectors (always in the same location) and our scintillating

fiber detectors (in different configurations).

7.2.1 Connecting source location and timing

As mentioned in the previous chapter, we have started working on estimating source locations for the electrons that hit the detectors. This seems promising, and we have mentioned several ways the model could be improved.

If the source locations can be determined, the time of electron production could be estimated based on expected electron energies and distance. This could in turn be connected to the work on stereo photography of streamers presented by Nijdam et al. (2008) and work on the spatio-temporal development of metre-scale sparks by Kochkin et al. (2014). This should also be combined with the theoretical work of Cooray et al. (2009) and Celestin and Pasko (2011) on energies of electrons ejected from streamer tips to further improve the quality of our models.

Our simulations have so far used homogeneous electric fields, which are poor representatives for the actual field configuration. One option is to introduce a dipole field (modelling point charges on the electrode tips).

7.2.2 Attenuator experiments

During our experiments, we did a few series of sparks with different attenuators covering the detectors. We can calculate the expected loss of energy for electrons passing through the attenuators, and we can compare signals in different channels using our relative calibrations. It might be possible to learn more about the electron and photon sensitivities by analysing these data.

7.2.3 Signal processing

Much of what we have presented in chapter 5 falls under the topic of signal processing. More advanced methods could improve the calibrations, peak-finding algorithm and thus the following analyses.

7.2.4 Saturated peaks

The saturated peaks are intriguing, they are the most energetic signals. It would be interesting to do an experiment with large enough dynamic ranges in the oscilloscopes to never get saturated channels. Such an experiment should have some detectors connected to channels with narrower ranges to see if any comparison between weak and strong hits can be done.

Bibliography

Berger, M. J., Hubbell, J. H., Seltzer, S. M., Chang, J., Coursey, J. S., Sukumar, R., Zucker, D. S., and Olsen, K. XCOM: Photon Cross Section Database, 1998.

Briggs, M. S., Fishman, G. J., Connaughton, V., Bhat, P. N., Paciesas, W. S., Preece, R. D., Wilson-Hodge, C., Chaplin, V. L., Kippen, R. M., von Kienlin, A., Meegan, C. a., Bissaldi, E., Dwyer, J. R., Smith, D. M., Holzworth, R. H., Grove, J. E., and Chekhtman, A. First results on terrestrial gamma ray flashes from the Fermi Gamma-ray Burst Monitor. *Journal of Geophysical Research*, 115(A7):1–14, July 2010. ISSN 0148-0227. doi: 10.1029/2009JA015242.

Briggs, M. S., Xiong, S., Connaughton, V., Tierney, D., Fitzpatrick, G., Foley, S., Grove, J. E., Chekhtman, A., Gibby, M., Fishman, G. J., McBreen, S., Chaplin, V. L., Guiriec, S., Layden, E., Bhat, P. N., Hughes, M., Greiner, J., von Kienlin, A., Kippen, R. M., Meegan, C. a., Paciesas, W. S., Preece, R. D., Wilson-Hodge, C., Holzworth, R. H., and Hutchins, M. L. Terrestrial gamma-ray flashes in the Fermi era: Improved observations and analysis methods. *Journal of Geophysical Research: Space Physics*, 118(6):3805–3830, June 2013. ISSN 21699380. doi: 10.1002/jgra.50205.

Carlson, B. E. *Terrestrial gamma-ray flash production by lightning*. Ph.d. thesis, Stanford University, 2009.

Carlson, B. E., Lehtinen, N. G., and Inan, U. S. Constraints on terrestrial gamma ray flash production from satellite observation. *Geophysical Research Letters*, 34(8):1–5, April 2007. ISSN 0094-8276. doi: 10.1029/2006GL029229.

Carlson, B. E., Lehtinen, N. G., and Inan, U. S. Runaway relativistic electron avalanche seeding

in the Earth's atmosphere. *Journal of Geophysical Research*, 113(A10):A10307, October 2008. ISSN 0148-0227. doi: 10.1029/2008JA013210.

Carlson, B. E., Lehtinen, N. G., and Inan, U. S. Terrestrial gamma ray flash production by lightning current pulses. *Journal of Geophysical Research*, 114, December 2009. ISSN 0148-0227. doi: 10.1029/2009JA014531.

Celestin, S. and Pasko, V. P. Energy and fluxes of thermal runaway electrons produced by exponential growth of streamers during the stepping of lightning leaders and in transient luminous events. *Journal of Geophysical Research*, 116(A3):A03315, March 2011. ISSN 0148-0227. doi: 10.1029/2010JA016260.

Coleman, L. M. and Dwyer, J. R. Propagation speed of runaway electron avalanches. *Geophysical Research Letters*, 33(11):1–4, 2006. ISSN 0094-8276. doi: 10.1029/2006GL025863.

Cooray, V. Mechanism of electrical discharges. In Cooray, V., editor, *The Lightning Flash*, chapter 3, pages 45–126. Institution of Electrical Engineers, 2003.

Cooray, V., Arevalo, L., Rahman, M., Dwyer, J., and Rassoul, H. On the possible origin of X-rays in long laboratory sparks. *Journal of Atmospheric and Solar-Terrestrial Physics*, 71(17-18):1890–1898, December 2009. ISSN 13646826. doi: 10.1016/j.jastp.2009.07.010.

Cummer, S. a. Measurements and implications of the relationship between lightning and terrestrial gamma ray flashes. *Geophysical Research Letters*, 32(8):1–5, 2005. ISSN 0094-8276. doi: 10.1029/2005GL022778.

Dwyer, J. R. A fundamental limit on electric fields in air. *Geophysical Research Letters*, 30(20): 1–4, 2003. ISSN 0094-8276. doi: 10.1029/2003GL017781.

Dwyer, J. R. Implications of x-ray emission from lightning. *Geophysical Research Letters*, 31(12): L12102, 2004. ISSN 0094-8276. doi: 10.1029/2004GL019795.

Dwyer, J. R. Relativistic breakdown in planetary atmospheres. *Physics of Plasmas*, 14(4):42901, 2007. ISSN 1070664X. doi: 10.1063/1.2709652.

Dwyer, J. R. Source mechanisms of terrestrial gamma-ray flashes. *Journal of Geophysical Research*, 113(D10):D10103, May 2008. ISSN 0148-0227. doi: 10.1029/2007JD009248.

Dwyer, J. R. and Smith, D. M. A comparison between Monte Carlo simulations of runaway breakdown and terrestrial gamma-ray flash observations. *Geophysical Research Letters*, 32 (22):L22804, 2005. ISSN 0094-8276. doi: 10.1029/2005GL023848.

Dwyer, J. R., Rassoul, H. K., Al-Dayeh, M., Caraway, L., Chrest, A., Wright, B., Kozak, E., Jerauld, J., Uman, M. A., Rakov, V. A., Jordan, D. M., and Rambo, K. J. X-ray bursts associated with leader steps in cloud-to-ground lightning. *Geophysical Research Letters*, 32(1):1–4, 2005a. ISSN 0094-8276. doi: 10.1029/2004GL021782.

Dwyer, J. R., Rassoul, H. K., Saleh, Z., Uman, M. A., Jerauld, J., and Plumer, J. A. X-ray bursts produced by laboratory sparks in air. *Geophysical Research Letters*, 32(20):L20809, 2005b. ISSN 0094-8276. doi: 10.1029/2005GL024027.

Dwyer, J. R., Saleh, Z., Rassoul, H. K., Concha, D., Rahman, M., Cooray, V., Jerauld, J., Uman, M. a., and Rakov, V. a. A study of X-ray emission from laboratory sparks in air at atmospheric pressure. *Journal of Geophysical Research*, 113(D23):D23207, December 2008. ISSN 0148-0227. doi: 10.1029/2008JD010315.

Dwyer, J. R. The relativistic feedback discharge model of terrestrial gamma ray flashes. *Journal of Geophysical Research*, 117(A2):A02308, February 2012. ISSN 0148-0227. doi: 10.1029/2011JA017160.

Dwyer, J. R., Uman, M. a., Rassoul, H. K., Al-Dayeh, M., Caraway, L., Jerauld, J., Rakov, V. a., Jordan, D. M., Rambo, K. J., Corbin, V., and Wright, B. Energetic radiation produced during rocket-triggered lightning. *Science (New York, N.Y.)*, 299(5607):694–7, January 2003. ISSN 1095-9203. doi: 10.1126/science.1078940.

Dwyer, J. R., Smith, D. M., and Cummer, S. A. High-Energy Atmospheric Physics: Terrestrial Gamma-Ray Flashes and Related Phenomena. *Space Science Reviews*, 173(1-4):133–196, 2012. doi: 10.1007/s11214-012-9894-0.

Fishman, G. J., Bhat, P. N., Mallozzi, R., Horack, J. M., Koshut, T., Kouveliotou, C., Pendleton, G. N., Meegan, C. A., Wilson, R. B., Paciesas, W. S., Goodman, S. J., and Christian, H. J. Discovery of intense gamma-ray flashes of atmospheric origin. *Science (New York, N.Y.)*, 264(5163): 1313–1316, 1994. doi: 10.1126/science.264.5163.1313.

Fishman, G. J., Briggs, M. S., Connaughton, V., Bhat, P. N., Paciesas, W. S., von Kienlin, A., Wilson-Hodge, C., Kippen, R. M., Preece, R., Meegan, C. a., and Greiner, J. Temporal properties of the terrestrial gamma-ray flashes from the Gamma-Ray Burst Monitor on the Fermi Observatory. *Journal of Geophysical Research*, 116(A7):1–17, July 2011. ISSN 0148-0227. doi: 10.1029/2010JA016084.

Gallimberti, I., Bacchiega, G., Bondiou-clergerie, A., and Lalande, P. Fundamental processes in long air gap discharges. *Physique appliquée/Applied physics*, 3:1335–1359, 2002.

Gjesteland, T., Østgaard, N., Connell, P. H., Stadsnes, J., and Fishman, G. J. Effects of dead time losses on terrestrial gamma ray flash measurements with the Burst and Transient Source Experiment. *Journal of Geophysical Research*, 115:1–26, May 2010. ISSN 0148-0227. doi: 10.1029/2009JA014578.

Gjesteland, T., Østgaard, N., Collier, a. B., Carlson, B. E., Cohen, M. B., and Lehtinen, N. G. Confining the angular distribution of terrestrial gamma ray flash emission. *Journal of Geophysical Research*, 116(A11):A11313, November 2011. ISSN 0148-0227. doi: 10.1029/2011JA016716.

Gjesteland, T., Østgaard, N., Collier, a. B., Carlson, B. E., Eyles, C., and Smith, D. M. A new method reveals more TGFs in the RHESSI data. *Geophysical Research Letters*, 39(5), March 2012. ISSN 00948276. doi: 10.1029/2012GL050899.

Grefenstette, B. W., Smith, D. M., Dwyer, J. R., and Fishman, G. J. Time evolution of terrestrial gamma ray flashes. *Geophysical Research Letters*, 35(6):178, March 2008. ISSN 0094-8276. doi: 10.1029/2007GL032922.

Gurevich, A. V., Milikh, G. M., and Roussel-Dupre, R. Runaway electron mechanism of air breakdown and preconditioning during a thunderstorm. *Physics Letters A*, 165(5-6):463–468, June 1992. ISSN 03759601. doi: 10.1016/0375-9601(92)90348-P.

Gurevich, A. V. and Zybin, K. P. Runaway breakdown and electric discharges in thunderstorms. *Physics-Uspekhi*, 44(11):1119–1140, November 2001. ISSN 1063-7869. doi: 10.1070/PU2001v044n11ABEH000939.

Hansen, R. S., Østgaard, N., Gjesteland, T., and Carlson, B. How simulated fluence of photons from terrestrial gamma ray flashes at aircraft and balloon altitudes depends on initial parameters. *Journal of Geophysical Research: Space Physics*, 118(5):2333–2339, May 2013. ISSN 21699380. doi: 10.1002/jgra.50143.

Hazelton, B. J., Grefenstette, B. W., Smith, D. M., Dwyer, J. R., Shao, X.-M., Cummer, S. A., Chronis, T., Lay, E. H., and Holzworth, R. H. Spectral dependence of terrestrial gamma-ray flashes on source distance. *Geophysical Research Letters*, 36(1):1–5, January 2009. ISSN 0094-8276. doi: 10.1029/2008GL035906.

Hubbel, J. H. *Bibliography of Photon Total Cross Section (Attenuation Coefficient) Measurements 10 eV to 13.5 GeV, 1907-1993*. National Institute of Standards and Technology, Gathersburg, MD, 1994.

Inan, U., Reising, S., Fishman, G. J., and Horack, J. M. On the association of terrestrial gamma-ray bursts with lightning and implications for sprites. *Geophysical Research Letters*, 23(9): 1017–1020, 1996. doi: 10.1029/96GL00746.

International Commission on Radiation Units and Measurements. Stopping powers for electrons and positrons, ICRU Report 37. Technical report.

Klebesadel, R. Observations of gamma-ray bursts of cosmic origin. *The astrophysical journal*, 182, 1973.

Kochkin, P. O., Nguyen, C. V., van Deursen, a. P. J., and Ebert, U. Experimental study of hard x-rays emitted from metre-scale positive discharges in air. *Journal of Physics D: Applied Physics*, 45(42):425202, October 2012. ISSN 0022-3727. doi: 10.1088/0022-3727/45/42/425202.

Kochkin, P. O., van Deursen, a. P. J., and Ebert, U. Experimental study of the spatio-temporal development of metre-scale negative discharge in air. *Journal of Physics D: Applied Physics*, 47(14):145203, April 2014. ISSN 0022-3727. doi: 10.1088/0022-3727/47/14/145203.

Lin, R. P., Dennis, B. R., Hurford, G. J., Smith, D. M., Zehnder, A., Harvey, P. R., Curtis, D., Pankow, D., Turin, P., Bester, M., Csillaghy, A., Lewis, M., Madden, N., Beek, H. F. V., Appleby, M., Raudorf, T., McTiernan, J., Ramaty, R., Schmahl, E., Schwartz, R., Krucker, S., Abiad, R., Quinn, T., Berg, P., Hashii, M., Sterling, R., Jackson, R., Pratt, R., Campbell, R. D., Malone, D., Landis, D., Barringtong-Leigh, C. P., Slassi-Sennou, S., Cork, C., Clark, D., Amato, D., Orwig, L., Boyle, R., Banks, I. S., Shirey, K., Tolbert, A. K., Zarro, D., Snow, F., Thomsen, K., Henneck, R., Mchedlishvili, A., Ming, P., Fivian, M., Jordan, J., Wanner, R., Crubb, J., Preble, J., Matranga, M., Benz, A., Hudson, H., Canfield, R. C., Holman, G. D., Crannell, C., Kosugi, T., Emslie, A. G., Vilmer, N., Brown, J. C., Johns-Krull, C., Aschwanden, M., Metcalf, T., and Conway, A. The Reuven Ramaty high-energy solar spectroscopic imager (RHESSI). *Solar Physics2*, 210 (November):3–32, 2002. doi: 10.1117/12.506649.

Lu, G., Blakeslee, R. J., Li, J., Smith, D. M., Shao, X.-M., McCaul, E. W., Buechler, D. E., Christian, H. J., Hall, J. M., and Cummer, S. A. Lightning mapping observation of a terrestrial gamma-ray flash. *Geophysical Research Letters*, 37(11):1–5, June 2010. ISSN 0094-8276. doi: 10.1029/2010GL043494.

March, V. and Montanyà, J. Influence of the voltage-time derivative in X-ray emission from laboratory sparks. *Geophysical Research Letters*, 37(19):n/a–n/a, October 2010. ISSN 00948276. doi: 10.1029/2010GL044543.

March, V. and Montanyà, J. X-rays from laboratory sparks in air: The role of the cathode in the production of runaway electrons. *Geophysical Research Letters*, 38(4):n/a–n/a, February 2011. ISSN 00948276. doi: 10.1029/2010GL046540.

Marisaldi, M., Fuschino, F., Labanti, C., Galli, M., Longo, F., Del Monte, E., Barbiellini, G., Tavani, M., Giuliani, A., Moretti, E., Vercellone, S., Costa, E., Cutini, S., Donnarumma, I., Evangelista, Y., Feroci, M., Lapshov, I., Lazzarotto, F., Lipari, P., Mereghetti, S., Pacciani, L., Rapisarda, M., Soffitta, P., Trifoglio, M., Argan, A., Boffelli, F., Bulgarelli, A., Caraveo, P., Cattaneo, P. W., Chen, A., Cocco, V., D'Ammando, F., De Paris, G., Di Cocco, G., Di Persio, G., Ferrari, A., Fiorini, M., Froysland, T., Gianotti, F., Morselli, A., Pellizzoni, A., Perotti, F., Picozza, P., Piano, G., Pilia, M., Prest, M., Pucella, G., Rappoldi, A., Rubini, A., Sabatini, S., Striani, E., Trois, A., Vallazza, E.,

Vittorini, V., Zambra, A., Zanello, D., Antonelli, L. a., Colafrancesco, S., Gasparrini, D., Giommi, P., Pittori, C., Preger, B., Santolamazza, P., Verrecchia, F., and Salotti, L. Detection of terrestrial gamma ray flashes up to 40 MeV by the AGILE satellite. *Journal of Geophysical Research*, 115: 1–12, March 2010. ISSN 0148-0227. doi: 10.1029/2009JA014502.

Meegan, C., Lichti, G., Bhat, P. N., Bissaldi, E., Briggs, M. S., Connaughton, V., Diehl, R., Fishman, G., Greiner, J., Hoover, A. S., van der Horst, A. J., von Kienlin, A., Kippen, R. M., Kouveliotou, C., McBreen, S., Paciesas, W. S., Preece, R., Steinle, H., Wallace, M. S., Wilson, R. B., and Wilson-Hodge, C. The Fermi Gamma-Ray Burst Monitor. *The Astrophysical Journal*, 702(1):791–804, September 2009. ISSN 0004-637X. doi: 10.1088/0004-637X/702/1/791.

Moore, C. and Eack, K. Energetic radiation associated with lightning stepped-leaders. *Geophysical Research ...*, 28(11):2141–2144, 2001.

Moss, G. D., Pasko, V. P., Liu, N., and Veronis, G. Monte Carlo model for analysis of thermal runaway electrons in streamer tips in transient luminous events and streamer zones of lightning leaders. *Journal of Geophysical Research*, 111(A2):1–37, 2006. ISSN 0148-0227. doi: 10.1029/2005JA011350.

Nguyen, C. V. *Experimental study on hard radiation from long laboratory spark discharges in air*. Ph.d., Technical University of Eindhoven, 2012.

Nguyen, C. V., van Deursen, A. P. J., and Ebert, U. Multiple x-ray bursts from long discharges in air. *Journal of Physics D: Applied Physics*, 41(23):234012, December 2008. ISSN 0022-3727. doi: 10.1088/0022-3727/41/23/234012.

Nguyen, C. V., van Deursen, A. P. J., van Heesch, E. J. M., Winands, G. J. J., and Pemen, A. J. M. X-ray emission in streamer-corona plasma. *Journal of Physics D: Applied Physics*, 43(2):025202, January 2010. ISSN 0022-3727. doi: 10.1088/0022-3727/43/2/025202.

Nijdam, S., Moerman, J. S., Briels, T. M. P., van Veldhuizen, E. M., and Ebert, U. Stereophotography of streamers in air. *Applied Physics Letters*, 92(10):101502, 2008. ISSN 00036951. doi: 10.1063/1.2894195.

Østgaard, N., Gjesteland, T., Stadsnes, J., Connell, P. H., and Carlson, B. Production altitude and time delays of the terrestrial gamma flashes: Revisiting the Burst and Transient Source Experiment spectra. *Journal of Geophysical Research*, 113(A2):A02307, February 2008. ISSN 0148-0227. doi: 10.1029/2007JA012618.

Østgaard, N., Gjesteland, T., Hansen, R. S., Collier, A. B., and Carlson, B. The true fluence distribution of terrestrial gamma flashes at satellite altitude. *Journal of Geophysical Research*, 117 (A3):A03327, March 2012. ISSN 0148-0227. doi: 10.1029/2011JA017365.

Østgaard, N., Gjesteland, T., Carlson, B. E., Collier, A. B., Cummer, S. A., Lu, G., and Christian, H. J. Simultaneous observations of optical lightning and terrestrial gamma ray flash from space. *Geophysical Research Letters*, 40(10):2423–2426, May 2013. ISSN 00948276. doi: 10.1002/grl.50466.

Rahman, M., Cooray, V., Ahmad, N. A., Nyberg, J., Rakov, V. a., and Sharma, S. X rays from 80-cm long sparks in air. *Geophysical Research Letters*, 35(6):1–4, March 2008. ISSN 0094-8276. doi: 10.1029/2007GL032678.

Rakov, V. A. and Uman, M. A. *Lightning: physics and effects*. Cambridge University Press, Cambridge, 2003. ISBN 978-0521035415.

Shao, X.-M., Hamlin, T., and Smith, D. M. A closer examination of terrestrial gamma-ray flash-related lightning processes. *Journal of Geophysical Research*, 115(April 2004):1–8, June 2010. ISSN 0148-0227. doi: 10.1029/2009JA014835.

Skeltved, A. B. *A study of the relativistic runaway electron avalanche and the feedback theories to explain terrestrial gammaray production*. M.sc. thesis, University of Bergen, 2013.

Skeltved, A., Østgaard, N., Carlson, B., Gjesteland, T., and Celestin, S. Modeling the relativistic runaway electron avalanche and the feedback mechanism with GEANT4. *Journal of . . .*, 2014. doi: 10.1002/2014JA020504.Received.

Smith, D. M., Dwyer, J. R., Hazelton, B. J., Grefenstette, B. W., Martinez-McKinney, G. F. M., Zhang, Z. Y., Lowell, a. W., Kelley, N. a., Splitt, M. E., Lazarus, S. M., Ulrich, W., Schaal, M., Saleh, Z. H., Cramer, E., Rassoul, H. K., Cummer, S. a., Lu, G., and Blakeslee, R. J. The rarity

of terrestrial gamma-ray flashes. *Geophysical Research Letters*, 38(8):3–7, April 2011a. ISSN 0094-8276. doi: 10.1029/2011GL046875.

Smith, D. M., Lopez, L. I., Lin, R. P., and Barrington-Leigh, C. P. Terrestrial gamma-ray flashes observed up to 20 MeV. *Science (New York, N.Y.)*, 307(5712):1085–8, February 2005. ISSN 1095-9203. doi: 10.1126/science.1107466.

Smith, D. M., Lazarus, S. M., Ulrich, W., Schaal, M., Saleh, Z., Cramer, E., Rassoul, H. K., Cummer, S. a., Lu, G., Shao, X.-M., Ho, C., Dwyer, J. R., Hamlin, T., Blakeslee, R. J., Heckman, S. J., Hazelton, B. J., Grefenstette, B. W., Martinez-McKinney, G. F. M., Zhang, Z. Y., Lowell, A. W., Kelley, N. a., and Splitt, M. E. A terrestrial gamma-ray flash observed from an aircraft. *Journal of Geophysical Research*, 116:1–10, 2011b. ISSN 0148-0227. doi: 10.1029/2011JD016252.

Splitt, M. E., Lazarus, S. M., Barnes, D., Dwyer, J. R., Rassoul, H. K., Smith, D. M., Hazelton, B., and Grefenstette, B. Thunderstorm characteristics associated with RHESSI identified terrestrial gamma ray flashes. *Journal of Geophysical Research*, 115:1–10, June 2010. ISSN 0148-0227. doi: 10.1029/2009JA014622.

Stanley, M. a., Shao, X.-M., Smith, D. M., Lopez, L. I., Pongratz, M. B., Harlin, J. D., Stock, M., and Regan, A. A link between terrestrial gamma-ray flashes and intracloud lightning discharges. *Geophysical Research Letters*, 33(6):1–5, 2006. ISSN 0094-8276. doi: 10.1029/2005GL025537.

Tavani, M., Barbiellini, G., Argan, A., Bulgarelli, A., Caraveo, P., Chen, A., Cocco, V., Costa, E., De Paris, G., Del Monte, E., Di Cocco, G., Donnarumma, I., Feroci, M., Fiorini, M., Froysland, T., Fuschino, F., Galli, M., Gianotti, F., Giuliani, A., Evangelista, Y., Labanti, C., Lapshov, I., Lazzarotto, F., Lipari, P., Longo, F., Marisaldi, M., Mastropietro, M., Mauri, F., Mereghetti, S., Morelli, E., Morselli, A., Pacciani, L., Pellizzoni, A., Perotti, F., Picozza, P., Pontoni, C., Porrovecchio, G., Prest, M., Pucella, G., Rapisarda, M., Rossi, E., Rubini, A., Soffitta, P., Trifoglio, M., Trois, A., Vallazza, E., Vercellone, S., Zambra, A., Zanello, D., Giommi, P., Antonelli, A., and Pittori, C. The AGILE space mission. *Nuclear Instruments and Methods in Physics Research Section A: Accelerators, Spectrometers, Detectors and Associated Equipment*, 588(1-2):52–62, April 2008. ISSN 01689002. doi: 10.1016/j.nima.2008.01.023.

Tavani, M., Barbiellini, G., Argan, A., Boffelli, F., Bulgarelli, A., Caraveo, P., Cattaneo, P. W., Chen, A. W., Cocco, V., Costa, E., D'Ammando, F., Del Monte, E., De Paris, G., Di Cocco, G., Di Persio, G., Donnarumma, I., Evangelista, Y., Feroci, M., Ferrari, A., Fiorini, M., Fornari, F., Fuschino, F., Froysland, T., Frutti, M., Galli, M., Gianotti, F., Giuliani, A., Labanti, C., Lapshov, I., Lazzarotto, F., Liello, F., Lipari, P., Longo, F., Mattaini, E., Marisaldi, M., Mastropietro, M., Mauri, A., Mauri, F., Mereghetti, S., Morelli, E., Morselli, A., Pacciani, L., Pellizzoni, A., Perotti, F., Piano, G., Picozza, P., Pontoni, C., Porrovecchio, G., Prest, M., Pucella, G., Rapisarda, M., Rappoldi, A., Rossi, E., Rubini, A., Soffitta, P., Traci, A., Trifoglio, M., Trois, A., Vallazza, E., Vercellone, S., Vittorini, V., Zambra, A., Zanello, D., Pittori, C., Preger, B., Santolamazza, P., Verrecchia, F., Giommi, P., Colafrancesco, S., Antonelli, A., Cutini, S., Gasparrini, D., Stellato, S., Fanari, G., Primavera, R., Tamburelli, F., Viola, F., Guarrera, G., Salotti, L., D'Amico, F., Marchetti, E., Crisconio, M., Sabatini, P., Annoni, G., Alia, S., Longoni, A., Sanquerin, R., Battilana, M., Concari, P., Dessimone, E., Grossi, R., Parise, A., Monzani, F., Artina, E., Pavesi, R., Marseguerra, G., Nicolini, L., Scandelli, L., Soli, L., Vettorello, V., Zardetto, E., Bonati, A., Maltecca, L., D'Alba, E., Patané, M., Babini, G., Onorati, F., Acquaroli, L., Angelucci, M., Morelli, B., Agostara, C., Cerone, M., Michetti, A., Tempesta, P., D'Eramo, S., Rocca, F., Giannini, F., Borghi, G., Garavelli, B., Conte, M., Balasini, M., Ferrario, I., Vanotti, M., Collavo, E., and Giacomazzo, M. The AGILE Mission. *Astronomy and Astrophysics*, 502(3):995–1013, August 2009. ISSN 0004-6361. doi: 10.1051/0004-6361/200810527.

Tavani, M., Marisaldi, M., Labanti, C., Fuschino, F., Argan, A., Trois, A., Giommi, P., Colafrancesco, S., Pittori, C., Palma, F., Trifoglio, M., Gianotti, F., Bulgarelli, A., Vittorini, V., Verrecchia, F., Salotti, L., Barbiellini, G., Caraveo, P., Cattaneo, P., Chen, A., Contessi, T., Costa, E., D'Ammando, F., Del Monte, E., De Paris, G., Di Cocco, G., Di Persio, G., Donnarumma, I., Evangelista, Y., Feroci, M., Ferrari, A., Galli, M., Giuliani, A., Giusti, M., Lapshov, I., Lazzarotto, F., Lipari, P., Longo, F., Mereghetti, S., Morelli, E., Moretti, E., Morselli, A., Pacciani, L., Pellizzoni, A., Perotti, F., Piano, G., Picozza, P., Pilia, M., Pucella, G., Prest, M., Rapisarda, M., Rappoldi, A., Rossi, E., Rubini, A., Sabatini, S., Scalise, E., Soffitta, P., Striani, E., Vallazza, E., Vercellone, S., Zambra, A., and Zanello, D. Terrestrial Gamma-Ray Flashes as Powerful Particle Accelerators. *Physical Review Letters*, 106(1):1–5, January 2011. ISSN 0031-9007. doi: 10.1103/PhysRevLett.106.018501.

Tipler, P. A. and Llewellyn, R. A. *Modern Physics*. W. H. Freeman and Company, New York, 5th edition, 2008.

Williams, E., Boldi, R., Bór, J., Sátori, G., Price, C., Greenberg, E., Takahashi, Y., Yamamoto, K., Matsudo, Y., Hobara, Y., Hayakawa, M., Chronis, T., Anagnostou, E., Smith, D. M., and Lopez, L. Lightning flashes conducive to the production and escape of gamma radiation to space. *Journal of Geophysical Research*, 111(D16):1–7, 2006. ISSN 0148-0227. doi: 10.1029/2005JD006447.

Wilson, C. T. R. The Acceleration of β-particles in Strong Electric Fields such as those of Thunderclouds. *Proc. Cambridge Philos. Soc.*, 22:534–538, 1925.